Analysis Note

Measurement of charged particle production in diffractive proton-proton collisions at $\sqrt{s} = 200$ GeV with tagging of the forward scattered proton

Leszek Adamczyk[1], Łukasz Fulek[1], Mariusz Przybycień[1], and Rafał Sikora[1]

[1] *AGH University of Science and Technology, FPACS, Kraków, Poland*

26th November 2020

In this note we present the analysis of the Single Diffractive Dissociation process with the STAR Roman Pot (RP) detectors at RHIC. The measurement is focused on the charged particle multiplicity, its dependence on the transverse momentum and pseudorapidity in three regions of ξ: $0.02 < \xi < 0.05$, $0.05 < \xi < 0.1$ and $0.1 < \xi < 02$. The identified particle to antiparticle (pion, kaon, proton and their antiparticle) multiplicity ratios as a function of transverse momentum in above three ξ regions are also measured. The data come from proton-proton collisions collected in 2015. The forward proton was tagged in the STAR Roman Pot system while the charged particle tracks were reconstructed in the STAR Time Projection Chamber (TPC). We describe all stages of the analysis involving comparison of the data with MC simulations and systematic uncertainty studies. More technical parts of the analysis are described in a supplementary analysis note [1].

List of contributions

Leszek Adamczyk	Analysis coordination/supervision, production of picoDST, production of embedded MC samples
Łukasz Fulek*	Main analyzer, write-up author
Mariusz Przybycień	Analysis supervision
Rafał Sikora	Analysis support

* - contact editor

Change log

26th November 2020	ver. 1.0	Initial revision

Contents

Acronyms

CD	Central Diffraction
DD	Double Diffraction
MBR	Minimum Bias Rockefeller
MC	Monte Carlo
ND	Non-Diffractive
QCD	Quantum Chromodynamics
RP	Roman Pot
SaS	Schuler and Sjöstrand
SD	Single Diffraction
TPC	Time Projection Chamber

1. Introduction

Inclusive measurements of charged-particle distributions in proton–proton (pp) collisions probe the strong interaction in the low-momentum transfer, non-perturbative regime of Quantum Chromodynamics (QCD). In this kinematic region interactions are usually described by phenomenological models implemented in Monte Carlo (MC) event generators. Measurements can be used to constrain the free parameters of these models. An accurate description of low-energy strong interaction processes is essential for understanding and precise simulation of different types of pp processes and the effects of multiple pp collisions in the same bunch crossing at high instantaneous luminosity at hadron colliders. Measurements with tagging of the forward-scattered proton are of special interest. They give direct access to specific but still significant part of pp processes called diffraction. In addition precise modelling of forward particle production is essential for better understanding of the longitudinal development of air showers observed in experiments studying cosmic radiation.

We present a measurement of charged particle production in events with single forward proton tagging (dominated by Single Diffraction (SD): $p + p \to p + \mathrm{X}$). The following observables are studied:

$$\frac{1}{N_{\mathrm{ev}}}\frac{dN_{\mathrm{ev}}}{dn_{\mathrm{ch}}}, \qquad \frac{1}{N_{\mathrm{ev}}}\frac{1}{2\pi p_{\mathrm{T}}}\frac{d^2N}{d\bar{\eta}dp_{\mathrm{T}}}, \qquad \frac{1}{N_{\mathrm{ev}}}\frac{dN}{d\bar{\eta}} \tag{1.1}$$

where n_{ch} is the number of primary charged particles within kinematic range given by $p_{\mathrm{T}} >$ 200 MeV and $|\eta| < 0.7$, N_{ev} is the total number of events with $2 \leq n_{\mathrm{ch}} \leq 8$, N is the total number of charged particles within the above kinematic acceptance and $\bar{\eta}$ is the pseudorapidity of the charged particle with longitudinal momentum taken with respect to direction of the forward scattered proton. To suppress non-SD events the trigger system required no signal in BBC-small in the direction of forward scattered proton and signal in BBC-small in opposite direction. The measurements are performed in a fiducial phase space of the forward scattered protons of $0.04 < -t < 0.16\ \mathrm{GeV}^2/\mathrm{c}^2$ and $0.02 < \xi < 0.2$, where ξ is the fractional energy loss of the scattered proton and t is the squared four momentum transfer. In case of SD process $\xi = M_{\mathrm{X}}^2/s$, where M_{X} is the mass of the state X into which one of the incoming proton dissociates and s is the center of mass energy squared of the pp system. The Mandelstam variable t is defined by $t = (p_1 - p_3)^2$, where p_1 is the four-momentum of the incoming proton, p_3 is the four-momentum of the outgoing proton. The above mentioned observables are presented in three ξ regions: $0.02 < \xi < 0.05$, $0.05 < \xi < 0.1$ and $0.1 < \xi < 0.2$. In addition their average values are presented as a function of ξ.

We have also studied an identified particle to antiparticle (pion, kaon, proton and their antiparticle) multiplicity ratios as a function of p_{T} also in the above mentioned three regions of ξ. The system X into which proton diffractively dissociates has net charge and baryon number +1. It is believed that initial charge and barion number should appear in the very forward direction leading to the equal amount of particles and antiparticles in the central region created by fragmentation and hadronization processes. However other scenarios are also possible where extra baryon is uniformly distributed over rapidity [2] or even appear close to the gap edge [3]. It is natural to expect that possible charge and baryon number transfer to central region will be better visible at small ξ where amount of particle-antiparticle creation is smaller due to the generally smaller particle multiplicity or due to the fact that gap edge is inside our fiducial region of $|\eta| < 0.7$.

2. Monte Carlo Samples

MC samples used to correct data for detector effects were obtained by the embedding MC technique [4], in which simulated particles are mixed with the real Zerobias events at the raw data level. Zerobias data events used in the embedding were sampled over the entire data-taking period in order to properly describe the data set used in the analysis. Two samples of embedding MC were produced:

1. Single particle MC, in which particles are generated from flat distributions in η and p_{T}, in order to have similar statistics in all bins.

2. The Schuler and Sjöstrand (SaS) model implemented in PYTHIA 8 with 4C tune.

Generated particles were passed through the full simulation of the STAR TPC and RP system detectors using GEANT3 and GEANT4, respectively, and then embedded into real data sample. These embedding events were next processed through the full event reconstruction chain.

It is preferred to get the detector corrections from a MC, which is dedicated to simulate the studied physics process. However, for this purpose, the statistics in the MC should be several times greater than in the analysed data sample. Since this is not possible with low efficiency of TPC and TOF, the basic method of corrections used in the analysis for p_{T} and $\bar{\eta}$ distributions is a method of factorization of global efficiency into the product of single-particle efficiencies. In this way, statistically precise multidimensional corrections on TPC and TOF were obtained from the single particle MC. The energy loss correction was also determined from the same MC sample. The charged-particle multiplicity distributions were unfolded from the measured multiplicities of TPC tracks based on the response matrix, which takes into account all detector effects. In this procedure single particle MC samples were not used.

All other detector corrections were obtained from PYTHIA 8 4C (SaS). In order to keep statistical precision coming from the corrections high, samples filtered on true-level values of ξ and t (not necessarily with reconstructed proton track in RP) are used.

Several additional MC samples were generated, in which simulated particles were propagated through full simulation and reconstruction chain but were not embedded into Zerobias events. Systematic uncertainty related to hadronization of the diffractive system was determined by using alternative hadronization models as implemented in HERWIG and EPOS. Results are compared to model predictions from PYTHIA 8 4C (SaS), HERWIG, EPOS and alternative PYTHIA 8 model Minimum Bias Rockefeller (MBR) with A2 tune. EPOS predicts very large contribution of forward protons, which originate from Non-Diffractive (ND) events and are well separated in rapidity from other final state particles. This is the result of low mass excitation of the proton remnant (< 1 GeV) leading to hadronization of the beam remnant back to the proton. Therefore EPOS predictions were separated in two classes: diffractive (EPOS SD) modelled by Pomeron exchange and ND modelled by low mass excitation of the proton remnant (EPOS SD$'$). Such remnant treatment is very unique in EPOS compared to other string models, especially, to that used in PYTHIA 8, where ND forward protons are rare and arise from string fragmentation and hadronization. In all PYTHIA 8 models, diffractive cross-sections are scaled by the factors, which were introduced in order to describe the full phase space [5, 6]. In the SaS model, the scaling factors for SD and DD, F_{SD} and F_{DD}, are defined as a function of diffractive masses:

$$F_{\mathrm{SD}} = \left(1 - \frac{M^2}{s}\right)\left(1 + \frac{c_{\mathrm{res}} M_{\mathrm{res}}^2}{M_{\mathrm{res}}^2 + M^2}\right) \tag{2.1}$$

$$F_{\mathrm{DD}} = \left(1 - \frac{M_a^2 + M_b^2}{s}\right)\left(\frac{s m_p^2}{s m_p^2 + M_a^2 M_b^2}\right) \times \left(1 + \frac{c_{\mathrm{res}} M_{\mathrm{res}}^2}{M_{\mathrm{res}}^2 + M_a^2}\right)\left(1 + \frac{c_{\mathrm{res}} M_{\mathrm{res}}^2}{M_{\mathrm{res}}^2 + M_b^2}\right) \tag{2.2}$$

where M and M_a, M_b are the invariant masses of the systems X and X_a, X_b for SD and DD, respectively, $c_{\mathrm{res}} = 2$ and $M_{\mathrm{res}} = 2$ GeV/c^2 were obtained from a fit to $pp/\bar{p}p$ data [5]. On the other hand, in the MBR model the scaling factor is given as a function of the rapidity gap [6]:

$$S = \frac{1}{2}\left[1 + \mathrm{erf}\left(\frac{\Delta y - \Delta y_S}{\sigma_S}\right)\right] \tag{2.3}$$

where Δy is the rapidity gap, $\Delta y_S = 2$ and $\sigma_S = 0.5$. As a result, diffractive cross sections are artificially suppressed at relatively large values of ξ (>0.05). This artificial suppression significantly changes predicted distribution of ξ and fractions of different processes in our fiducial phase space. Therefore data is also compared with expectations obtained without suppression of the diffractive cross sections (MBR-tuned).

Figure 2.1 (left) shows the distribution of ξ generated with EPOS (SD and SD+SD$'$) and PYTHIA 8 SD (SaS, MBR and MBR-tuned). PYTHIA 8 (MBR) predicts a strong dependence of the cross section on ξ, which is much weaker in PYTHIA 8 (SaS and MBR-tuned) and the weakest in EPOS. This difference between PYTHIA 8 SaS and MBR models is expected since they are based on different Pomeron trajectories ($\epsilon_{\mathrm{SaS}} = 0$, $\epsilon_{\mathrm{MBR}} = 0.104$). Only 30% of events in EPOS are SD, while the rest are SD$'$. Since all MC samples were generated with forward proton filter (a cut on the proton position in front of the RPs), the shapes of $|t|$ distributions for these samples are biased. In order to compare them with each other, only their ratio to PYTHIA 8 (MBR) predictions is presented as a function of $|t|$. EPOS SD is only relevant for very small $|t|$ (below 0.04 GeV^2/c^2) and is suppressed in the STAR acceptance region, $0.04 < |t| < 0.16$, where EPOS SD$'$ contribution dominates. The t-slope is very different for EPOS SD and EPOS SD$'$, while it is similar for EPOS SD+SD$'$ and PYTHIA 8 (SaS and MBR-tuned), EPOS SD and PYTHIA 8 (MBR). This is related to the smaller average value of ξ for EPOS SD and PYTHIA 8 (MBR) compared to EPOS SD+SD' and PYTHIA 8 (SaS and MBR-tuned).

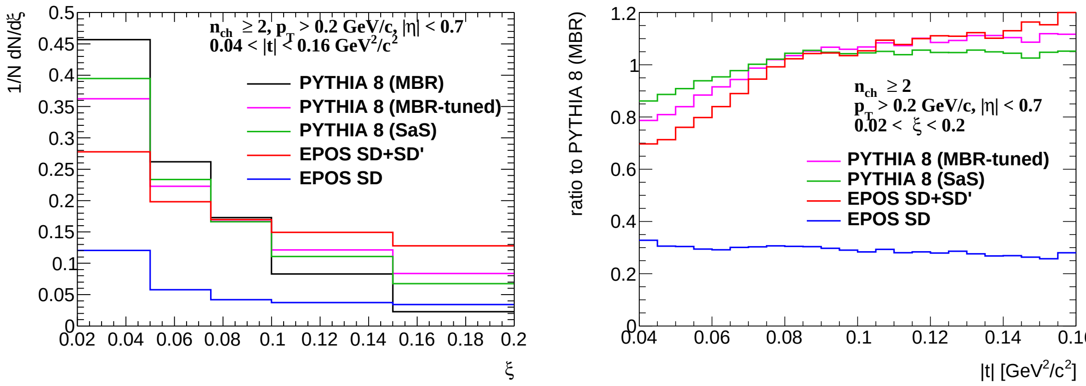

Figure 2.1: (left) ξ distribution for various MC generators and (right) ratios of different MCs to PYTHIA 8 (MBR) predictions as a function of $|t|$ at $\sqrt{s} = 200$ GeV.

3. Data Sample and Event Selection

The data sample used in this analysis was collected in proton-proton collisions at centre-of-mass energy of $\sqrt{s} = 200$ GeV during RHIC Run 15.

All of the studies in this analysis use data from only the SDT trigger condition, which was the main trigger designed for SD studies in Run 15. The logic of the trigger was formed by the following conditions combined with the logical AND:

1. RP_EOR || RP_WOR - signal in at least one RP on any side of the STAR central detector,
2. veto on any signal in small BBC tiles or ZDC on the triggered RP side of the STAR central detector,
3. at least two TOF hits.

The above requirements were imposed in accordance with the diffractive event topology. Veto on any signal in small BBC tiles and ZDC allowed to accept only events with rapidity gap and reject diffractive events with simultaneous pile-up event. The requirement of at least two TOF hits was applied to ensure activity in the mid-rapidity.

Integrated luminosity delivered by the RHIC to the STAR experiment in *pp* collisions during Run 15 amounts to 185.1 pb^{-1} [9], whereas about 34.4M SDT events were gathered by the STAR detector, shown in Fig. 3.1, which corresponds to 16 nb^{-1} of integrated luminosity.

Event Selection

Events were selected from those passing the SDT trigger condition. In order to remove events of poor quality and to suppress background the following conditions were required:

1. trigger signals in exactly two stations of one arm of RP system (this requirement divides the sample into four sub-samples, which were later analysed independently, e.g. for background studies),
2. any trigger signal in small BBC tiles on the opposite side of the STAR central detector to the triggered RP station,

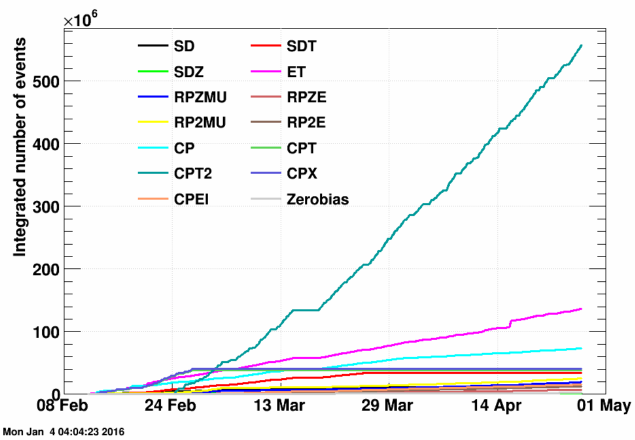

Figure 3.1: Cumulative number of events collected for each trigger in the RP data stream during Run 15 [7, 8].

3. exactly one proton track in the above RP stations with $0.02 < \xi < 0.2$ and $0.04 < -t < 0.16$ GeV^2/c^2.

4. exactly one vertex reconstructed from TPC tracks matched with hits in TOF (later in the text such vertex is referred as a TOF vertex),

5. TOF vertex within $|V_z| < 80$ cm - events with vertices away from the nominal IP have low acceptance for the central and forward tracks,

6. at least two but no more than eight primary TPC tracks, $2 \leq n_{\mathrm{sel}} \leq 8$, matched with hits in TOF and satisfying the selection criteria described in Sec. 3.1,

7. if there are exactly two primary tracks satisfying the above criteria and exactly two global tracks used in vertex reconstruction (Sec. 5.1), the longitudinal distance between these global tracks should be smaller than 2 cm, $|\Delta z_0| < 2$ cm.

Figure 3.2 shows the multiplicity of TOF vertices n_{vrt} (left) and the z-position of reconstructed vertices in single TOF vertex events (right). Data are compared to embedded PYTHIA 8 SD sample. These distributions are not significantly process-dependent, therefore, contributions from other processes are not included in these plots. Most events with $n_{\mathrm{vrt}} > 1$ originate from in-time pile-up and are excluded from the analysis.

ZDC Veto

The SDT trigger conditions imposed a veto on any signal in the same-side ZDC. However, all MC samples do not contain ZDC simulation. To check the impact of this veto on the measurement, the total energy of neutral particles, such as n, γ, π^0, produced within ZDC acceptance ($|\eta| > 6$) was measured using true-level PYTHIA 8 (SaS). In most of the events, the energy measured on the proton side of the IP is smaller than trigger thresholds (as shown in Fig. 3.3). Therefore, the ZDC veto has a negligible effect on the analysis and ZDC simulation is not needed.

3.1 Track Selection

The following quality cuts had to be passed by the selected primary tracks:

1. the tracks must be matched with hits reconstructed in TOF,

2. the number of the TPC hits used in the helix fit $N_{\mathrm{hits}}^{\mathrm{fit}}$ must be greater than 24,

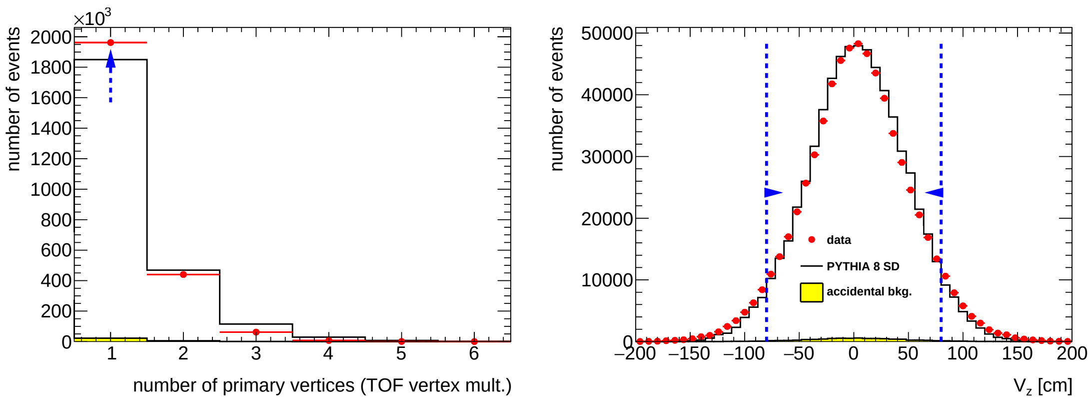

Figure 3.2: (left) Vertex multiplicity and (right) the z-position of reconstructed vertices in single TOF vertex events before applying the cut on the quantity shown. Blue lines indicate regions accepted in the analysis.

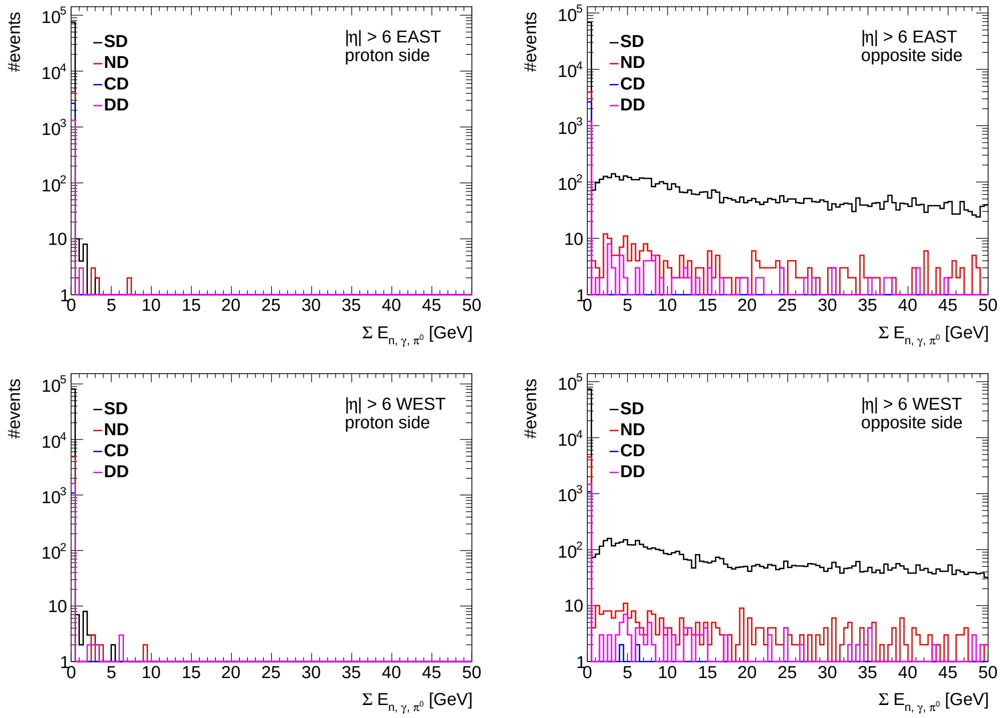

Figure 3.3: Total energy of neutral particles (n, γ, π^0) produced within ZDC acceptance ($|\eta| > 6$) for events in which forward-scattered proton is on (top) west and (bottom) east side of the IP. Distributions are presented separately for neutral particles produced on (left) the proton and (right) opposite side of the IP. PYTHIA 8 predictions for different processes are shown as colour histograms.

3. the number of the TPC hits used to determine the dE/dx information $N_{\mathrm{hits}}^{\mathrm{dE/dx}}$ must be greater than 14,

4. the transverse impact parameter with respect to the beamline d_0 must be less than 1.5 cm,

5. the radial component of the distance of the closest approach between the global helix and the vertex DCA_{xy} must be less than 1.5 cm,

6. the absolute magnitude of longitudinal component of the distance of the closest approach between the global helix and the vertex $|\mathrm{DCA}_z|$ must be less than 1 cm,

7. the track's transverse momentum p_{T} must be greater than 0.2 GeV/c,

8. the track's absolute value of pseudorapidity $|\eta|$ must be smaller than 0.7.

The $N_{\mathrm{hits}}^{\mathrm{fit}}$ and $N_{\mathrm{hits}}^{\mathrm{fit}}/N_{\mathrm{hits}}^{\mathrm{possible}}$ cuts are used to reject low quality TPC tracks and avoid track splitting effects. The d_0 and global DCA_{xy}, $|\mathrm{DCA}_z|$ cuts are used to select tracks that originate from the primary interaction vertex. The cut on $N_{\mathrm{hits}}^{\mathrm{dE/dx}}$ is used to ensure that selected tracks have sufficient energy loss information for particle identification purposes. In this analysis tracks without identification are required to have $p_{\mathrm{T}} > 0.2$ GeV/c and $|\eta| < 0.7$ due to high track reconstruction and TOF matching efficiencies in this region. For the identified particle-antiparticle ratio analysis, where charged pions, charged kaons and (anti)protons are measured, the p_{T} cut was increased for kaons and (anti)protons to 0.3 and 0.4 GeV/c, respectively. The distributions of the DCA_{xy}, $|\mathrm{DCA}_z|$, d_0, $N_{\mathrm{hits}}^{\mathrm{fit}}$ and $N_{\mathrm{hits}}^{\mathrm{dE/dx}}$ quantities together with applied cuts are shown in

Fig. 3.4, while the p_{T}, η and the azimuthal angle, ϕ, of the reconstructed tracks are shown in Fig. 3.5. Data are compared to embedded PYTHIA 8 SD sample.

The azimuthal angle of the reconstructed tracks for runs ≤ 16073050 is not described by PYTHIA 8. The inner sector #19 in the TPC was dead for this running period and some effects related to it were presumably not taken into account in the TPC detector simulation. Therefore, additional data-driven corrections to track efficiencies are used [1]. The larger accidental background is observed for runs > 16073050, probably due to the higher bunch intensities in this running period [10].

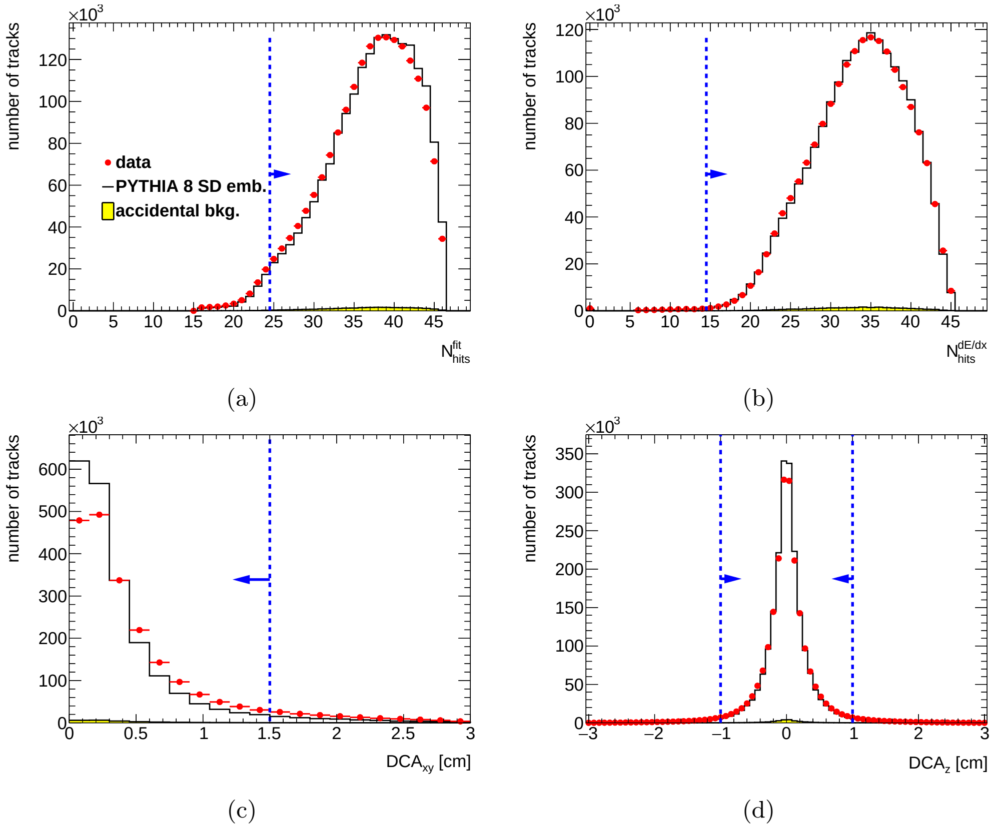

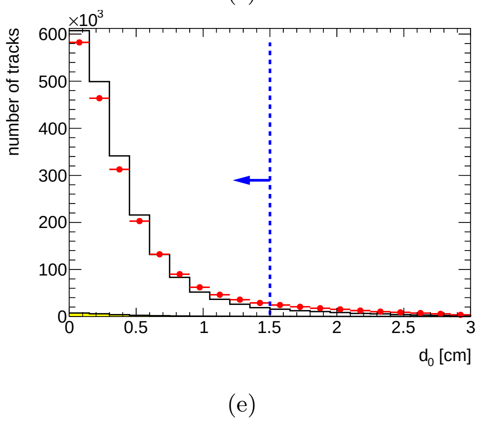

Figure 3.4: Number of the TPC hits used in the helix fit (a) and number of the TPC hits used to determine the dE/dx (b), the radial component (c) and the absolute magnitude of the longitudinal component (d) of the distance of the closest approach between the global helix and the vertex, transverse impact parameter w.r.t. beam-line (e). All distributions are shown before applying the corresponding cuts. Blue lines indicate regions accepted in the analysis.

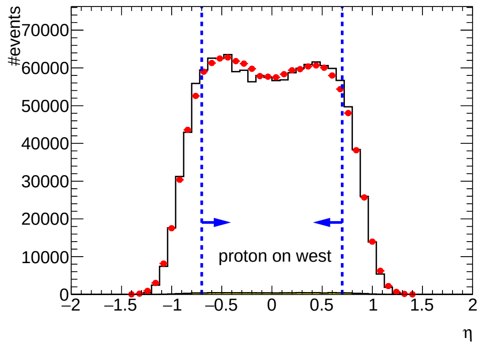

(a)

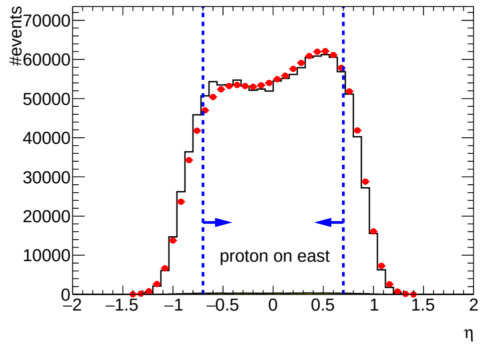

(b)

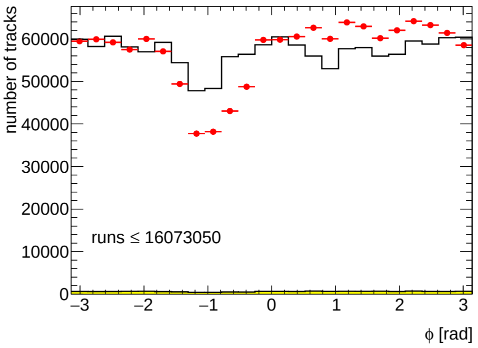

(c)

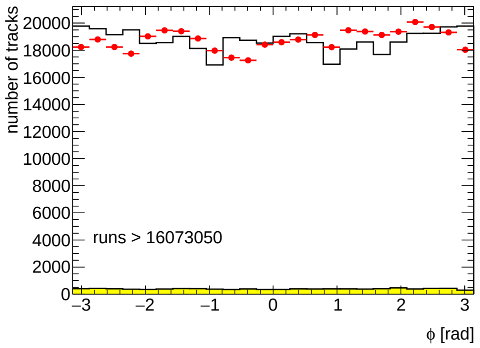

(d)

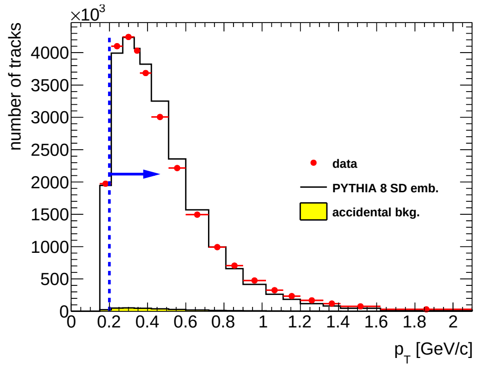

(e)

Figure 3.5: Pseudorapidity of the reconstructed tracks for events in which forward proton is on west (a) and east (b) side of the IP, track azimuthal angle for runs $\leq$ 16073050 (c) and $>$ 16073050 (d) and track transverse momentum (e). All distributions are shown before applying the corresponding cuts. Blue lines indicate regions accepted in the analysis.

3.2 Fiducial Region of the Measurement

A fiducial phase space of measurement is defined by the following criteria. Primary charged particles are defined as charged particles with a mean lifetime $\tau > 300$ ps, either directly produced in *pp* interaction or from subsequent decays of directly produced particles with $\tau < 30$ ps. Primary charged particles had to be contained within the kinematic range of $p_{\mathrm{T}} > 0.2$ GeV/c and $|\eta| < 0.7$. The results are corrected to the region of the total number of primary charged particles (without identification), $2 \leq n_{\mathrm{ch}} \leq 8$. In identified charged antiparticle to particle ratio measurement, the lower transverse momentum limit was set for the analysed particles as follows: 0.2 GeV/c (pions), 0.3 GeV/c (kaons), 0.4 GeV/c (protons and antiprotons).

The measurements were performed in a fiducial phase space of the forward-scattered protons of $0.04 < -t < 0.16$ GeV^2/c^2 and $0.02 < \xi < 0.2$. Figure 3.6 shows that the fraction of events containing at least two primary charged particles, $\epsilon_{n_{\mathrm{ch}}\geq 2}(\log_{10}\xi)$, is reduced by half for $\xi < 0.02$ compared to the region of larger ξ. In addition, the accidental background contribution at $\xi < 0.02$ is significant and approximately equal to 10% (Sec. 4). For these reasons the lower ξ cut was introduced. The upper ξ cut was required since the region of larger ξ is dominated by Double

Diffraction (DD) and ND (Sec. 4.2). The joint RP acceptance and track reconstruction efficiency was defined as the probability that true-level proton was reconstructed as a track passing the selection criteria. This efficiency was calculated as a function of $-t$ for three ranges of ξ separately and is shown in Fig. 3.7. Events were accepted only if the reconstructed values of $-t$ for protons fall within $> 5\%$ acceptance regions, which were required to be the same for each ξ region and similar to those defined in the elastic analysis [11]. Therefore, cuts on $0.04 < -t < 0.16$ GeV^2/c^2 were introduced. All measured observables are presented in three ξ regions: $0.02 < \xi < 0.05$, $0.05 < \xi < 0.1$ and $0.1 < \xi < 0.2$.

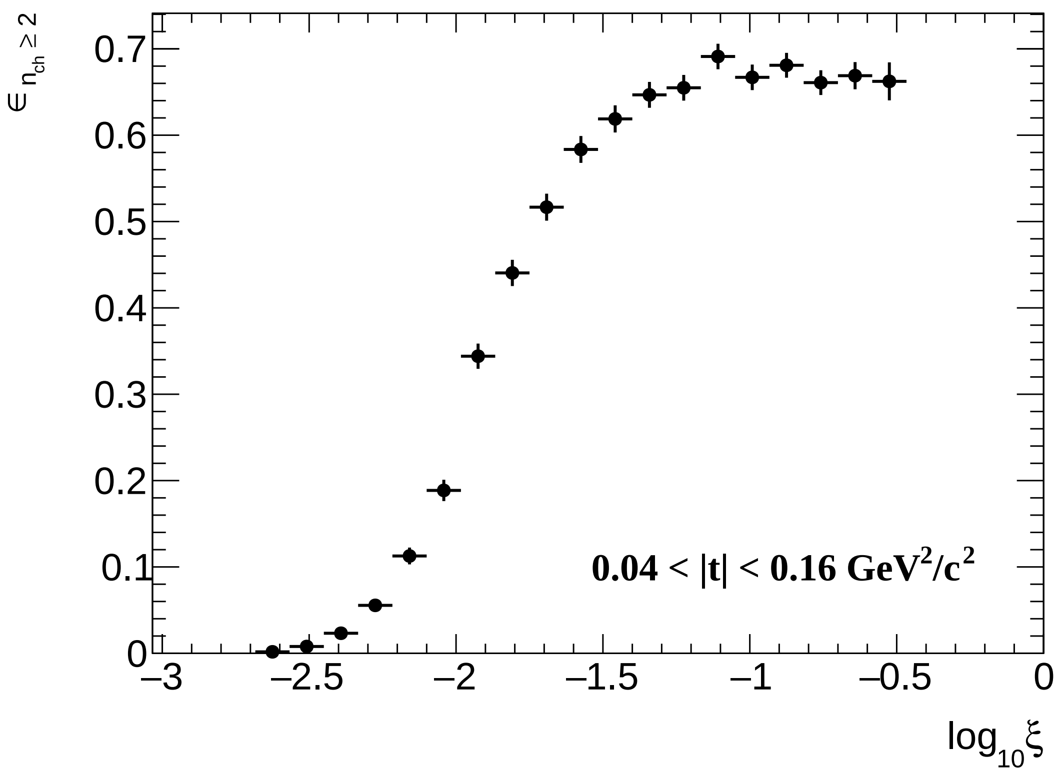

Figure 3.6: $\epsilon_{n_{\mathrm{ch}}\geq 2}$ as a function of $\log_{10}\xi$ calculated from PYTHIA 8 (MBR).

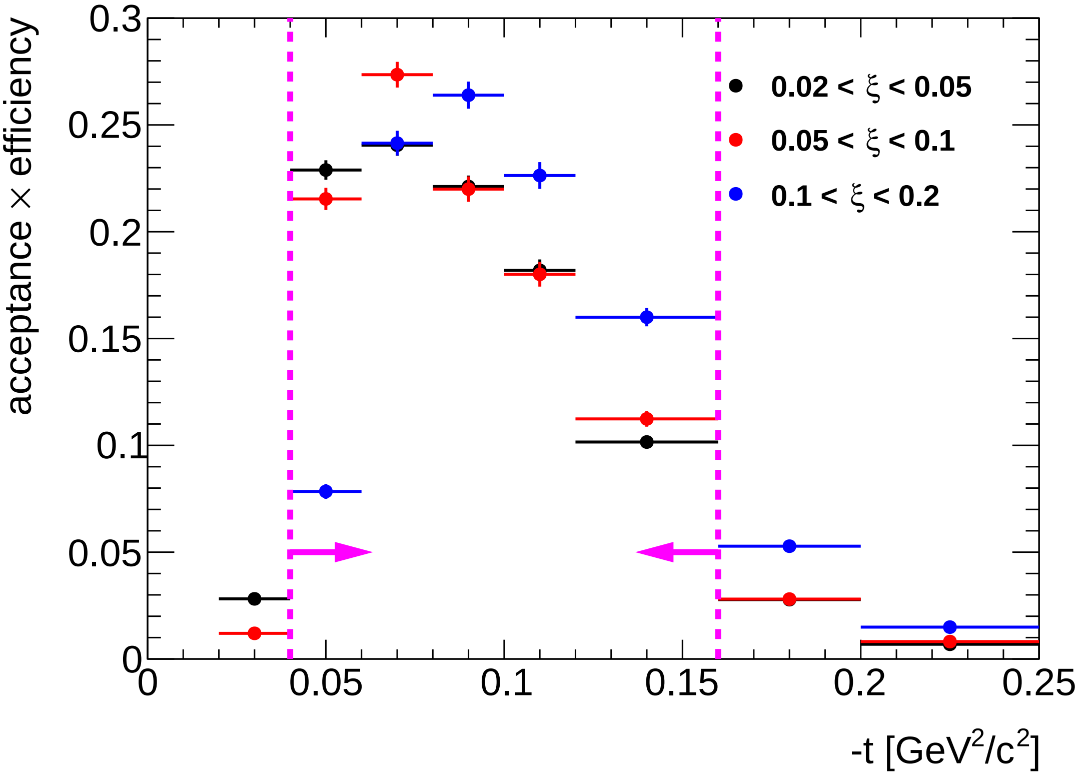

Figure 3.7: RP acceptance and track reconstruction efficiency as a function $-t$ in three ranges of ξ, calculated using PYTHIA 8 4C (SaS). Magenta lines indicate region accepted in the analysis.

4. Background Contribution

The background contributions to the charged-particle distributions can be divided into event-level and track-level backgrounds, and are described in detail below:

- Accidental background refers to events which do not originate from a single collision of two protons.
- Track backgrounds from non-primary tracks consist of secondary tracks and fake tracks; the first come mostly from decays, the short-lived particles with mean life $30 < \tau < 300$ ps, or secondary interactions with the detector dead material, while the second comes from the track reconstruction algorithms and out-of-time pile-up with no corresponding true particles.

Accidental Background

The accidental backgrounds (same bunch pile-up background) are quantified using data-driven method and defined as a process where in single bunch crossing there is coincidence of two interactions, where any single-side proton signal is collected in coincidence with an independent signal in the TPC+TOF+BBC detector. This type of background may come from the overlap of a signal in RP (proton from beam-halo, low mass SD process without activity in TOF, elastic or low mass Central Diffraction (CD) processes with undetected proton on the other side) with a signal in TPC+TOF+BBC (mainly ND events without forward-scattered proton).

The accidental background contribution was calculated from Zerobias data (colliding bunches), where two signatures of such background were investigated: the reconstructed proton in RP and the reconstructed vertex from TPC tracks matched with TOF. The analysis was done for each RP arm separately and thus the Zerobias data was firstly required to pass the following criteria:

1. no trigger in any RP or trigger in exactly one arm (two RPs) with exactly one reconstructed proton track in that arm,
2. veto on any signal in small BBC tiles or ZDC on the same side of the IP as the RP arm under consideration,
3. no or exactly one reconstructed vertex with at least two TOF-matched tracks passing the quality criteria. The latter includes also signal in BBC small tiles on the opposite side of the IP to the RP arm under study.

The sample of selected Zerobias data with total number of events N was divided into four classes:

$$N = N_{PS} + N_{RS} + N_{PT} + N_{RT} \tag{4.1}$$

where: N_{PS} is the number of events with reconstructed proton in exactly one RP and reconstructed TOF vertex, N_{RS} is the number of events with no trigger in any RP and reconstructed TOF vertex, N_{PT} is the number of events with reconstructed proton in exactly one RP and no reconstructed TOF vertex, N_{RT} is the number of events with no trigger in any RP and no reconstructed TOF vertex. Since the signature of the signal is a reconstructed proton in exactly one RP and a reconstructed TOF vertex, the number of such events can be expressed as:

$$N_{PS} = N\left(p_3 + p_1 p_2\right) \tag{4.2}$$

where: p_1 is the probability that there is a reconstructed proton in RP and there is no reconstructed TOF vertex, p_2 is the probability that there is no reconstructed proton in RP and there is a reconstructed TOF vertex, p_3 is the probability that there is a reconstructed proton in RP and there is a reconstructed TOF vertex (not accidental).

The other classes of events given in Eq. (4.1) can be expressed in terms of the above probabilities as:

$$\begin{aligned} N_{RS} &= N(1-p_1)p_2(1-p_3) \\ N_{PT} &= N(1-p_2)p_1(1-p_3) \\ N_{RT} &= N(1-p_1)(1-p_2)(1-p_3) \end{aligned} \tag{4.3}$$

Finally, the accidental background contribution $A_{\mathrm{bkg}}^{\mathrm{accidental}}$ is given by:

$$A_{\mathrm{bkg}}^{\mathrm{accidental}} = \frac{p_1 p_2}{p_3 + p_1 p_2} = \frac{N_{RS} N_{PT} N}{N_R N_T N_{PS}} \tag{4.4}$$

where: $N_R = N_{RS} + N_{RT}$ and $N_T = N_{PT} + N_{RT}$.

The shapes of the accidental background related to TPC distributions come from the above Zerobias data events which pass all the analysis selection except having no trigger in any RP. The templates corresponding to RP distributions are from protons in the above data sets but with no reconstructed TOF vertex. The normalization is given by Eq. (4.4). Figure 4.1 shows distributions of the reconstructed ξ with the accidental background contribution for events with proton reconstructed in EU, ED, WU and WD arms. Accidental background in the range of $0.02 < \xi < 0.2$ is below 1% and increases to 10% at $\xi < 0.02$. Unphysical negative values of reconstructed ξ are due to the detector resolution.

The selection of Zerobias events, which is not unique, may provide some bias to the normalization of the accidental background. As a systematic check, two criteria for Zerobias selection were changed to:

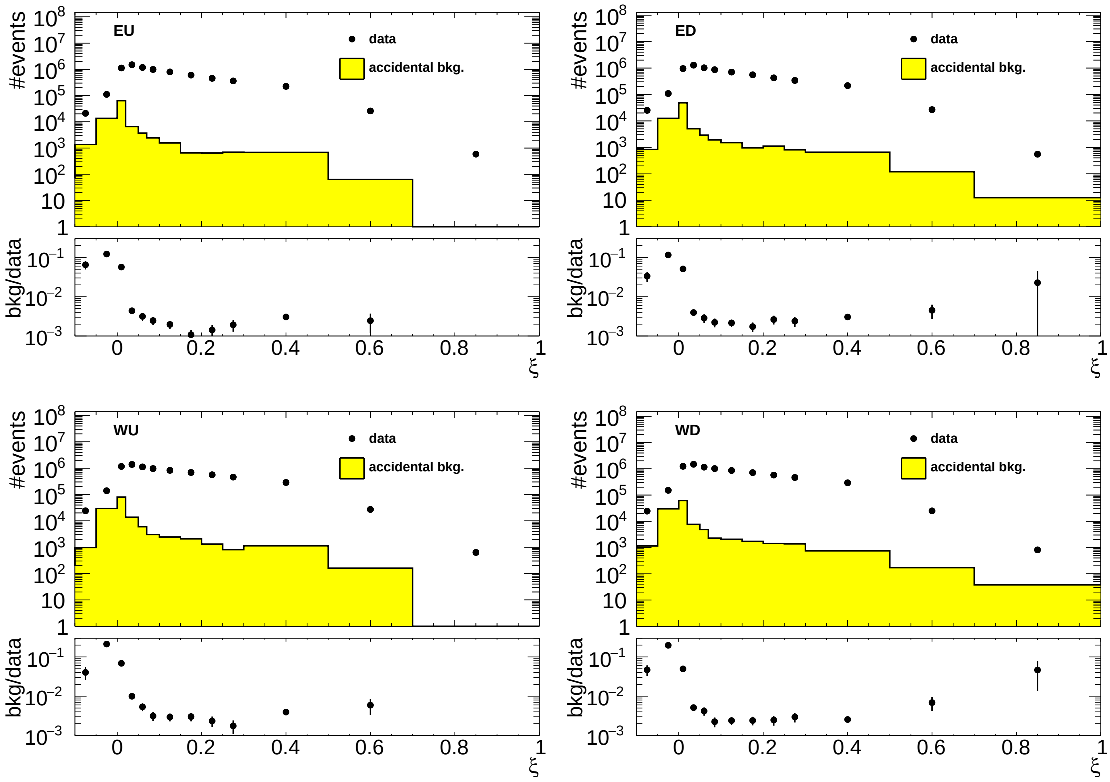

Figure 4.1: Uncorrected distributions of the reconstructed ξ for events with proton reconstructed in (top left) EU, (top right) ED, (bottom left) WU and (bottom right) WD arms. Data is shown as black markers, whereas the accidental background contribution is shown as yellow histogram. The ratio of accidental background and data is shown in the bottom panels.

1. no trigger in any RP or trigger in exactly one arm (two RPs) with *no more* than one reconstructed proton track in that arm, i.e. events with trigger signals in exactly one arm and without reconstructed proton track in that arm were also used,

2. no or exactly one reconstructed TOF vertex (*without any additional requirements*), i.e. events with a reconstructed TOF vertex that does not have at least two primary tracks satisfying the selection criteria (Sec. 3.1), or with a reconstructed TOF vertex that is out of the range of $|V_z| < 80$ cm, were also accepted. The requirement of signal in BBC small tiles remains unchanged.

As a result of this change, the accidental background normalization increases of about 50% with respect to the nominal value. A symmetric systematic uncertainty of 50% of the normalization of accidental background is applied to the measurement.

4.1 Background from Non-Primary Tracks

Reconstructed tracks matched to a non-primary particle, so-called background tracks, originate mainly from the following sources:

- decays of short-lived primary particles with strange quark content (mostly K^0, Λ^0),
- photons from π^0 and η decays which are converting to e^+e^-,
- hadronic interactions of particles with the beam-pipe or detector dead material.

Figure 4.2 (left) shows the background from non-primary tracks, $f_{\mathrm{bkg}}(p_{\mathrm{T}}, \eta)$, as a function of tracks' p_{T} and η, predicted by PYTHIA 8 SD model. There were no differences observed in the background contribution in different ξ ranges, hence, all three ξ ranges were merged for this study. The highest background fraction, which varies between $5 - 10\%$, was found to be at low p_{T}.

Figure 4.2 (right) shows the background track contribution to reconstructed tracks as a function of p_{T} and η calculated from EPOS SD+SD′. The differences between PYTHIA 8 and EPOS, which are up to 50% for $p_{\mathrm{T}} > 0.5$ GeV/c (as shown in Fig. 4.3), were symmetrized and taken as a systematic uncertainty.

There is also a small ($< 0.5\%$) contribution from fake tracks, $f_{\mathrm{fake}}(p_{\mathrm{T}}, \eta)$, i.e. tracks not associated with true-level particles, coming from out-of-time pile-up or formed by a random combination of TPC hits. The change by $\pm 100\%$ in this contribution was taken as a systematic uncertainty.

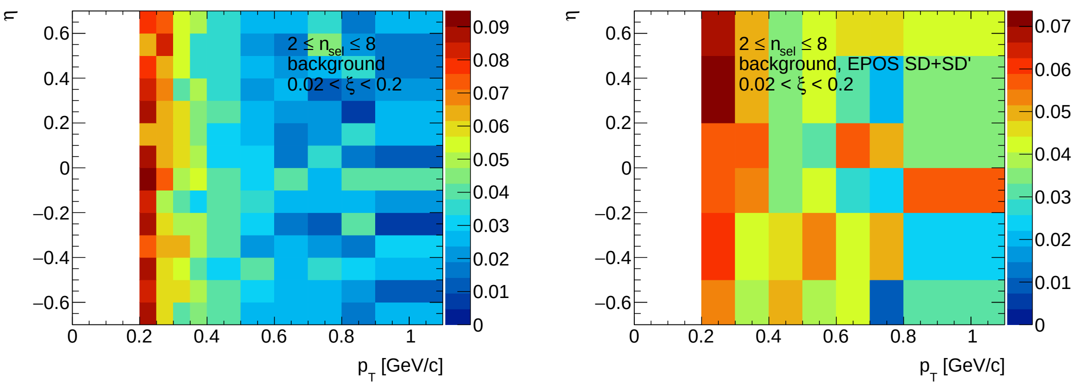

Figure 4.2: Distribution of fraction of selected tracks associated with non-primary particles in the range $0.02 < \xi < 0.2$ as predicted by (left) PYTHIA 8 4C (SaS) embedding and (right) EPOS SD+SD′.

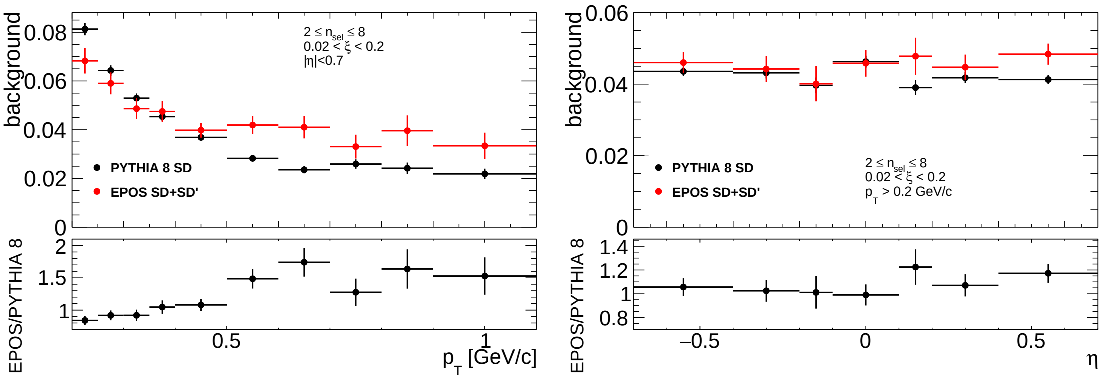

Figure 4.3: PYTHIA 8 SD and EPOS SD+SD′ predictions of fraction of selected tracks associated with non-primary particles as a function of (left) p_{T} and (right) η. The ratio of EPOS and PYTHIA 8 predictions is shown in the bottom panels.

Proton Background

Secondary particles can be created due to the interaction of particles with detector dead-material. The proton sample contains background from such protons knocked out from the detector materials [12]. Most of these protons have large DCA to the primary vertex and are not associated with it. However, the protons with small DCA are included in the primary track sample. Antiprotons do not have knockout background, hence the DCA tail is almost absent in their DCA distributions.

The fraction of knock-out background protons depends on a number of factors, including the amount of detector material, analysis cuts and the ξ of diffractive proton. While it is natural to calculate the fractions of primary and background protons in the MC sample, the MC models do not necessarily predict the fraction of knock-out background protons without any bias. Hence, data-driven methods should be used to calculate this type of background.

In order to correct for the knock-out background protons, sample enriched in proton background was used for background normalization, where DCA_{xy}, DCA_z and d_0 cuts were abandoned. Additionally, at least one, instead of exactly one, reconstructed vertex was allowed in this sample. Figures 4.4 and 4.5 show the DCA distributions of protons and antiprotons, respectively, for nominal (bottom) and background enriched (top) samples. The distributions for other p_{T} and ξ regions are shown in Appendix A. The protons and antiprotons are selected by a dE/dx cut of $-1 < n\sigma_{p,\bar{p}} < 3$ where $n\sigma_{p,\bar{p}}$ is given by Eq. (7.10). In some p_{T} regions, the dE/dx of (anti)protons and pions starts to overlap, hence, the asymmetric $n\sigma_{p,\bar{p}}$ cut was introduced in order to select as clean (anti)proton sample as possible. The fraction of knock-out protons within the selected sample is determined via MC template fits. The templates of reconstructed tracks with dE/dx corresponding to the proton and antiproton are obtained from PYTHIA 8 embedding MC separately for:

- primary (anti)protons,
- knock-out background protons (labeled as dead-material),
- fake tracks,
- secondary particles with dE/dx of (anti)proton (labeled as wrong PID - sec.),
- tracks associated with primary (anti)protons, but with the reconstructed vertex not matched to true-level primary vertex (labeled as wrong vtx),
- reconstructed track is partially matched to true-level particle (labeled as wrong match, track to true-level particle matching is described in [1]), i.e. track and true-level particle have appropriate number of common hit points but the distance between true-level particle and

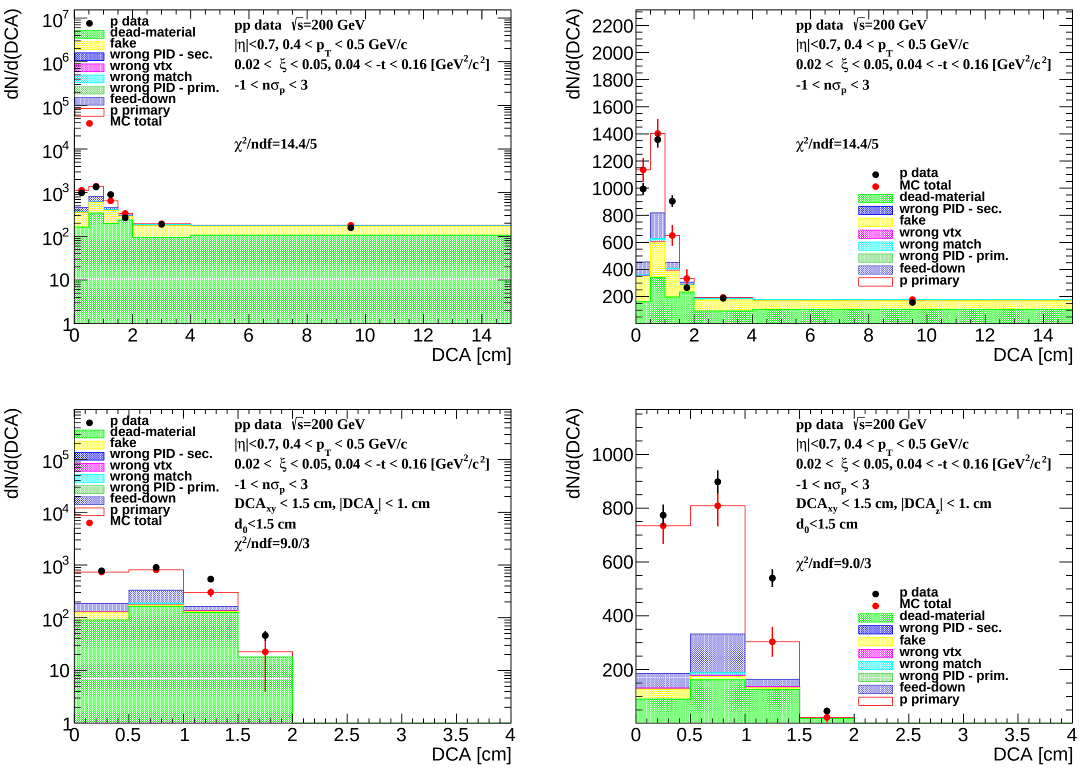

Figure 4.4: The DCA distributions of protons for $0.4 < p_T < 0.5$ GeV/c shown for single range of $0.02 < \xi < 0.05$ (shown in log and linear scale in left and right column, respectively). The MC contributions are shown after scaling the dead-material template to the tail of large DCA values, $2 <$ DCA < 15 cm. (top) Background enriched samples were used in the normalization procedure, whereas (bottom) the proton background was estimated from the nominal sample.

track is too large, $\delta^2(\eta, \phi) > (0.15)^2$, thus, track is not considered as primary particle according to discussion in [1],

- primary particles with dE/dx of (anti)proton (labeled as wrong PID - prim.),
- (anti)proton as a product of short-lived decays, mainly Λ^0 (labeled as feed-down).

First, the background enriched sample was analyzed (Fig. 4.4, top), where the template of knock-out background protons was normalized to the number of events in the fake-subtracted tail of the DCA distribution, $2 <$ DCA < 15 cm. Next the knock-out proton and fake background was subtracted from the DCA distribution and the sum of other templates was normalized to the number of events in the signal region, DCA < 1.5 cm.

The fraction of the knock-out proton background in the signal region, DCA < 1.5, was estimated from the nominal sample (Fig. 4.4, bottom), where DCA$_{xy}$, DCA$_z$ and d_0 track cuts were applied and exactly one reconstructed vertex was required. The normalization of each MC contribution was kept the same as that estimated for the background enriched sample. Figure 4.6 shows the knock-out proton background as a function of p_T in three ranges of ξ. The following functional form was found to describe the background protons:

$$f^p_{\mathrm{bkg}}(p_{\mathrm{T}}) = p_0 \exp(p_1 p_{\mathrm{T}}) \tag{4.5}$$

where p_0 and p_1 are free parameters obtained from a fit.

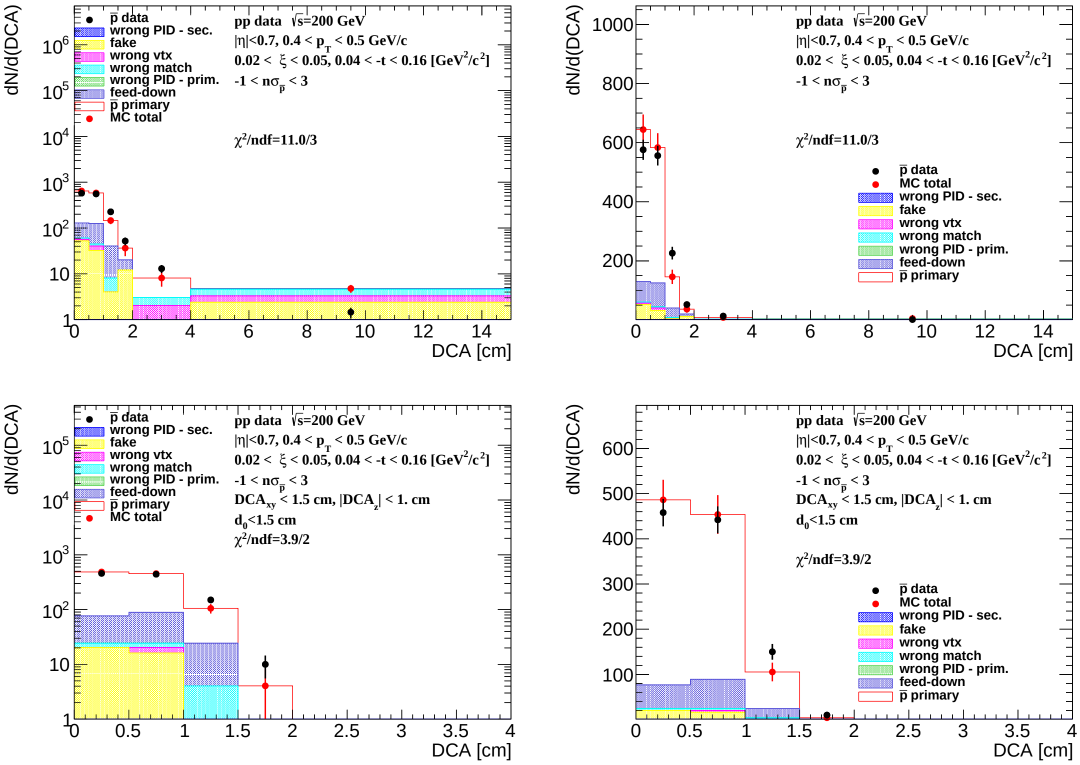

Figure 4.5: The DCA distributions of antiprotons for $0.4 < p_{\mathrm{T}} < 0.5$ GeV/c shown for one range of $0.02 < \xi < 0.05$ (log and linear scale in left and right column, respectively). The MC controbutions are shown as colour histograms. (top) Background enriched and (bottom) nominal samples were used.

The obtained fraction of knock-out background protons is approximately 20% at $p_{\mathrm{T}} = 0.45$ GeV/c and less than 10% at $p_{\mathrm{T}} = 1.0$ GeV/c. In PYTHIA 8 SD predictions (also shown in Fig. 4.6), such fraction is much smaller and equals to approximately 7% at $p_{\mathrm{T}} = 0.45$ GeV/c and about 5% at $p_{\mathrm{T}} = 1.0$ GeV/c. This may suggest that there are differences in the amount of dead material in front of TPC between data and simulation, which is consistent with the studies presented in [1].

Figure 4.5 shows the corresponding DCA distributions with MC templates for antiprotons, where the background from knock-out particles is not present. Therefore, there was no need for any fit to be performed in this comparison. The MC templates fairly well describe the DCA distribution for both, protons, after tunning the fraction of knock-out background to data, and antiprotons.

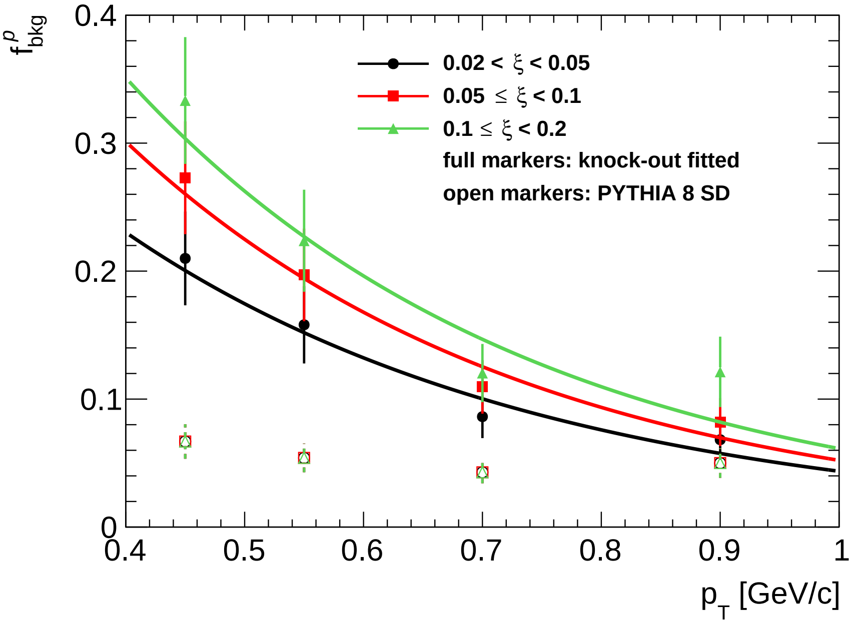

Figure 4.6: The fraction of knock-out proton background as a function of p_{T} in three ranges of ξ with fitted parametrizations. Full markers represent fitted knock-out background and open markers represent PYTHIA 8 SD predictions.

Systematic Uncertainty Related to Proton Background

The knock-out proton background estimation introduces systematic uncertainties. First, the normalization interval of the knock-out proton background template in the background enriched sample was changed to $4 < \mathrm{DCA} < 15$ cm. This introduced a relative systematic uncertainty of up to 30% for $p_{\mathrm{T}} \approx 0.9$ GeV/c.

The knock-out proton background contribution was parameterized as it is shown in Eq. (4.5). The systematic uncertainty related to the parameterization procedure was estimated by varying the parameters, p_0 and p_1, by their statistical uncertainties ($\pm 1\sigma$). As a result, a relative systematic uncertainties of about 10% were obtained.

Differences in the shape of the DCA distribution between data and MC can affect the knock-out proton background estimation procedure. Figure 4.7 (top left) shows the data to MC ratio of the number of events in the background dominated region, $2 < \mathrm{DCA} < 15$ cm. Since this region is used to estimate background normalization, and the shape of the DCA distribution in the data differs from that observed in the simulation, the predicted background in the $\mathrm{DCA} < 1.5$ cm region can change. Thus, the following functional form was used to estimate the slope between data and MC:

$$\frac{\mathrm{data}}{\mathrm{MC}}(\mathrm{DCA}) = A(\mathrm{DCA} - 8.5) + B \tag{4.6}$$

where A (slope) and B are fit free parameters. Differences in slope between data and MC were used to estimate how many more background tracks would fit into the signal region and a systematic uncertainty, which varies up to 5% for $0.02 < \xi < 0.05$, was introduced.

All above components of the systematic uncertainty related to the knock-out proton background, shown in Fig. 4.7, are added in quadrature. Those related to the fit range and the shape of the proton background are symmetrized. Figure 4.8 shows the fraction of knock-out proton background in three ranges of ξ and the total systematic uncertainty related to it.

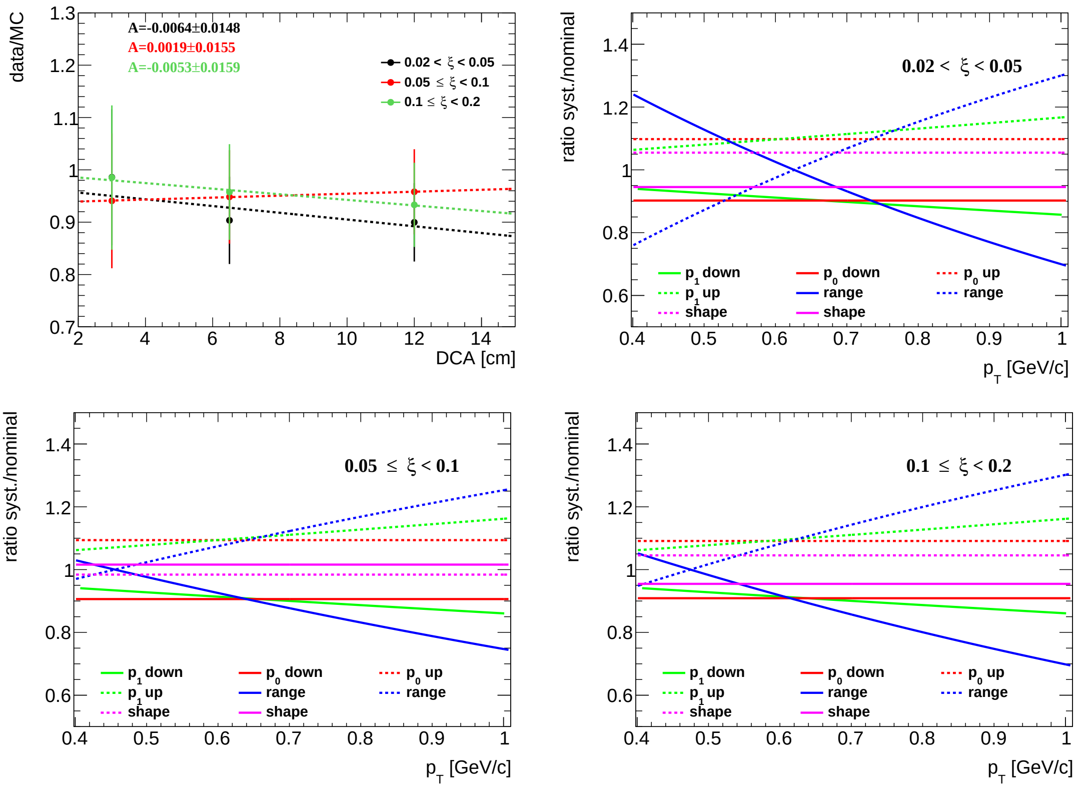

Figure 4.7: (top left) Data to MC ratio of the number of events in the background dominated region in three ranges of ξ with fitted functional form given by Eq. (4.6). (top right and bottom) Components of the systematic uncertainty related to the knock-out background protons contribution in three ξ ranges.

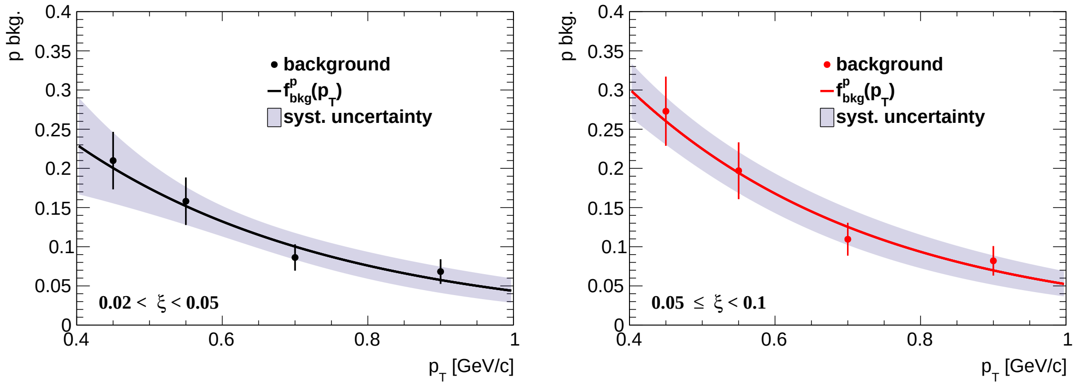

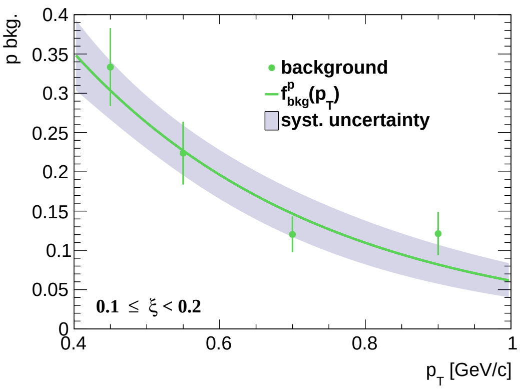

Figure 4.8: The fraction of knock-out proton background as a function of p_T with fitted parametrizations in three ranges of ξ: (top left) $0.02 < \xi < 0.05$, (top right) $0.05 < \xi < 0.1$ and (bottom) $0.1 < \xi < 0.2$. Gray bands represent total systematic uncertainties.

Pion Background

The pion spectra are corrected for weak decays (mainly of K^0_S and Λ^0), muon contribution and background from the detector dead-material interactions. The pion decay muons can be identified as pions due to the similar masses. These background contributions are obtained from PYTHIA 8 SD. Figure 4.9 shows the background contribution to the pion spectra as a function of p_{T} in three ranges of ξ, separately for π^- and π^+. Since there were negligible differences observed between these three ranges of ξ, the background contribution was averaged over ξ. The following parametrization was found to describe it:

$$f^{\pi}_{\mathrm{bkg}}\,(p_{\mathrm{T}}) = a_0 \exp(a_1 p_{\mathrm{T}}) + a_2 p_{\mathrm{T}}^2 + a_3 p_{\mathrm{T}} \tag{4.7}$$

where a_i, $i = 0, \ldots, 3$ are free parameters of the fitted function.

The pion background contribution varies between 5% at low-p_{T} ($p_{\mathrm{T}} = 0.25$ GeV/c) and about 1% at $p_{\mathrm{T}} = 1.0$ GeV/c for both negatively and positively charged pions. In addition, the background was calculated from EPOS SD+SD′ for the full range of ξ. The differences between PYTHIA 8 and EPOS are up to 1% for π^-.

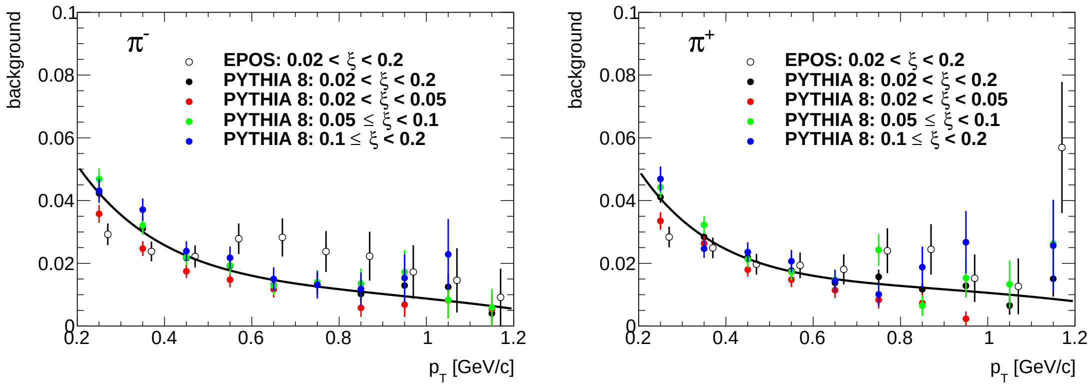

Figure 4.9: Pion background fraction as a function of p_{T} shown separately for (left) negatively and (right) positively charged pions in three ranges of ξ: (red) $0.02 < \xi < 0.05$, (green) $0.05 < \xi < 0.1$, (blue) $0.1 < \xi < 0.2$. (full black points) The pion background averaged over three ranges of ξ with fitted parametrization is also shown. Open black points represent EPOS predictions for the full ξ range.

4.2 Control Plots

Events, in which forward-scattered proton and reconstructed TOF vertex are the result of the same pp interaction, may originate from ND, DD, SD, and CD processes. It is preferred to estimate the background contribution from data, using dedicated control regions. Since such regions were not found, the relative contributions from the above processes were estimated from MC models and are therefore model dependent. Tracks reconstructed in RPs may also be:

- forward-scattered protons produced in the SD, CD or DD diffractive systems or from ND events,
- secondary particles from showering initiated by interaction of forward-scattered protons with beam-line elements. This contribution is negligible.

Figure 4.10 shows the uncorrected ξ and t distributions in data compared to various MC models: PYTHIA 8 A2 (MBR), PYTHIA 8 A2 (MBR-tuned), PYTHIA 8 4C (SaS) and EPOS. The MC distributions are split into SD, ND, DD and CD components. For EPOS, SD$'$ is separated from the ND events. Additionally, the accidental background is also shown. PYTHIA 8 A2 (MBR) predictions, shown in Fig. 4.10 (a-b), do not agree with the data, especially there is small number of events in the region of large values of ξ. This effect may be due to the scaling factors, which are introduced in PYTHIA 8 to artificially suppress diffractive cross sections in the high mass region, or due to too large Pomeron intercept ($\epsilon = 0.104$). Therefore, additional two samples of PYTHIA 8 were generated: without this artificial suppression (MBR-tuned) and with $\epsilon = 0$ (SaS). Their predictions, shown in Fig. 4.10 (c-f), agree much better with the data than PYTHIA 8 A2 (MBR) and result also in a suppression of non-SD events. Amongst PYTHIA 8 models, PYTHIA 8 A2 (MBR-tuned) shows the best agreement with the data. EPOS predictions, shown in Fig. 4.10 (g-h), describes data better than PYTHIA 8 but shows a dominant contribution of SD$'$ events. The CD contribution in EPOS is several times greater than in PYTHIA 8 (MBR), but it was never tuned to describe any data, as opposed to PYTHIA 8 (MBR) in which the CD cross sections are constrained by CDF measurements [13]. The CD component in the SaS model is based on simple scaling assumption, therefore, it is not usually used by the experimental communities. All MCs predict significant DD and ND background at large ξ, thereby the analysis was limited to $\xi < 0.2$.

Figures 4.11 to 4.13 show the uncorrected distributions of variables used in the later analysis: n_{sel}, p_{T} an $\bar{\eta}$. The contributions from non-SD (except EPOS SD$'$) interactions differ a bit between each other, i.e. EPOS predicts significantly larger CD contribution, whereas DD and ND are suppressed in PYTHIA 8 A2 (MBR-tuned) and PYTHIA 8 4C (SaS). PYTHIA 8 A2 (MBR) is used as the default model of non-SD contribution subtracted from the data with systematic uncertainty $\pm 50\%$, which covers all differences between the models except EPOS SD$'$. In this analysis EPOS SD$'$ is considered as an alternative to PYTHIA 8 SD model of events with forward-scattered proton in the final state, where one of the proton remnants hadronizes back to a single proton (non-diffractive process), while in PYTHIA 8 the initial proton stays intact (diffractive process). As a consequence, results are compared with the sum of SD and SD$'$ processes for EPOS model.

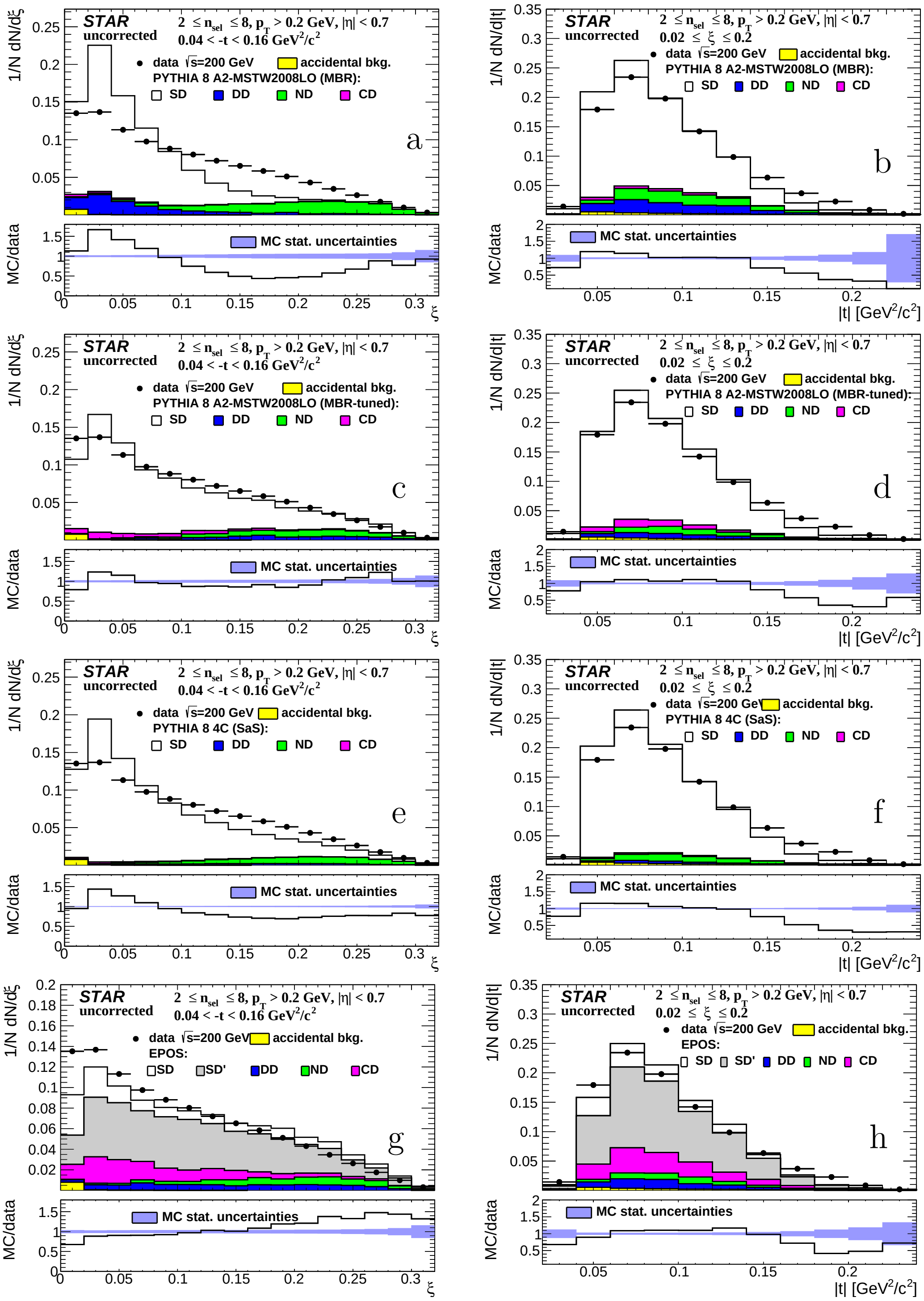

Figure 4.10: Uncorrected distributions of data compared to various MC models: (a-b) PYTHIA 8 A2 (MBR), (c-d) PYTHIA 8 A2 (MBR-tuned), (e-f) PYTHIA 8 4C (SaS) and (g-h) EPOS, as a function of (left column) ξ and (right column) $|t|$. The ratio of MC predictions and data is shown in the bottom panels.

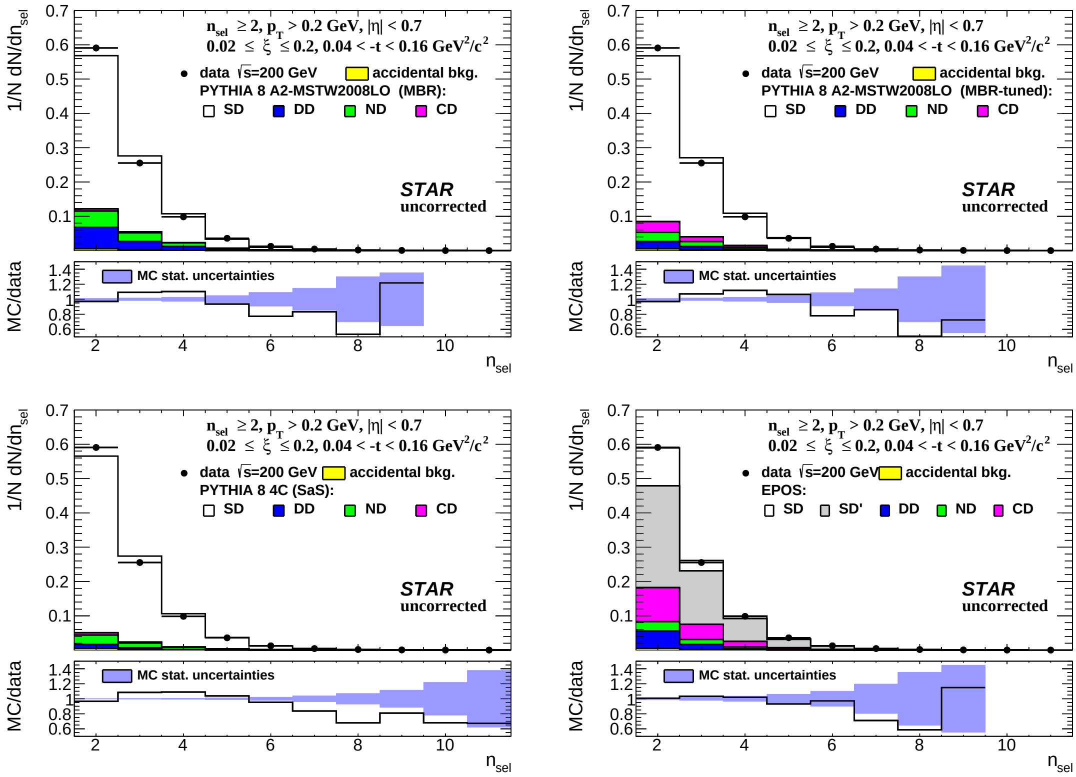

Figure 4.11: Uncorrected distributions of data compared to various MC models: (top left) PYTHIA 8 A2 (MBR), (top right) PYTHIA 8 A2 (MBR-tuned), (bottom left) PYTHIA 8 4C (SaS) and (bottom right) EPOS, as a function of n_{sel}. The ratio of MC predictions and data is shown in the bottom panels.

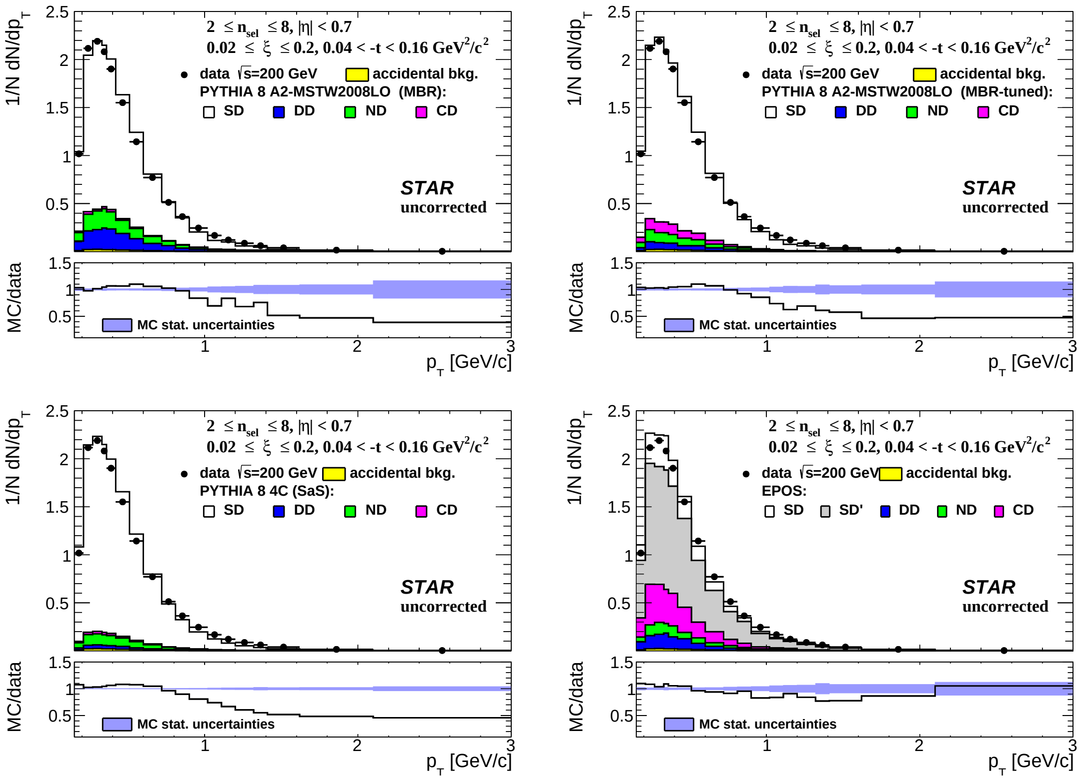

Figure 4.12: Uncorrected distributions of data compared to various MC models: (top left) PYTHIA 8 A2 (MBR), (top right) PYTHIA 8 A2 (MBR-tuned), (bottom left) PYTHIA 8 4C (SaS) and (bottom right) EPOS, as a function of p_{T}. The ratio of MC predictions and data is shown in the bottom panels.

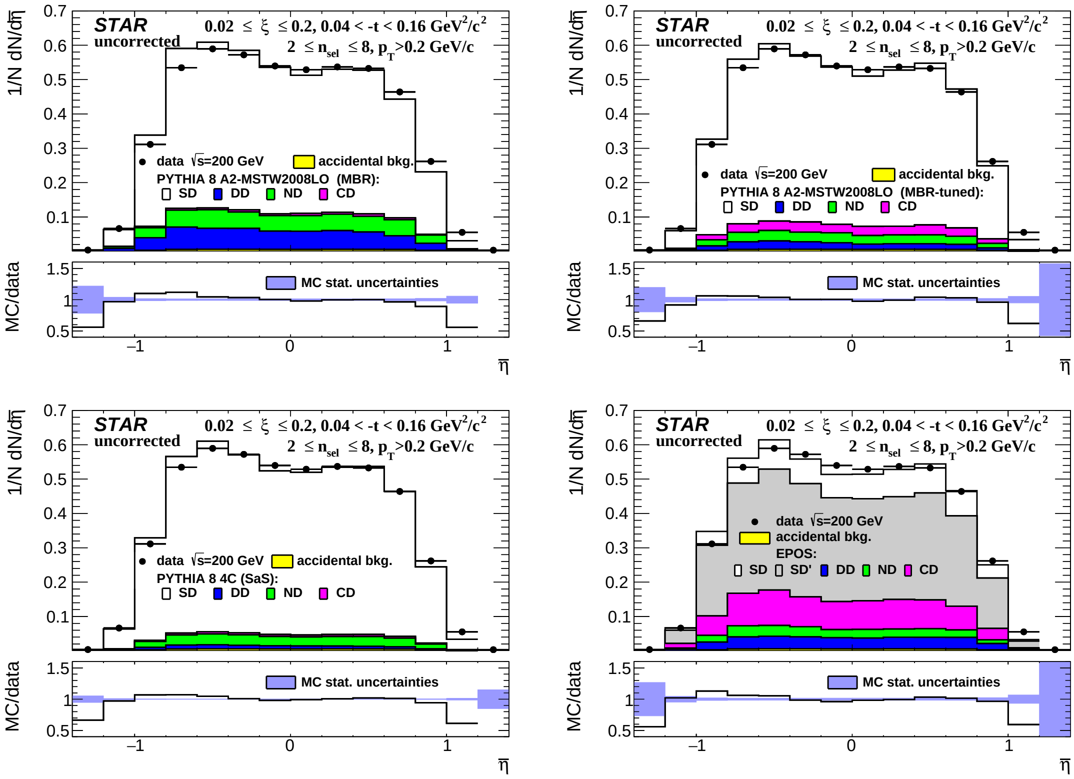

Figure 4.13: Uncorrected distributions of data compared to various MC models: (top left) PYTHIA 8 A2 (MBR), (top right) PYTHIA 8 A2 (MBR-tuned), (bottom left) PYTHIA 8 4C (SaS) and (bottom right) EPOS, as a function of $\bar{\eta}$. The ratio of MC predictions and data is shown in the bottom panels.

5. Selection Efficiencies

5.1 Vertex Reconstruction

When the charged-particle multiplicity is low, the vertex-finding algorithm sometimes fails to find the primary vertex. In addition, at high luminosity, vertex finder can fail due to the contribution of pile-up interactions, providing a wrong reconstructed vertex. In the study of vertex reconstruction efficiency we required at least two reconstructed global tracks $n_{\mathrm{sel}}^{\mathrm{global}} \geq 2$ passing all the quality cuts listed in Sec 3.1, except vertex-related cuts on DCA_{xy} and DCA_{z}, and associated to true-level primary particles. Additionally, MC events were accepted if the z-coordinate of the true-level primary vertex was between -80 and 80 cm and $n_{\mathrm{ch}} \geq 2$. All corrections, described in this section, were calculated in three ranges of ξ separately using PYTHIA 8 SD embedding MC.

The global tracks (not necessarily associated to a true-level primary particles), which are used by the vertex-finder algorithm, had to pass the following quality cuts:

1. tracks must be matched with hits reconstructed in TOF,
2. the number of the TPC hits used in the helix fit $N_{\mathrm{hits}}^{\mathrm{fit}}$ must be greater than 20,
3. the ratio of the number of TPC hits used in the helix fit to the number of possible TPC hits $N_{\mathrm{hits}}^{\mathrm{fit}}/N_{\mathrm{hits}}^{\mathrm{poss}}$ must be greater than 0.52,
4. the transverse impact parameter with respect to the beamline d_0 must be less than 2 cm,
5. the track's transverse momentum p_{T} must be greater than 0.2 GeV/c.

The above track selection criteria are different than those used in the nominal analysis. Primary vertex reconstruction efficiency and fake vertex rate were calculated as a function of the number of global tracks used in vertexing $n_{\mathrm{vrt}}^{\mathrm{global}}$ instead of $n_{\mathrm{sel}}^{\mathrm{global}}$ ($n_{\mathrm{vrt}}^{\mathrm{global}} \geq n_{\mathrm{sel}}^{\mathrm{global}}$).

In the nominal analysis exactly one vertex with $n_{\mathrm{sel}} \geq 2$ is required. However, in the study of vertex reconstruction, events with additional vertices were studied. Therefore, we define the best vertex as the reconstructed vertex with the highest number of TOF-matched tracks. This vertex does not have to be associated to true-level primary vertex (fake or secondary vertex). The algorithm, which matches reconstructed vertices to true-level vertices, checks for reconstructed tracks originating from them. If at least one reconstructed track is assigned to a true-level particle, then the reconstructed vertex is assigned to the true-level vertex from which the true-level particle originates. Since the fake vertices (not matched to the true-level primary vertex) are allowed in the analysis, the overall vertex-finding efficiency, $\epsilon_{\mathrm{vrt}}\left(n_{\mathrm{vrt}}^{\mathrm{global}}\right)$, is expressed as:

$$\epsilon_{\mathrm{vrt}}\left(n_{\mathrm{vrt}}^{\mathrm{global}}\right) = \epsilon_{\mathrm{vrt}}^{\mathrm{best}}\left(n_{\mathrm{vrt}}^{\mathrm{global}}\right) + \delta_{\mathrm{vrt}}^{\mathrm{fake}}\left(n_{\mathrm{vrt}}^{\mathrm{global}}\right) \tag{5.1}$$

where:

$\epsilon_{\mathrm{vrt}}^{\mathrm{best}}\left(n_{\mathrm{vrt}}^{\mathrm{global}}\right)$ is the primary vertex reconstruction efficiency, determined as the ratio of the number of good reconstructed events (best primary vertex with $n_{\mathrm{sel}} \geq 2$ matched to the true-level primary vertex) to the number of input MC events,

$\delta_{\mathrm{vrt}}^{\mathrm{fake}}\left(n_{\mathrm{vrt}}^{\mathrm{global}}\right)$ is the fake vertex rate, determined as the ratio of the number of good reconstructed events (best primary vertex with $n_{\mathrm{sel}} \geq 2$ not matched to the true-level primary vertex) to the number of input MC events. Due to the contribution of pile-up, it is possible that the best vertex originates from fake tracks instead of true-level particles.

The vertex-finding efficiency as a function of $n_{\rm vrt}^{\rm global}$, shown in Fig. 5.1 (left), is larger than 75% for all $n_{\rm vrt}^{\rm global}$. However, for $n_{\rm vrt}^{\rm global} > 8$, there are more fake than true-level primary vertices. When there are exactly two global tracks used in the vertex reconstruction, $n_{\rm vrt}^{\rm global} = 2$, the vertex-finding efficiency depends on the longitudinal distance between these tracks $|\Delta z_0|$. Therefore, the vertex-finding efficiency for such events $\epsilon_{\rm vrt}\left(|\Delta z_0|\right)$ is given by:

$$\epsilon_{\rm vrt}\left(|\Delta z_0|\right) = \epsilon_{\rm vrt}^{\rm best}\left(|\Delta z_0|\right) + \delta_{\rm vrt}^{\rm fake}\left(|\Delta z_0|\right) \tag{5.2}$$

where: $\epsilon_{\rm vrt}^{\rm best}\left(|\Delta z_0|\right)$ is the primary vertex reconstruction efficiency, $\delta_{\rm vrt}^{\rm fake}\left(|\Delta z_0|\right)$ is the fake vertex rate.

Figure 5.1 (right) shows the vertex-finding efficiency for events with $n_{\rm vrt}^{\rm global} = 2$. This efficiency is smaller than 20% for tracks with $|\Delta z_0| > 2$ cm, hence the analysis was limited to events with $|\Delta z_0| < 2$ cm, when $n_{\rm vrt}^{\rm global} = 2$. The rate of fake vertices is negligibly low (open points overlap with full points).

Events are rejected if more vertices are reconstructed in addition to the best one. Rejected events can be classified as:

a) two or more additional vertices,

b) additional secondary vertex from interactions with the detector dead-material,

c) additional fake vertex,

d) additional primary vertex (vertex splitting or background vertex reconstructed as best vertex),

e) additional secondary vertex from the decay.

The fraction of such events, $f_{\rm vrt}^{\rm veto}\left(n_{\rm vrt}^{\rm global}\right)$, is given by:

$$\begin{aligned} f_{\rm vrt}^{\rm veto}\left(n_{\rm vrt}^{\rm global}\right) &= \frac{\text{number of events with more than one reconstructed TOF vertex}}{\text{number of events with at least one reconstructed TOF vertex}} \\ &= f_a + f_b + f_c + f_d + f_e \end{aligned} \tag{5.3}$$

where f_a to f_e are the fractions of events with additional vertices, with labels corresponding to the items in the listing above.

As before, the fraction was calculated as a function of $|\Delta z_0|$ for events with $n_{\rm vrt}^{\rm global} = 2$. Figure 5.2 shows the fraction of multi-vertex events with respect to the $n_{\rm vrt}^{\rm global}$. There is a large fraction of events ($> 90\%$) with additional background vertices for $n_{\rm vrt}^{\rm global} \geq 9$, what would result in large correction factor. Hence, the analysis was limited to events with $n_{\rm sel}^{\rm global} \leq 8$ ($n_{\rm sel}^{\rm global} \leq$

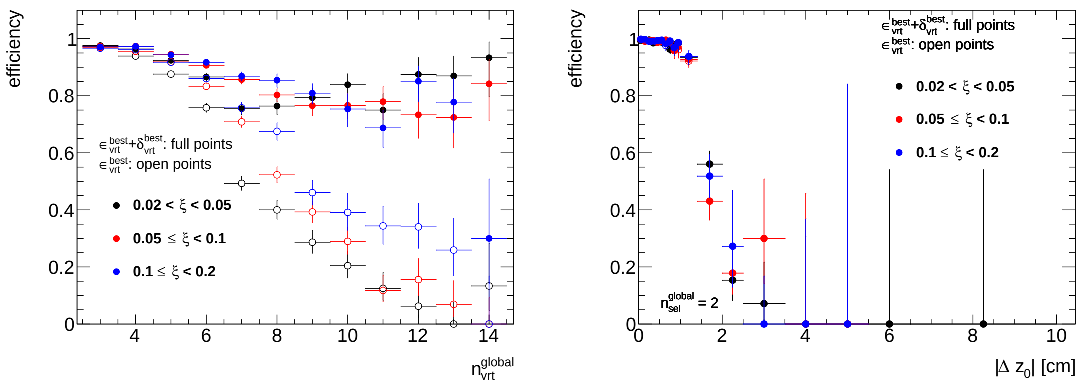

Figure 5.1: Vertex-finding efficiency in three ranges of ξ as a function of (left) $n_{\rm vrt}^{\rm global}$ and (right) with respect to the $|\Delta z_0|$ between reconstructed tracks in events with $n_{\rm vrt}^{\rm global} = 2$.

$n_{\mathrm{vrt}}^{\mathrm{global}}$). The total fraction of multi-vertex events, $f_a + f_b + f_c + f_d + f_e$, as a function of $n_{\mathrm{vrt}}^{\mathrm{global}}$ and $|\Delta z_0|$, shown in Fig. 5.3, demonstrates that $f_{\mathrm{vrt}}^{\mathrm{veto}}(|\Delta z_0|)$ is very small ($< 2\%$) for events with $n_{\mathrm{vrt}}^{\mathrm{global}} = 2$.

Although, the analysis was limited to $n_{\mathrm{sel}}^{\mathrm{global}} \leq 8$ ($n_{\mathrm{sel}}^{\mathrm{global}} \leq n_{\mathrm{vrt}}^{\mathrm{global}}$), a fraction of events with additional background vertices was still relatively large. Since most of these additional vertices are fake (and as accidental not correlated with true-level primary distributions), it was checked whether the charged-particle multiplicity distributions are different for events with and without reconstructed fake vertices. These distributions, as shown in Fig 5.4, are in good agreement, thus, above studies of vertex reconstruction were repeated using MC events that do not contain reconstructed fake vertices. It means that events with additional fake vertex were rejected (similarly to the analysis of real data) and no correction is needed for such losses since it only affects overall normalization (not the shapes of distributions under study). The vertex-finding efficiency, which was calculated from such events, is shown in Fig. 5.5. It is greater than 95% for events with $2 \leq n_{\mathrm{vrt}}^{\mathrm{global}} \leq 8$. In addition, the corresponding fraction of multi-vertex events, shown in Figs. 5.6

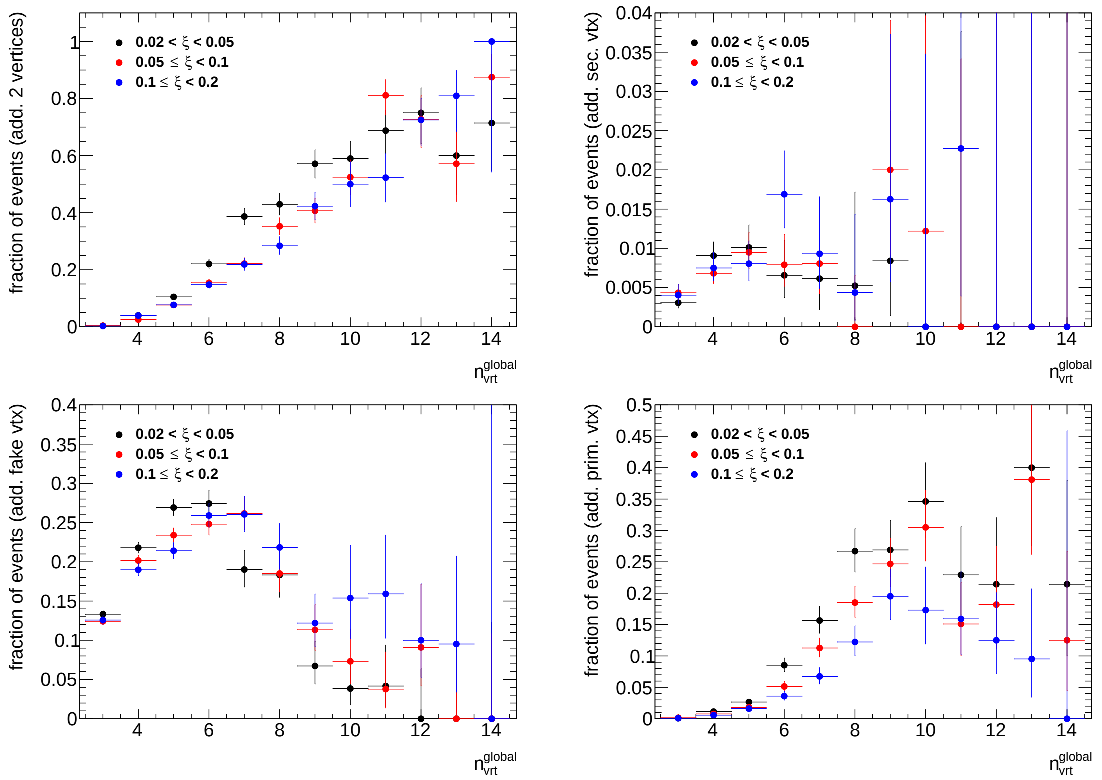

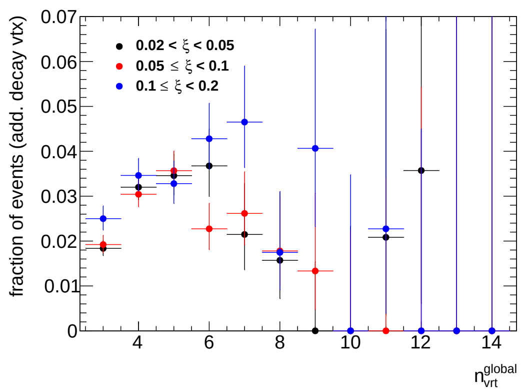

Figure 5.2: Fraction of multi-vertex events with respect to the $n_{\mathrm{vrt}}^{\mathrm{global}}$ in three ranges of ξ. Each contribution is shown separately: (top left) more than one additional vertices, (top right) additional secondary vertex from the interactions with the detector dead-material, (middle left) additional fake vertex, (middle right) additional primary vertex and (bottom) additional decay vertex.

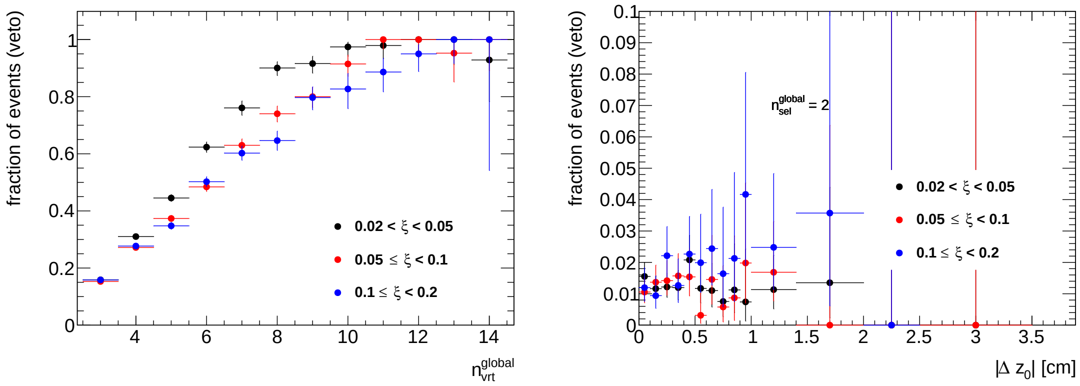

Figure 5.3: Total fraction of multi-vertex events as a function of (left) $n_{\mathrm{vrt}}^{\mathrm{global}}$ for events with $n_{\mathrm{vrt}}^{\mathrm{global}} > 2$ and (right) $|\Delta z_0|$ for events with $n_{\mathrm{vrt}}^{\mathrm{global}} = 2$ in three ranges of ξ.

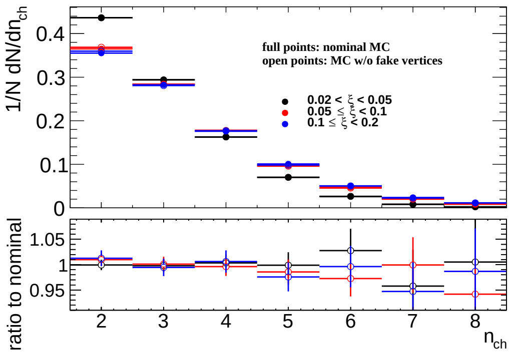

Figure 5.4: Normalized charged-particle multiplicity distributions in three ranges of ξ calculated from PYTHIA 8 SD embedding MC for (full points) all generated events and (open points) events without reconstructed fake vertices.

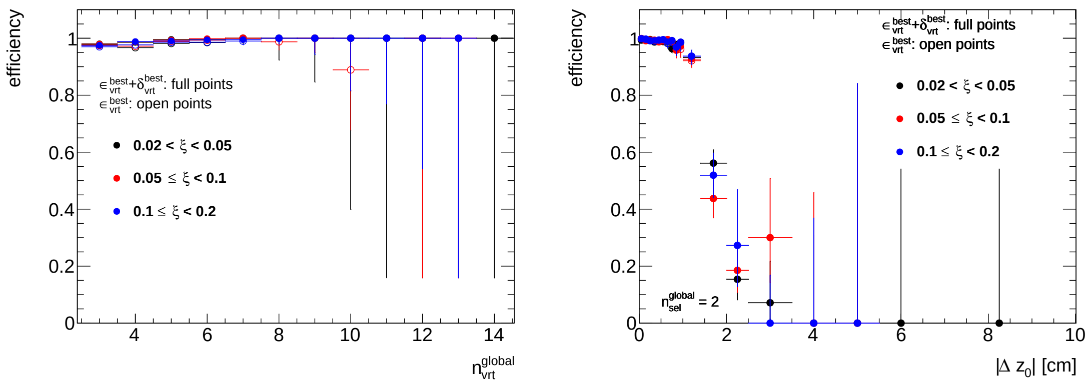

Figure 5.5: Vertex-finding efficiency in three ranges of ξ as a function of (left) $n_{\mathrm{vrt}}^{\mathrm{global}}$ and (right) with respect to the $|\Delta z_0|$ between reconstructed tracks in events with $n_{\mathrm{vrt}}^{\mathrm{global}} = 2$. Only events that do not contain additional fake vertices were used.

and 5.7, is smaller than 20%. Since fake vertices were rejected from this study, the f_c term from Eq. (5.3) is equal to 0. The correction factors calculated from MC events that do not contain reconstructed fake vertices were used in the analysis instead of the one obtained from the full MC sample.

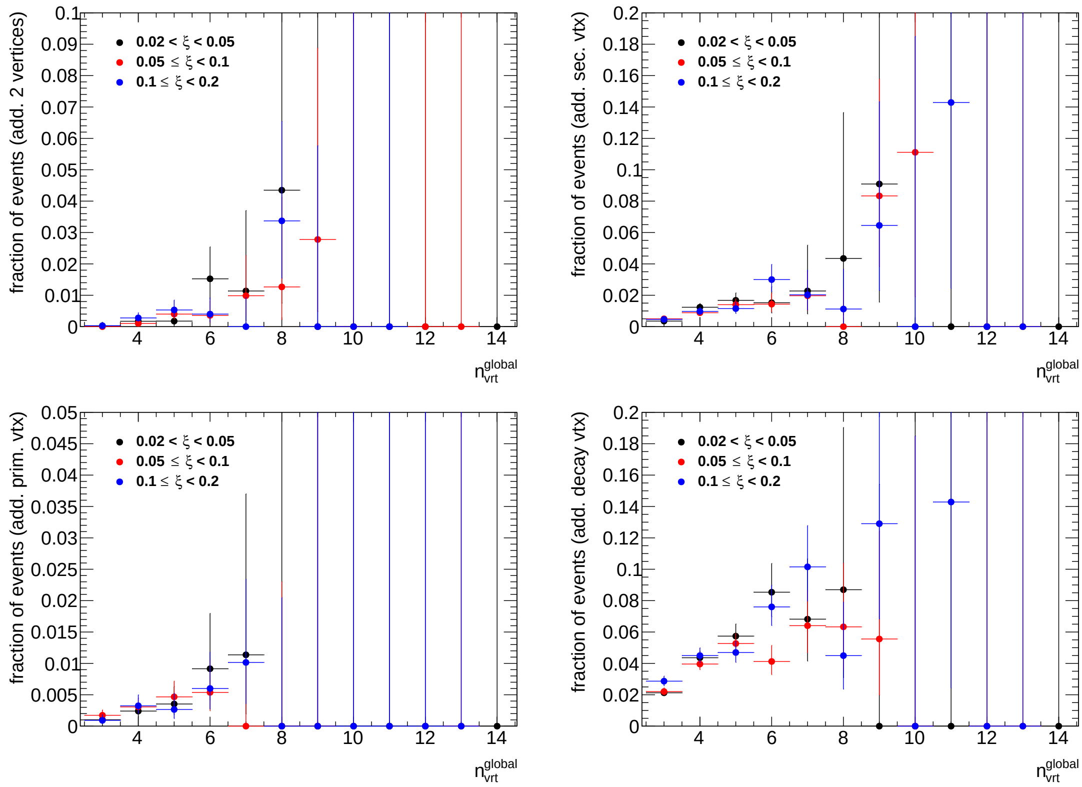

Figure 5.6: Fraction of multi-vertex events with respect to the $n_{\mathrm{vrt}}^{\mathrm{global}}$ in three ranges of ξ. Each contribution is shown separately: (top left) more than one additional vertices, (top right) additional secondary vertex from the interactions with the detector dead-material, (bottom left) additional primary vertex and (bottom right) additional decay vertex. Only events that do not contain additional fake vertices were used.

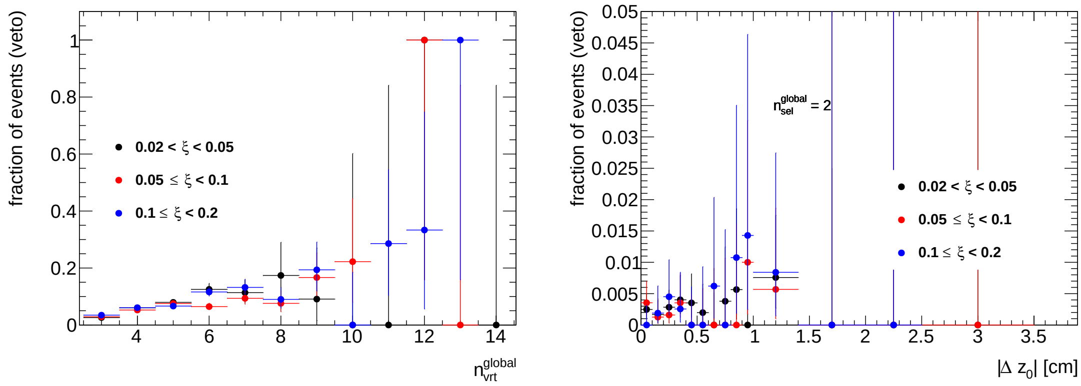

Figure 5.7: Total fraction of multi-vertex events as a function of (left) $n_{\mathrm{vrt}}^{\mathrm{global}}$ for events with $n_{\mathrm{vrt}}^{\mathrm{global}} > 2$ and (right) $|\Delta z_0|$ for events with $n_{\mathrm{vrt}}^{\mathrm{global}} = 2$ in three ranges of ξ. Only events that do not contain additional fake vertices were used.

5.2 Correction to BBC-Small

The SDT trigger conditions imposed a signal in RPs and a veto on any signal in the same-side small BBC tiles, whereas a signal in the opposite-side BBC-small was required by the offline event selection. These requirements were imposed in order to accept only events with rapidity gap and reduce DD, ND and accidental backgrounds. A joined BBC-small efficiency, ϵ_{BBC}, was obtained as a function of each measured quantity using PYTHIA 8 4C (SaS) SD embedded into Zerobias data, EPOS SD+SD$'$ and HERWIG SD MC. The efficiency was calculated for events within fiducial region as follows:

$$\epsilon_{\mathrm{BBC}} = \frac{\text{number of MC events satisfying the BBC-small selection criteria}}{\text{number of MC events}} \tag{5.4}$$

Figures 5.8 to 5.10 show the fraction of generated true-level MC events, within the fiducial region of the measurement, in which the selection criteria on BBC-small signal and veto are fulfilled. The efficiency weakly depends on the measured variables (n_{ch}, p_{T} and $\bar{\eta}$). In addition, veto, signal and joined BBC-small efficiencies are presented separately as a function of ξ in Fig. 5.11. The ϵ_{BBC} strongly depends on ξ and varies from about 90% for events with ξ within $0.02 - 0.05$ to about 60% for events with $0.1 < \xi < 0.2$. However, measurements of corrected ξ distributions are out of the scope of this analysis.

Data is corrected for BBC-small efficiency using PYTHIA 8 4C (SaS). The uncertainty related to this correction is estimated by using HERWIG and EPOS SD+SD$'$ samples, where the hadronization models are different from that used in PYTHIA 8. Figure 5.12 shows the PYTHIA 8 prediction on BBC efficiency divided by the HERWIG prediction in three ranges of ξ. The deviations between these two models are of the order of 4% at $0.02 < \xi < 0.05$, 2% at $0.05 < \xi < 0.1$ and about 10% at $0.1 < \xi < 0.2$. The differences between PYTHIA 8 and EPOS SD+SD$'$ predictions are shown in Fig. 5.13. Most of them are of the order of 3%, except $n_{\mathrm{ch}} \leq 3$ for which the difference varies up to 6%. The maximum difference between PYTHIA 8 and HERWIG/EPOS hadronization models is used as systematic uncertainty.

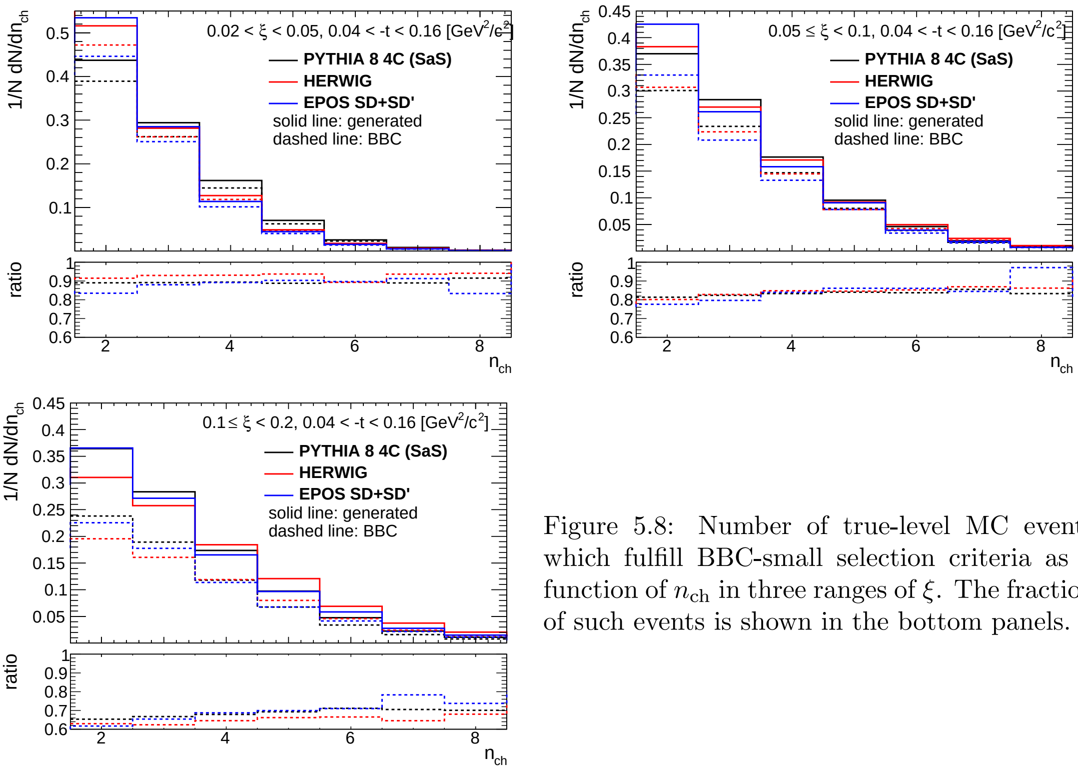

Figure 5.8: Number of true-level MC events which fulfill BBC-small selection criteria as a function of n_{ch} in three ranges of ξ. The fraction of such events is shown in the bottom panels.

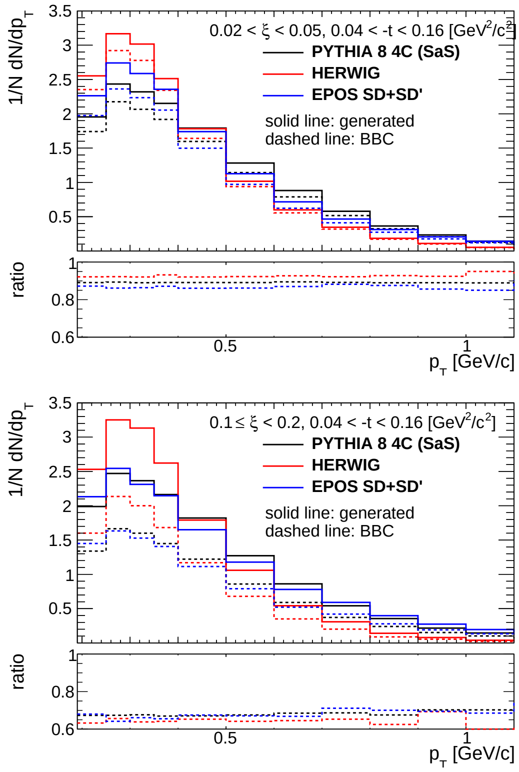

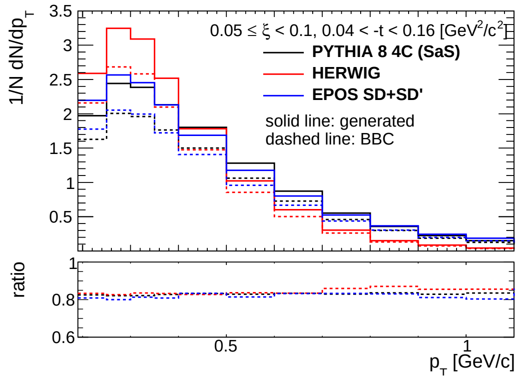

Figure 5.9: Number of true-level MC events which fulfill BBC-small selection criteria as a function of p_{T} in three ranges of ξ. The fraction of such events is shown in the bottom panels.

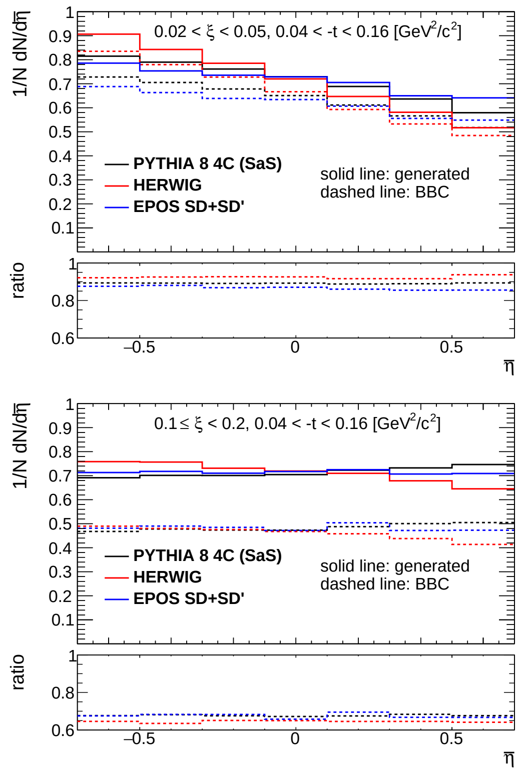

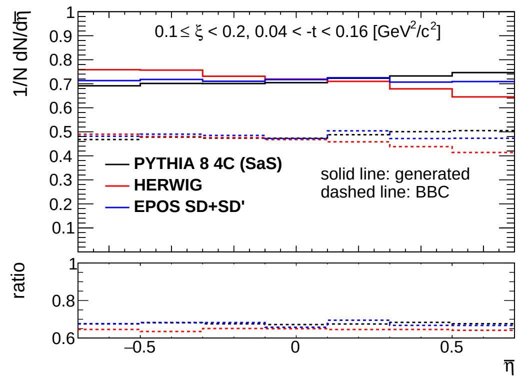

Figure 5.10: Number of true-level MC events which fulfill BBC-small selection criteria as a function of $\bar{\eta}$ in three ranges of ξ. The fraction of such events is shown in the bottom panels.

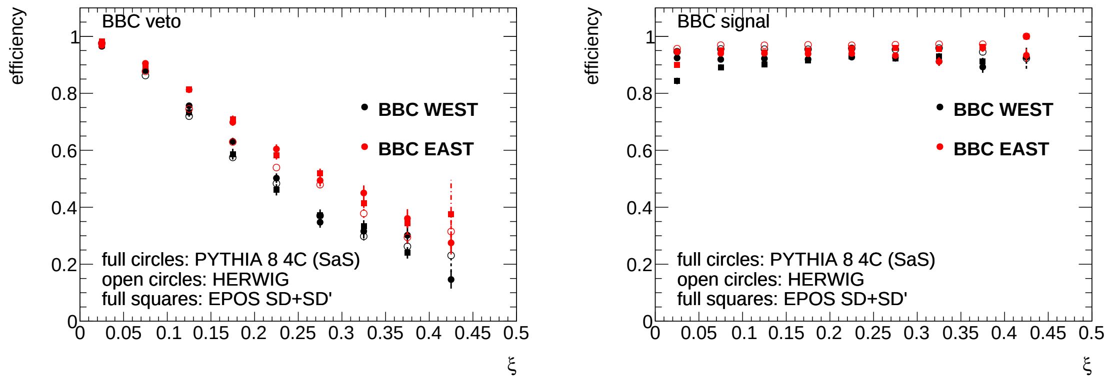

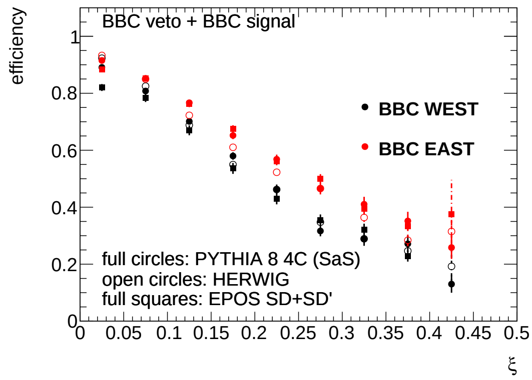

Figure 5.11: PYTHIA 8 4C (SaS), HERWIG and EPOS SD+SD′ predictions on (top left) veto, (top right) signal and (bottom) joined BBC-small efficiencies as a function of ξ calculated separately for BBCs on EAST and WEST side of the IP.

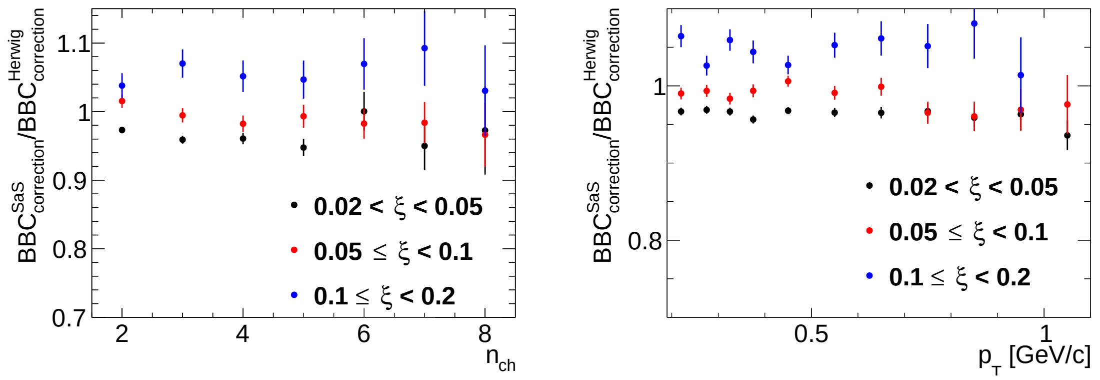

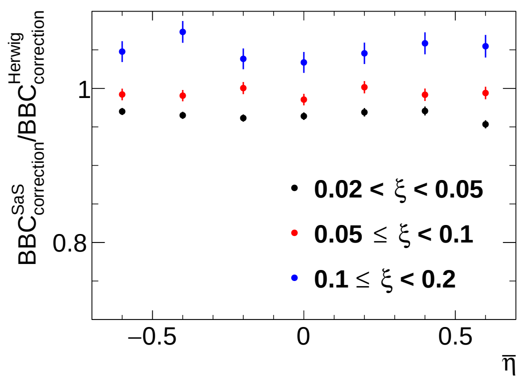

Figure 5.12: PYTHIA 8 4C (SaS) prediction on BBC efficiency divided by the HERWIG prediction as a function of (top left) n_{ch}, (top right) p_{T} and (bottom) $\bar{\eta}$ in three ranges of ξ

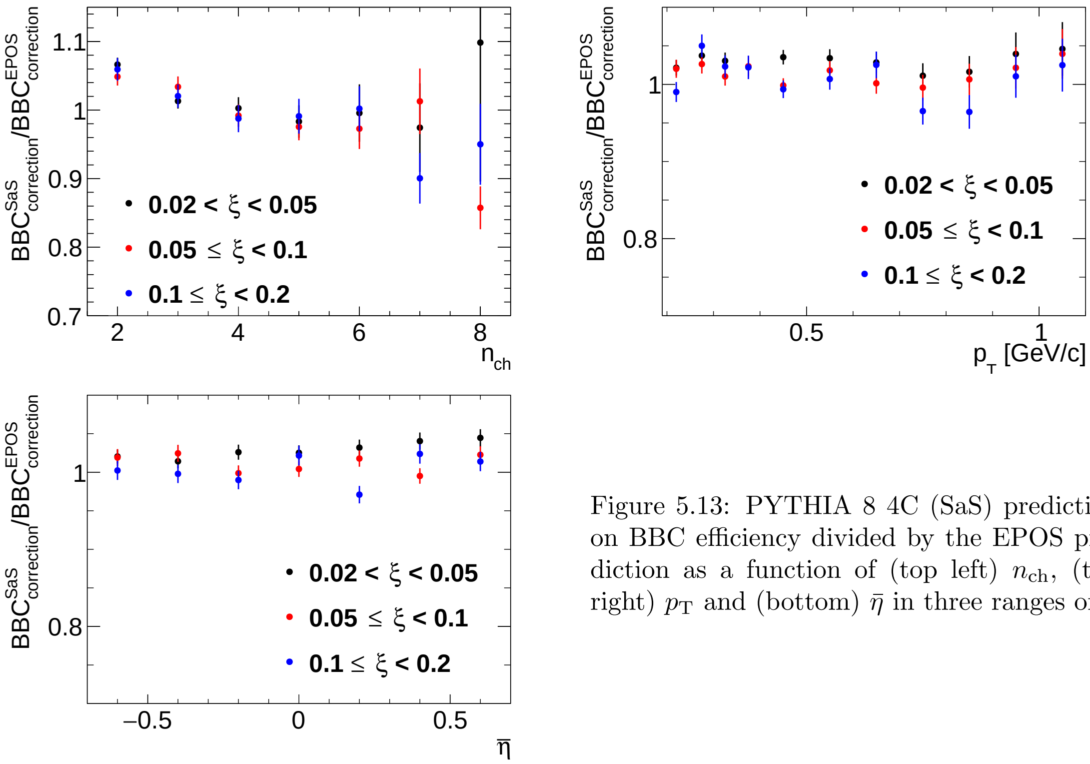

Figure 5.13: PYTHIA 8 4C (SaS) prediction on BBC efficiency divided by the EPOS prediction as a function of (top left) $n_{\rm ch}$, (top right) $p_{\rm T}$ and (bottom) $\bar{\eta}$ in three ranges of ξ

6. Migrations into and out of the Fiducial Region

In this section the corrections due to the migrations of tracks and forward-scattered protons into and out of the fiducial region are described.

6.1 Migrations of Tracks into and out of the Fiducial Region

The procedure, described in this section, accounts for migrations of tracks into and out of the fiducial region, which originate from TPC resolution effects. The correction factor for such tracks, $f_{\mathrm{okr}}(p_T, \eta)$ is defined as follows:

$$f_{\mathrm{okr}}(p_{\mathrm{T}}, \eta) = \frac{1 - f^{-}_{\mathrm{okr}}(p_{\mathrm{T}}, \eta)}{1 - f^{+}_{okr}(p_{\mathrm{T}}, \eta)} \tag{6.1}$$

where $f^{-}_{\mathrm{okr}}(p_{\mathrm{T}}, \eta)$ is the fraction of reconstructed tracks for which the corresponding primary particle is outside of the kinematic range of the measurement and $f^{+}_{\mathrm{okr}}(p_{\mathrm{T}}, \eta)$ is the fraction of primary particles for which the corresponding reconstructed track is outside of the kinematic range of the measurement.

The resulting residual migrations, shown in Fig. 6.1, were estimated using PYTHIA 8 SD embedding MC. The main effect was observed at $|\eta| \sim 0.7$, where about $2 - 6\%$ reconstructed tracks were associated to primary particle outside the fiducial region. However, above contributions to the correction factor, $f_{\mathrm{okr}}(p_T, \eta)$, cancel each other and the resulting factor is about 2% at $|\eta| \sim 0.7$.

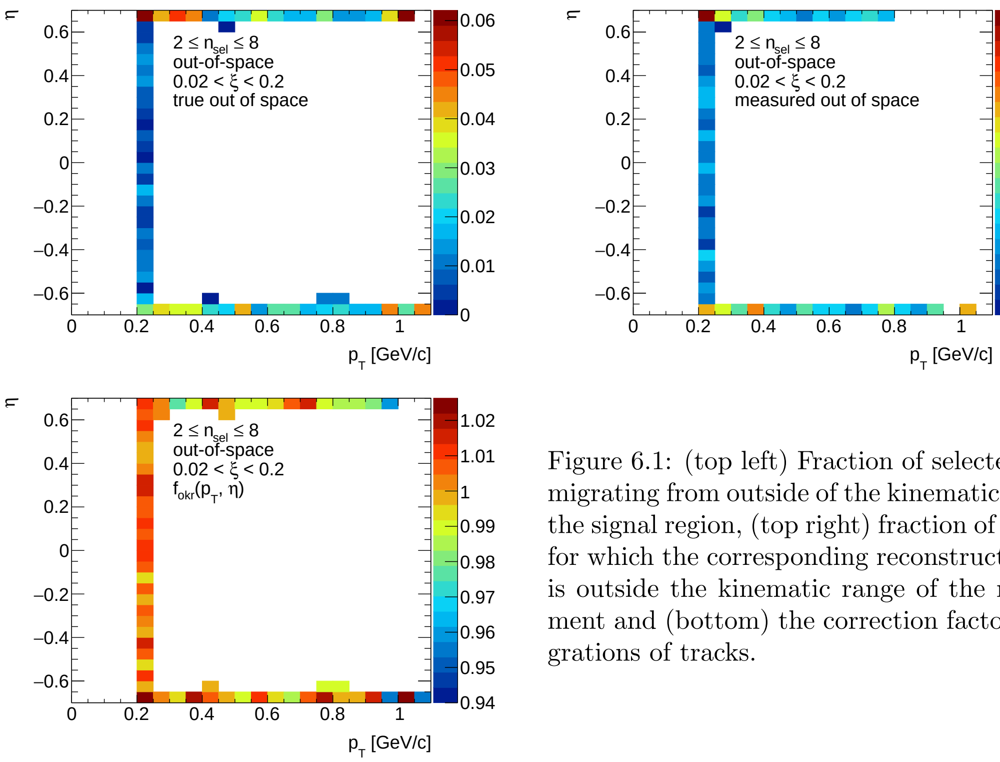

Figure 6.1: (top left) Fraction of selected tracks migrating from outside of the kinematic range to the signal region, (top right) fraction of particles for which the corresponding reconstructed track is outside the kinematic range of the measurement and (bottom) the correction factor for migrations of tracks.

6.2 Migrations in ξ

The analysis was performed in three ranges of ξ. Thus, there are migrations into and out of these ξ regions. They mainly originate from the resolution of ξ reconstructed from RP tracks. Figure 6.2 shows the resolution of ξ as a function of the true-level ξ (denoted as ξ_{true}) with fitted zeroth order polynomial. The resolution of ξ is fairly constant and equals to about 0.3%.

The corrections due to migrations into and out of ξ regions was defined as:

$$f_\xi = \frac{1 - f_\xi^-}{1 - f_\xi^+} \tag{6.2}$$

where f_ξ^- is the fraction of events for which the corresponding true-level, ξ_{true}, is outside of the ξ region and f_ξ^+ is the fraction of events for which the corresponding reconstructed, ξ_{reco}, is outside of the ξ region.

The f_ξ was calculated for each measured variable separately. Figures 6.3 to 6.5 show the fraction of events f_ξ^- and f_ξ^+ as a function of n_{ch}, p_{T} and $\bar{\eta}$. The lower panel in each figure shows the corresponding correction factor f_ξ. The largest differences between migrations into and out of the ξ regions were observed at $0.02 < \xi < 0.05$, where they are of the order of $2 - 4\%$. In the other ξ regions, the difference between f_ξ^- and f_ξ^+ is smaller than 1%.

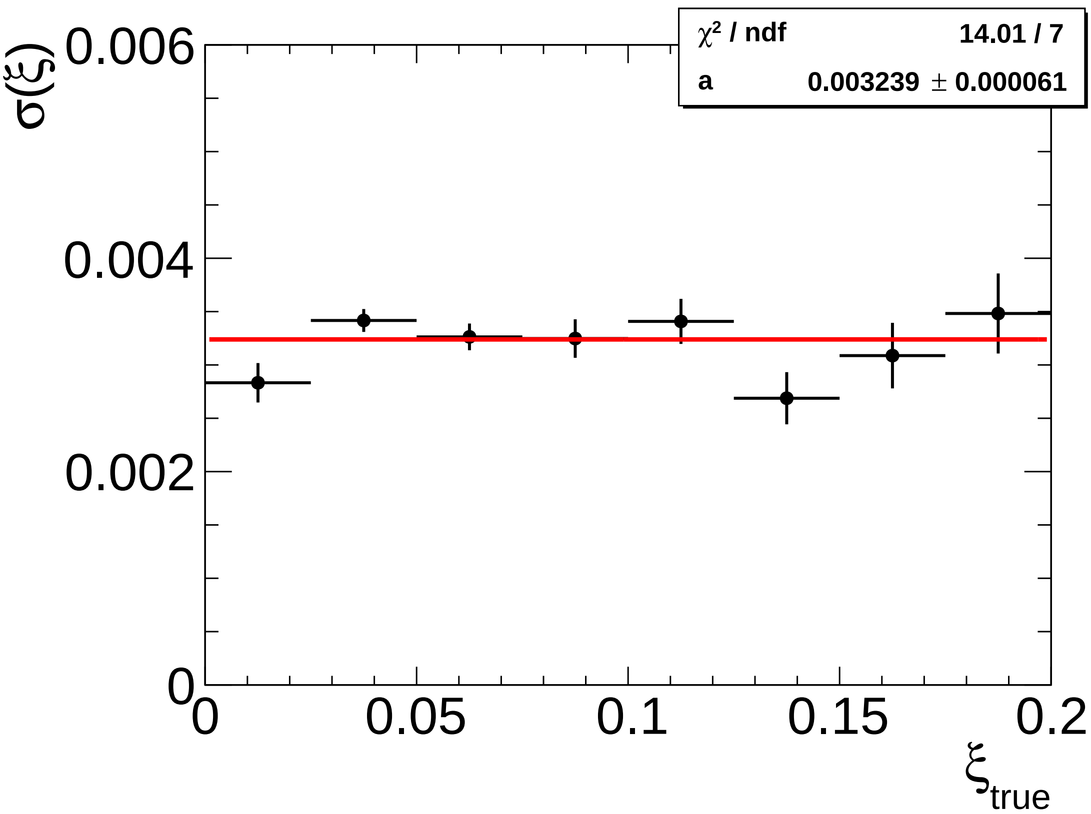

Figure 6.2: The resolution of ξ as a function of ξ_{true}. The zeroth order polynomial, shown as red line, was fitted.

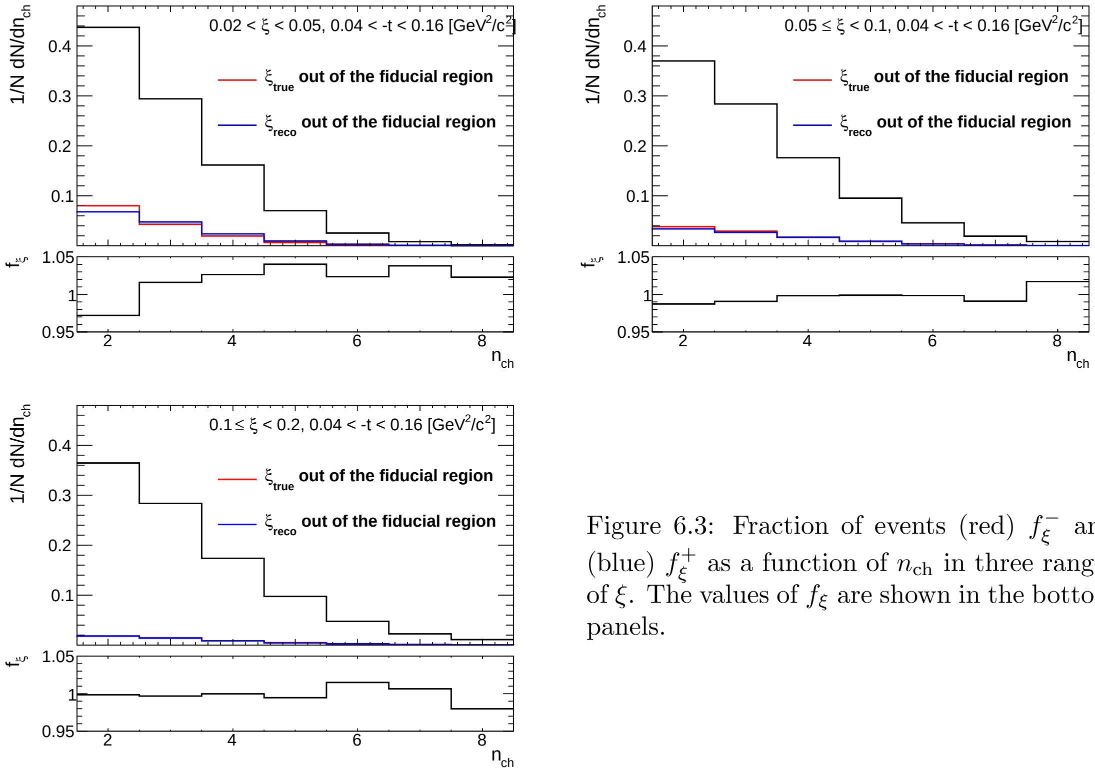

Figure 6.3: Fraction of events (red) f_ξ^- and (blue) f_ξ^+ as a function of $n_{\rm ch}$ in three ranges of ξ. The values of f_ξ are shown in the bottom panels.

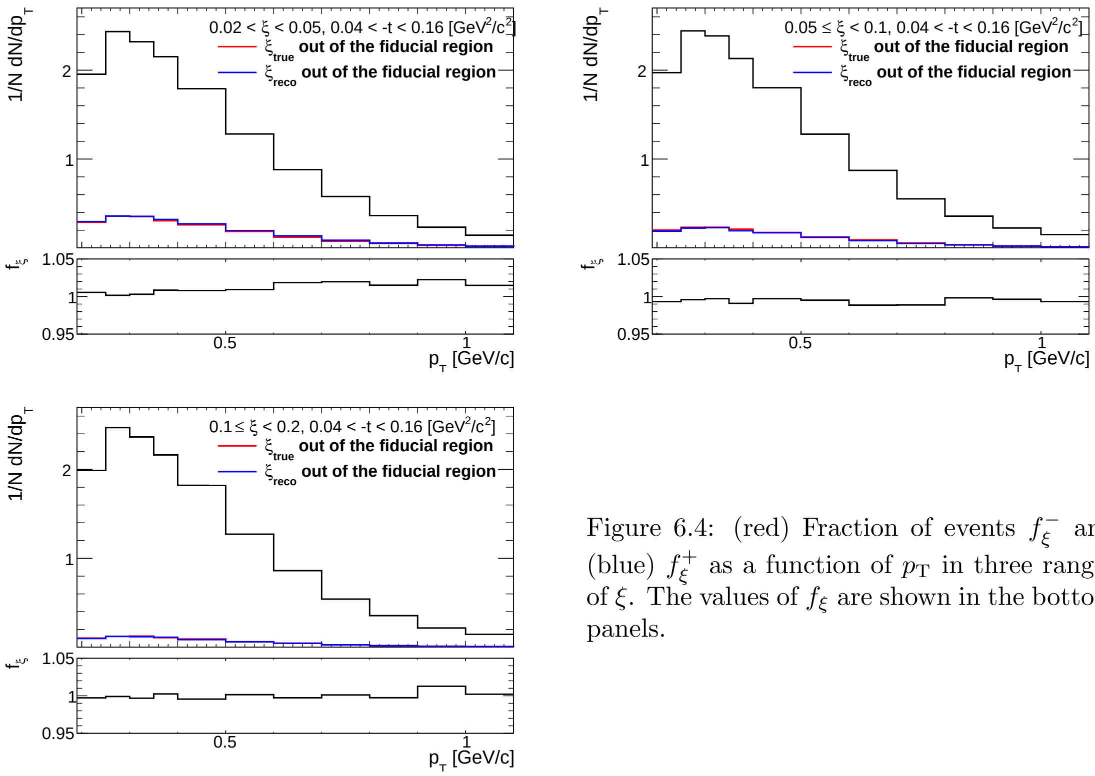

Figure 6.4: (red) Fraction of events f_ξ^- and (blue) f_ξ^+ as a function of $p_{\rm T}$ in three ranges of ξ. The values of f_ξ are shown in the bottom panels.

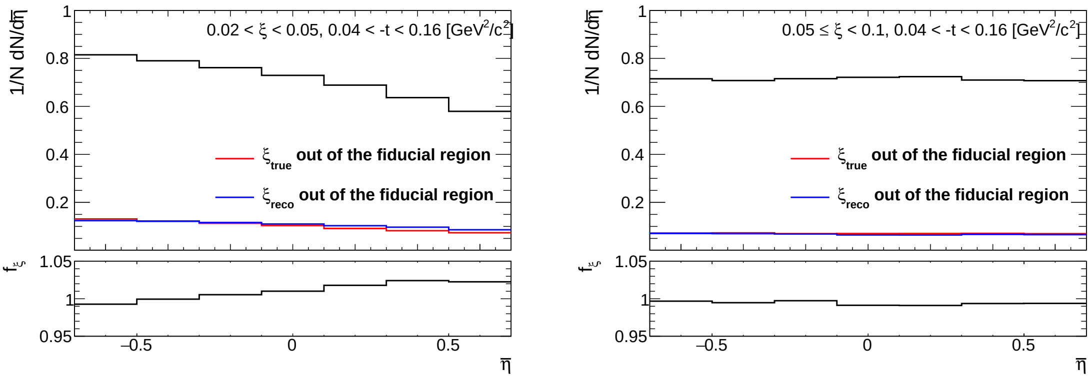

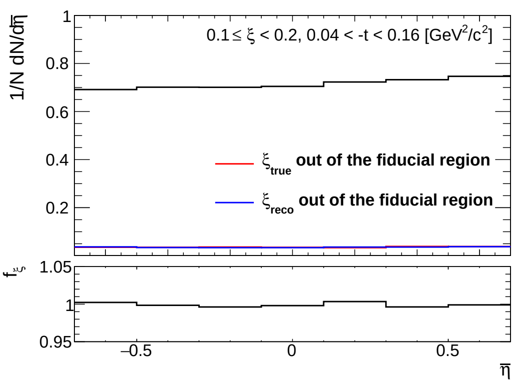

Figure 6.5: (red) Fraction of events f_ξ^- and (blue) f_ξ^+ as a function of $\bar{\eta}$ in three ranges of ξ. The values of f_ξ are shown in the bottom panels.

7. Event Corrections and Unfolding Procedure

After subtraction of accidental, DD, CD and ND backgrounds (as described in Sec. 4 and 4.2), the data was corrected for detector inefficiencies to obtain the distributions of charged particles and particle to antiparticle (pion, kaon, proton and their antiparticle) multiplicity ratios. These corrections include:

- event-by-event weights due to vertex reconstruction efficiency:

$$w_{\mathrm{ev}}^{\mathrm{vrt}}\left(n_{\mathrm{vrt}}^{\mathrm{global}}, |\Delta z_0|\right) = \frac{1}{\epsilon_{\mathrm{vrt}}\left(n_{\mathrm{vrt}}^{\mathrm{global}}, |\Delta z_0|\right)} \cdot \frac{1}{1 - f_{\mathrm{vrt}}^{\mathrm{veto}}\left(n_{\mathrm{vrt}}^{\mathrm{global}}, |\Delta z_0|\right)} \tag{7.1}$$

  where the $|\Delta z_0|$ dependence is only applicable for events with $n_{\mathrm{vrt}}^{\mathrm{global}} = 2$ as described in Sec. 5.1.

- track-by-track weights due to track reconstruction efficiency, track backgrounds, migrations of tracks into and out of the fiducial region:

$$w_{\mathrm{trk}}\left(p_{\mathrm{T}}, \eta, V_z\right) = \frac{1 - f_{\mathrm{bkg}}\left(p_{\mathrm{T}}, \eta\right) - f_{\mathrm{fake}}\left(p_{\mathrm{T}}, \eta\right)}{\epsilon_{\mathrm{TPC}}\left(p_{\mathrm{T}}, \eta, V_z\right)\epsilon_{\mathrm{TOF}}\left(p_{\mathrm{T}}, \eta, V_z\right)} f_{\mathrm{okr}}\left(p_{\mathrm{T}}, \eta\right) \tag{7.2}$$

  where: $\epsilon_{\mathrm{TPC}}\left(p_{\mathrm{T}}, \eta, V_z\right)$ is TPC track reconstruction efficiency [1], $\epsilon_{\mathrm{TOF}}\left(p_{\mathrm{T}}, \eta, V_z\right)$ is TOF matching efficiency [1], $f_{\mathrm{okr}}\left(p_{\mathrm{T}}, \eta\right)$ is a factor accounting for migrations of tracks into and out of the fiducial region, $f_{\mathrm{bkg}}\left(p_{\mathrm{T}}, \eta\right)$ is a fraction of background tracks, and $f_{\mathrm{fake}}\left(p_{\mathrm{T}}, \eta\right)$ is a fraction of fake tracks. These corrections were not applied for n_{ch} measurements since they were taken into account in the unfolding procedure.

- event-by-event (for n_{ch} distribution) or track-by-track (for p_{T}, $\bar{\eta}$ distributions) weights, f_{ξ}, due to migrations of events between three ξ regions.

Additionally, the obtained distributions were corrected for BBC-small efficiency, ϵ_{BBC}, using the following weight, which was calculated for each true-level quantity (n_{ch}, p_{T}, $\bar{\eta}$) in three ranges of ξ separately:

$$w_{\mathrm{BBC}} = \frac{1}{\epsilon_{\mathrm{BBC}}} \tag{7.3}$$

In the following sections, the correction procedure for each of the measured distributions is presented separately.

7.1 Correction to dN/dn$_{\mathrm{sel}}$

In order to express the multiplicity distribution in terms of the number of charged particles, n_{ch}, instead of the number of selected tracks, n_{sel}, the following procedure based on the Bayesian unfolding [14, 15] was used. First, the n_{sel} distribution was corrected for vertex reconstruction effects by applying event-by-event weights, $w_{\mathrm{ev}}^{\mathrm{vrt}}(n_{\mathrm{vrt}}^{\mathrm{global}}, |\Delta z_0|)$. The number of events in which n_{ch} are produced, $N_{\mathrm{ev}}(n_{\mathrm{ch}})$, can be associated with the number of events in which n_{sel} are reconstructed, $N_{\mathrm{ev}}(n_{\mathrm{sel}})$. Since there are several possible n_{sel} observed in n_{ch} event, $N_{\mathrm{ev}}(n_{\mathrm{ch}})$ is given by:

$$\begin{aligned} N_{\mathrm{ev}}(n_{\mathrm{ch}}) &= \sum_{n_{\mathrm{sel}}=0} P(n_{\mathrm{ch}}|n_{\mathrm{sel}}) \cdot N_{\mathrm{ev}}(n_{\mathrm{sel}}) \\ &= \frac{1}{\epsilon_m(n_{\mathrm{ch}})\epsilon_r(n_{\mathrm{ch}})} \sum_{n_{\mathrm{sel}}=2}^{8} P(n_{\mathrm{ch}}|n_{\mathrm{sel}}) \cdot N_{\mathrm{ev}}(n_{\mathrm{sel}}) \end{aligned} \tag{7.4}$$

where:

$P(n_{\mathrm{ch}}|n_{\mathrm{sel}})$ is the conditional probability of having n_{ch} charged particles in an event in which n_{sel} tracks were found,

$\epsilon_m(n_{\mathrm{ch}})$ is a factor, which recovers events that are lost due to TPC track reconstruction and TOF matching inefficiencies, i.e. those with $n_{\mathrm{ch}} \geq 2$ but $n_{\mathrm{sel}} < 2$,

$\epsilon_r(n_{\mathrm{ch}})$ is a factor, which recovers events which are lost due to fake tracks, i.e. those with $n_{\mathrm{ch}} \leq 8$ but $n_{\mathrm{sel}} > 8$. It was checked that this effect is negligible (smaller than 1‰) and can be omitted.

Figure 7.1 shows $\epsilon_m(n_{\mathrm{ch}})$ in three ranges of ξ. It was derived from PYTHIA 8 embedding MC and varies from about 25% for $n_{\mathrm{ch}} = 2$ to 95% for $n_{\mathrm{ch}} = 8$. Since there are additional data-driven corrections to TPC and TOF efficiencies, MC simulations were modified by randomly removing or adding tracks. This was done in accordance with differences in the efficiencies between data and MC. Figure 7.2 shows $\epsilon_m(n_{\mathrm{ch}})$ calculated in three ranges of ξ using no-pile-up PYTHIA 8 and EPOS SD+SD′. The differences between these two models, which are up to 12% for $n_{\mathrm{ch}} = 2$ and $0.02 < \xi < 0.05$, were symmetrized and taken as a systematic uncertainty.
The probability $P(n_{\mathrm{ch}}|n_{\mathrm{sel}})$ can be derived using Bayes' theorem, which can be stated mathematically in terms of charged particle and charged track multiplicities as:

$$P\left(n_{\mathrm{sel}}|n_{\mathrm{ch}}\right) \cdot P\left(n_{\mathrm{ch}}\right) = P\left(n_{\mathrm{ch}}|n_{\mathrm{sel}}\right) \cdot P\left(n_{\mathrm{sel}}\right) \tag{7.5}$$

where: $P(n_{\mathrm{sel}})$ and $P(n_{\mathrm{ch}})$ are probabilities of observing n_{sel} and n_{ch} respectively, $P(n_{\mathrm{ch}}|n_{\mathrm{sel}})$ and $P(n_{\mathrm{sel}}|n_{\mathrm{ch}})$ are conditional probabilities.
In order to improve the estimate of $P(n_{\mathrm{ch}}|n_{\mathrm{sel}})$, the unfolding is done iteratively:

- In the first iteration, it is assumed that:

$$P(n_{\mathrm{ch}}|n_{\mathrm{sel}}) = P = P^{\mathrm{MC}}(n_{\mathrm{sel}}|n_{\mathrm{ch}}) \frac{P^{\mathrm{MC}}(n_{\mathrm{ch}})}{P^{\mathrm{MC}}(n_{\mathrm{sel}})} \tag{7.6}$$

$$N_{\mathrm{ev}}(n_{\mathrm{ch}}) = \frac{1}{\epsilon_m(n_{\mathrm{ch}})} \sum_{n_{\mathrm{sel}}=2}^{8} N_{\mathrm{ev}}(n_{\mathrm{sel}}) \cdot P \tag{7.7}$$

  where $P^{\mathrm{MC}}(n_{\mathrm{sel}}|n_{\mathrm{ch}})$, $P^{\mathrm{MC}}(n_{\mathrm{ch}})$ and $P^{\mathrm{MC}}(n_{\mathrm{sel}})$ are obtained from MC. $P^{\mathrm{MC}}(n_{\mathrm{sel}}|n_{\mathrm{ch}})$ is the same for each iteration.

- In the $(i+1)$th iteration we have:

$$P^{i+1} = P^{\mathrm{MC}}(n_{\mathrm{sel}}|n_{\mathrm{ch}}) \frac{N^{i}_{\mathrm{ev}}(n_{\mathrm{ch}})}{N_{\mathrm{ev}}(n_{\mathrm{sel}})} \tag{7.8}$$

$$N^{i+1}_{\mathrm{ev}}(n_{\mathrm{ch}}) = \frac{1}{\epsilon_m(n_{\mathrm{ch}})} \sum_{n_{\mathrm{sel}}=2}^{8} N_{\mathrm{ev}}(n_{\mathrm{sel}}) \cdot P^{i+1} \tag{7.9}$$

  where $N^{i}_{\mathrm{ev}}(n_{\mathrm{ch}})$ is calculated in the previous iteration, and $N_{\mathrm{ev}}(n_{\mathrm{sel}})$ is taken from data.

The unfolding matrices $P(n_{\mathrm{ch}}|n_{\mathrm{sel}})$ for each ξ region, shown in Fig. 7.3, were obtained from PYTHIA 8 embedding MC and used in all iterations of the above procedure. Similarly to $\epsilon_m(n_{\mathrm{ch}})$, the matrices were modified by randomly removing or adding tracks in order to take into account additional data-driven corrections to TPC and TOF efficiencies. In order to increase statistical precision of the unfolding matrices, all simulated events were used, i.e. also those with additional fake vertices (with n_{sel} defined as a number of primary tracks associated with the best vertex). The systematic uncertainty related to limited statistics in PYTHIA 8 was estimated by performing 50 pseudo-experiments, in which the unfolding matrices were smeared according to their statistical

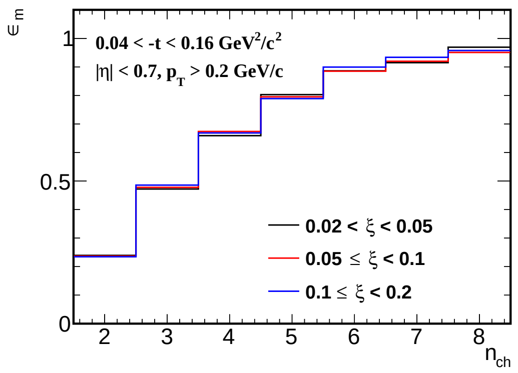

Figure 7.1: $\epsilon_m(n_{\rm ch})$ calculated separately in three ranges of ξ using PYTHIA 8 embedding MC.

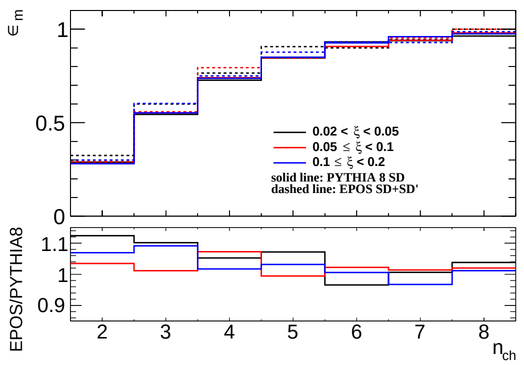

Figure 7.2: Comparison of $\epsilon_m(n_{\rm ch})$ calculated separately in three ranges of ξ using PYTHIA 8 SD and EPOS SD+SD$'$ no-pile-up MCs. The ratios of EPOS to PYTHIA 8 predictions are shown in the bottom panel.

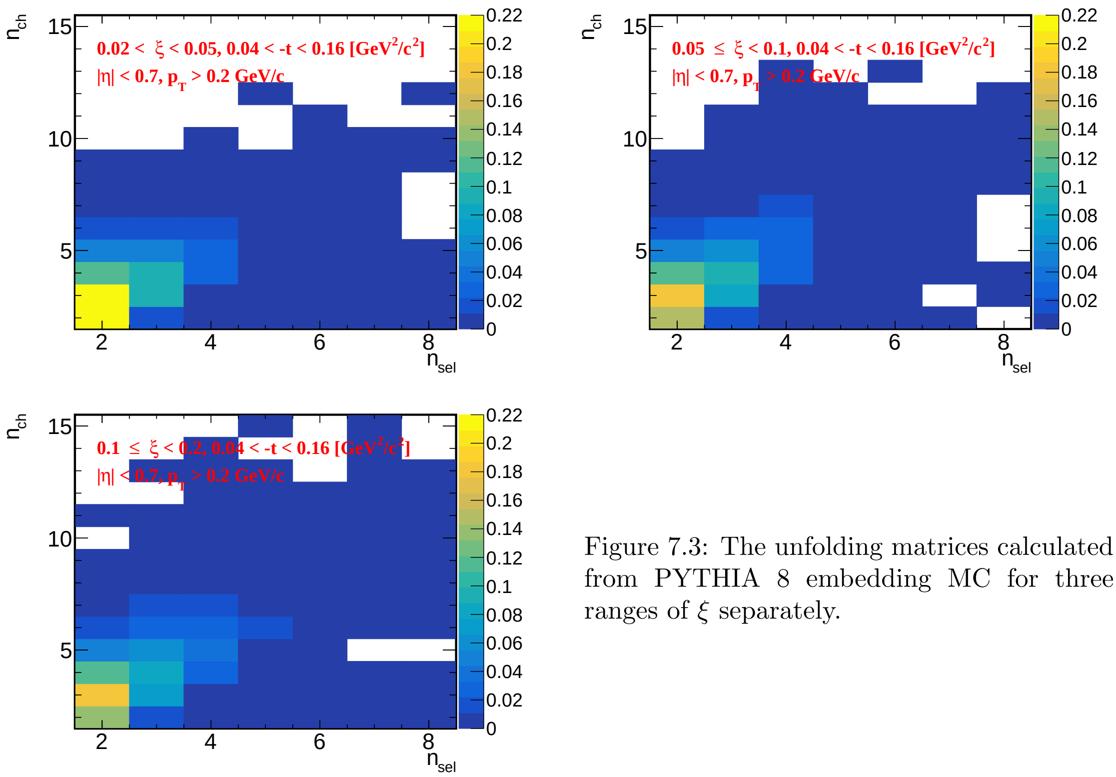

Figure 7.3: The unfolding matrices calculated from PYTHIA 8 embedding MC for three ranges of ξ separately.

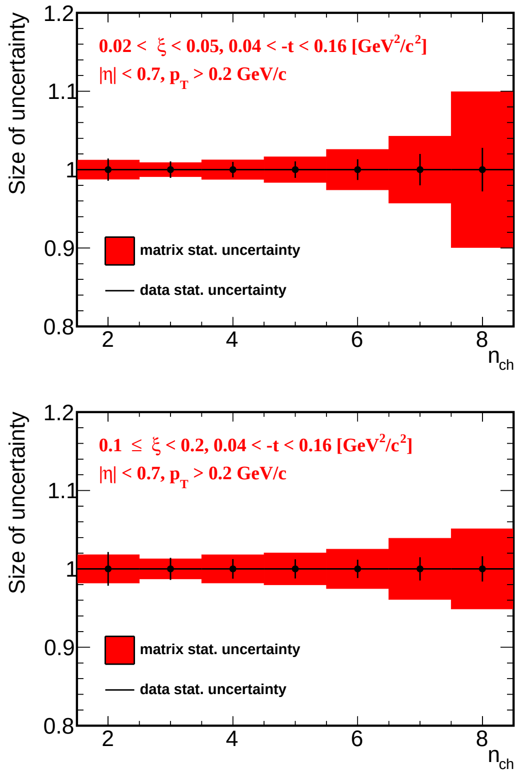

Figure 7.4: Comparison of uncertainties related to data and PYTHIA 8 statistics for the charged particle multiplicity in three ξ regions. The error bars represent uncertainty due to data statistics, while the red band shows uncertainty of the unfolding matrices.

uncertainties. It affects mainly large charged-particle multiplicities, where it is about $8-10\%$ (as shown in Fig. 7.4), and is smaller or at the same level as other components contributing to the total systematic uncertainty.

The distribution dN/dn_{ch} obtained after the unfolding procedure was corrected for BBC-small efficiency, through $w_{\mathrm{BBC}}(n_{\mathrm{ch}})$ weights, and migrations of events between ξ ranges, through $f_{\xi}(n_{\mathrm{ch}})$ weights. Since the unfolding matrices contain track reconstruction efficiencies, non-primary track backgrounds, migrations of tracks into and out of the fiducial region, the weight $w_{\mathrm{trk}}\,(p_{\mathrm{T}}, \eta, V_z)$ was not used.

Finally, the dN/dn_{ch} distribution was normalized to the total number of events, $N_{\mathrm{ev}} = N$, which was calculated as the integral of the unfolded distribution.

7.2 Correction to Transverse Momentum and Pseudorapidity Distributions

First the accidental and non-SD backgrounds were subtracted from the p_{T} and $\bar{\eta}$ distributions. Next, each event was corrected for vertex reconstruction efficiency by applying $w_{\mathrm{ev}}^{\mathrm{vrt}}(n_{\mathrm{vrt}}^{\mathrm{global}}, |\Delta z_0|)$ weights. Then, the tracks were corrected for the track reconstruction efficiency, non-primary track background contribution, track and ξ migrations, BBC-small efficiency (the product of $w_{\mathrm{trk}}(p_{\mathrm{T}}, \eta, V_z)$, f_{ξ} and w_{BBC} weights was applied, f_{ξ} and w_{BBC} were calculated as a function of true-level p_{T} and $\bar{\eta}$ separately).

In order to obtain charged-particle densities, the p_{T} and $\bar{\eta}$ distributions were normalized to unity and scaled by the average charged particle multiplicity in an event $\langle n_{\mathrm{ch}}\rangle$. The latter was calculated from the corrected charged particle multiplicity distribution dN/dn_{ch} (Sec. 7.1). The above procedure was done to correct the data also for events that are lost due to $n_{\mathrm{sel}} < 2$ but $n_{\mathrm{ch}} \geq 2$ since such correction was not included in any event-by-event and track-by-track weights. There was an assumption that p_{T} and η distributions are the same for lost and measured events, but it was validated by the closure tests (Sec. 7.3). The mean p_{T} and $\bar{\eta}$ in an event, $\langle p_{\mathrm{T}} \rangle$ and $\langle \bar{\eta} \rangle$, were obtained from the measured distributions.

7.3 Closure Tests

In order to validate the correction procedures, closure tests were performed, i.e. full correction procedure was applied to the MC detector-level distributions and the results were directly compared to the true-level distributions. Figure 7.5 shows closure tests of multiplicity, transverse momentum and pseudorapidity distributions for three ranges of ξ, separately. PYTHIA 8 SD embedding MC was used as an input. In order to compare corrected and true-level distributions, the statistical uncertainties of the true-level distributions were assumed to be 0. The difference between true-level and corrected distributions was taken as a systematic uncertainties.

7.4 EAST-WEST asymmetry

Another kind of consistency check can be performed by comparing the results obtained by tagging forward-scattered protons in different detectors. Therefore, each distribution was measured separately for events in which forward-scattered proton is on one and the other side of the IP (east-west). Figure 7.6 shows the tests of multiplicity, transverse momentum and pseudorapidity distributions for three ranges of ξ, separately. Both statistical uncertainty components, due to input data and due to unfolding matrix, are added in quadrature for n_{ch} distributions. The largest difference is observed for charged-particle multiplicity distributions, where it varies up to 20% for $n_{\mathrm{ch}} = 8$ and $0.02 < \xi < 0.1$. For the rest multiplicities and ξ ranges, the differences are smaller ($< 10\%$). In case of p_{T} and $\bar{\eta}$ distributions, a level of these disagreements is below 5%.

The deviations between the distributions for events with forward-scattered proton on east and west side of the IP were fitted with a constant (Fig. 7.6). The quality of the fit shows that the disagreements are compatible with statistical fluctuations (χ^2/ndf close to 1) for multiplicity and transverse momentum distributions. For pseudorapidity, the χ^2/ndf is significantly larger than 1.

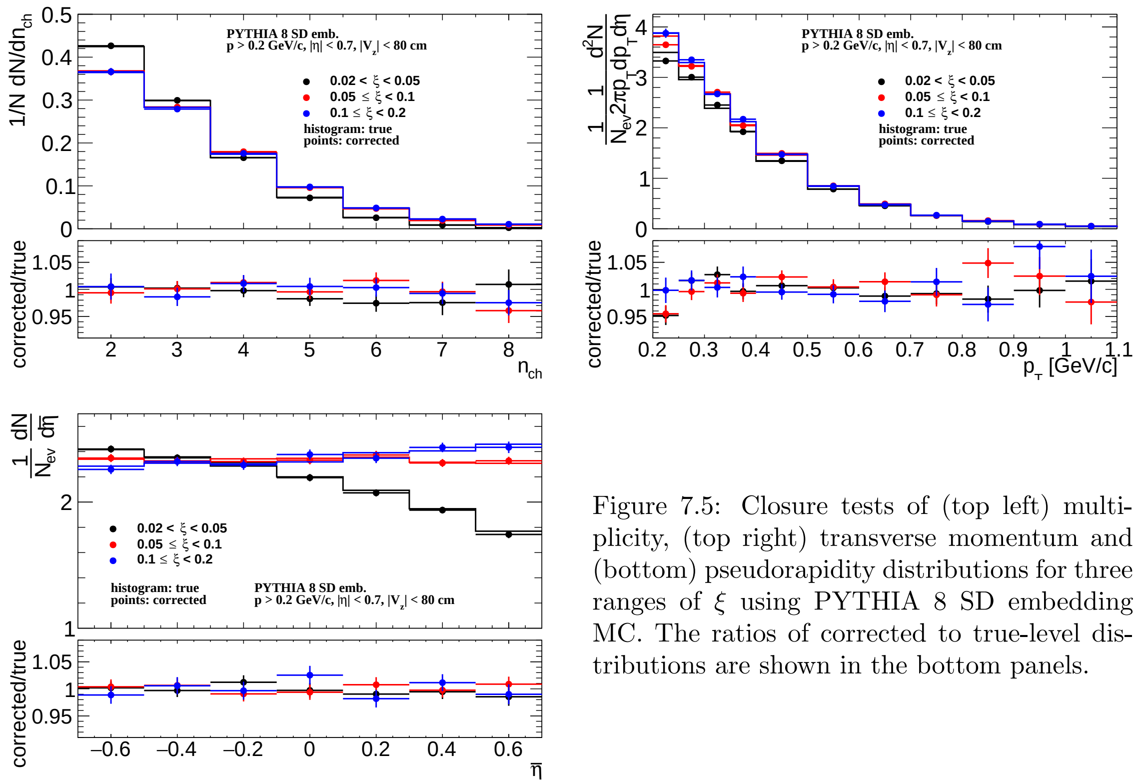

Figure 7.5: Closure tests of (top left) multiplicity, (top right) transverse momentum and (bottom) pseudorapidity distributions for three ranges of ξ using PYTHIA 8 SD embedding MC. The ratios of corrected to true-level distributions are shown in the bottom panels.

Therefore, half of the differences between east and west distributions were used to be systematic uncertainty for $\bar{\eta}$ distributions.

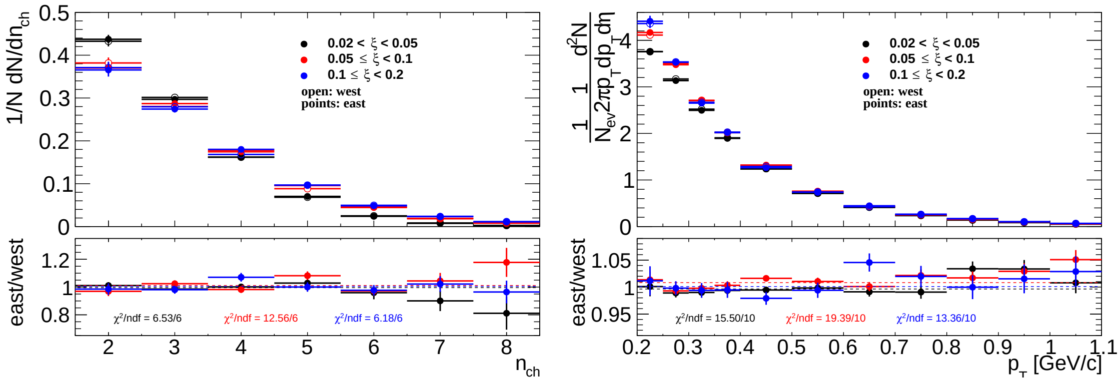

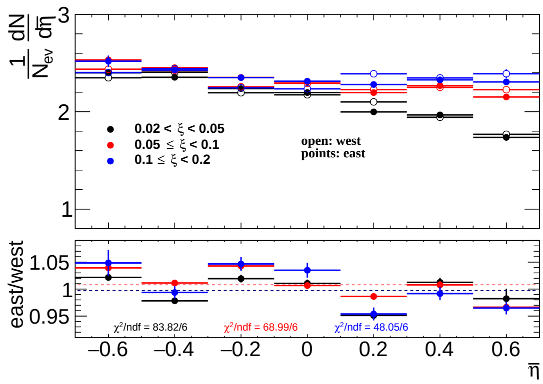

Figure 7.6: (top left) Primary charged-particle multiplicity, (top right) transverse momentum and (bottom) psuedorapidity distributions for three ranges of ξ. Particle densities are presented separately for events with forward scattered protons on (open circles) WEST and (full circles) EAST side of the IP. Both statistical uncertainty components, due to input data and due to unfolding matrix, are added in quadrature for $n_{\rm ch}$ distributions.

7.5 Particle Identification

Specific ionization energy loss, the dE/dx, is a function of the magnitude of a particle momentum. In this section the particle identification with help of dE/dx is described. Due to a low particle multiplicity and lack of signal in VPDs on the outgoing proton side (presence of the rapidity gap) in SD events, the time of collision is not defined precisely enough, therefore, the particle identification by the TOF is not possible and the analysis was limited to identification only by dE/dx.

The ionization energy loss of charged particles in material is given by the Bethe-Bloch formula and for the STAR TPC by the more precise Bichsel formula [16]. The particle type can be determined by comparison of particle's dE/dx with the Bethe-Bloch (Bichsel) expectations. Figure 7.7 shows the dE/dx versus rigidity $q \times p$ for particles in $|\eta| < 0.7$. Particles are well separated at low $|q \times p|$, whereas at higher $|q \times p|$ the dE/dx of different particle species starts to overlap: $e^{\pm}$ and $K^{\pm}$ merge at ~ 0.4 GeV/c, $K^{\pm}$ and $\pi^{\pm}$ merge at ~ 0.65 GeV/c, and $p(\bar{p})$ and $\pi^{\pm}$ merge at ~ 1 GeV/c. Since the dE/dx distribution for a given particle type is not Gaussian, the following variable for each particle type was defined:

$$n\sigma^{i}_{dE/dx} = \ln\left(\frac{dE/dx}{(dE/dx)^{\rm BB}_{i}}\right)/\sigma \tag{7.10}$$

where $(dE/dx)^{\rm BB}_{i}$ is the Bethe-Bloch (Bichsel) expectation of dE/dx for the given particle type i ($i = \pi, K, p$), σ - the relative dE/dx resolution. The expected value of $n\sigma^{i}_{dE/dx}$ for the particle under consideration is 0 and the width equals to 1. The sample $n\sigma^{i}_{dE/dx}$ distribution for $\pi^{\pm}$, $K^{\pm}$ and $p(\bar{p})$ in one ξ range, $0.02 < \xi < 0.05$, is shown in Fig. 7.8.

Figure 7.9 shows the $n\sigma^{\pi^\pm}_{dE/dx}$,$n\sigma^{K^\pm}_{dE/dx}$ and $n\sigma^{p(\bar{p})}_{dE/dx}$ distributions for $0.6 < p_\mathrm{T} < 0.65$ GeV/c in the ξ range, $0.02 < \xi < 0.05$, each corrected for the energy loss (mass of i-particle was assumed) [1] and vertexing (other p_T bins are shown in Appendix B). To extract the particle yield for a given particle type, a multi-Gaussian fit is applied to the $n\sigma^{i}_{dE/dx}$ distribution in each p_T bin and ξ range. The parameters of the multi-Gaussian fit are the centroids μ_{i^-/i^+}, widths σ_{i^-/i^+}, sums and ratios of yields C_{i^-/i^+}, r_{i^-/i^+} for negative i^- and positive i^+ particles ($\pi^\pm$, $e^\pm$, $K^\pm$, p and $\bar{p}$). The positive and negative particle $n\sigma^{i}_{dE/dx}$-distributions are fitted simultaneously, where the centroids and widths are kept the same for particle and antiparticle. In some p_T regions, the fit does not converge, because different particle species are not well separated there. Therefore, multiple steps of the fitting procedure are performed to reduce the number of free parameters in the final fit and ensure its stability. Almost all centroids and widths are constrained by a function with free parameters p_k, where $k \in \mathbb{N}$. The function is chosen to describe the data as best as possible. Since dE/dx is a function of the particle's momentum and its shape should be independent of the process under study, the values of p_k are obtained only for events with $0.02 < \xi < 0.05$ and kept the same for other ξ ranges. The electron contributions are fitted only at $p_\mathrm{T} < 0.4$ GeV/c, separately for each particle species and ξ range. For higher p_T ranges, they are estimated from PYTHIA 8 embedding MC, and scaled according to the ratio of PYTHIA 8 predictions and contributions fitted in the $0.35 < p_\mathrm{T} < 0.4$ GeV/c bin. The procedure slightly differs for different particle types. In each step, the multi-Gaussian fit is performed first, then the widths and centroids are fitted in p_T ranges in which the fit applied to $n\sigma^{i}_{dE/dx}$ converges. Later, the widths and centroids are extrapolated to other p_T ranges, in which particle species are not well separated:

1. $\pi^\pm$:
   - Step 1 (Fig. 7.10):
     - Analyze data with $0.2 < p_\mathrm{T} < 0.65$ GeV/c
     - Fit μ_{π^-/π^+} and σ_{π^-/π^+} as a function of p_T with a polynomial $p_0 p_\mathrm{T}^3 + p_1 p_\mathrm{T}^2 + p_2 p_\mathrm{T} + p_3$
     - Fit μ_{K^-/K^+} as a function of p_T with $p_0 \exp(p_1 p_\mathrm{T}) + p_2$
     - Fit μ_{e^-/e^+} as a function of p_T with $p_0 \exp\left[-(p_1 p_\mathrm{T})^{p_2}\right]$
     - Fit σ_{K^-/K^+} as a function of p_T, for $0.3 < p_\mathrm{T} < 0.5$ GeV/c, with constant p_0
     - Fit $\mu_{\bar{p}/p}$ and $\sigma_{\bar{p}/p}$ as a function of p_T with $p_0 \exp(p_1 p_\mathrm{T})$
   - Step 2:

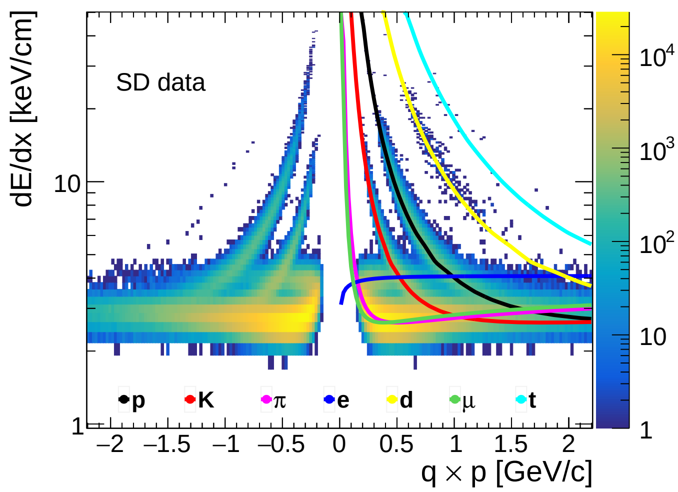

Figure 7.7: Specific ionization energy loss dE/dx as a function of rigidity $q \times p$ for particles in $|\eta| < 0.7$. The Bichsel predictions for each particle species are also shown.

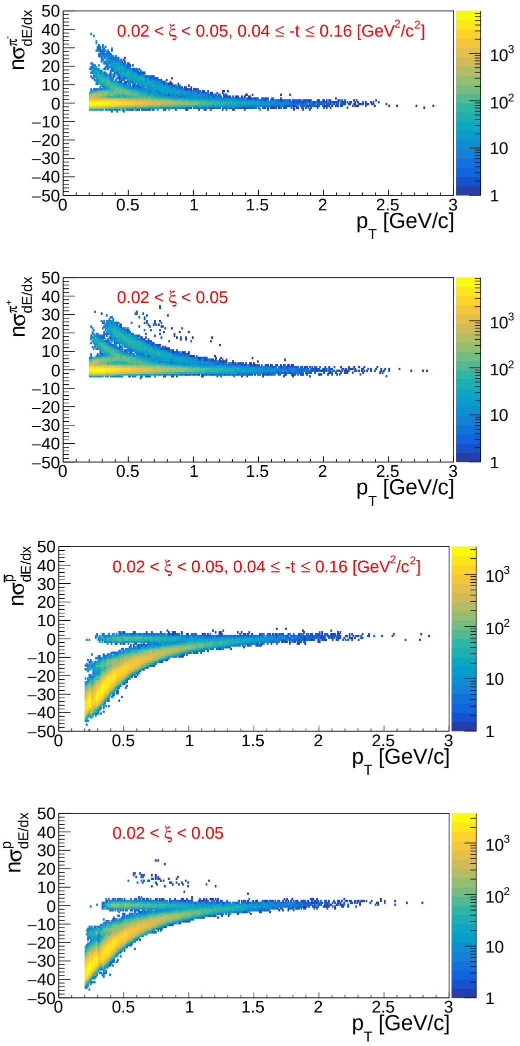

Figure 7.8: The $n\sigma^{i}_{dE/dx}$ variable for particle $i^{\pm}$ versus p_{T}. Particles are restricted in $|\eta| < 0.7$ and corrected for the energy loss (mass of $i^{\pm}$-particle was taken) [1] and vertexing.

- σ_{e^-/e^+} fixed to 1.2 and 0.8 for $0.2 < p_{\mathrm{T}} < 0.4$ and $0.4 < p_{\mathrm{T}} < 0.7$, respectively
- Fit σ_{K^-/K^+} as a function of p_{T}, for $0.3 < p_{\mathrm{T}} < 0.7$ GeV/c, with constant p_0 and fix it to the value of p_0
- The rest parameters from Step 1 are fixed to the values calculated from functions obtained in Step 1: μ_{π^-/π^+}, σ_{π^-/π^+}, μ_{e^-/e^+} , μ_{K^-/K^+}, $\mu_{\bar{p}/p}$, $\sigma_{\bar{p}/p}$

2. $K^{\pm}$:

   - Step 1 (Fig. 7.11):
     - Analyze data with $0.2 < p_{\mathrm{T}} < 0.6$ GeV/c
     - Fit μ_{π^-/π^+} as a function of p_{T} with $-\exp(p_0 + p_1 p_{\mathrm{T}})$
     - Fit σ_{π^-/π^+}, σ_{e^-/e^+}, σ_{K^-/K^+} as a function of p_{T} with $\exp(p_0 + p_1 p_{\mathrm{T}})$
     - Fit μ_{e^-/e^+} as a function of p_{T} with a polynomial $p_0 p_{\mathrm{T}}^3 + p_1 p_{\mathrm{T}}^2 + p_2 p_{\mathrm{T}} + p_3$
     - Fit μ_{K^-/K^+} as a function of p_{T} with a polynomial $p_0 + p_1 p_{\mathrm{T}}^2$
   - Step 2:
     - All parameters from Step 1 except σ_{e^-/e^+} are fixed to the values calculated from functions obtained in Step 1

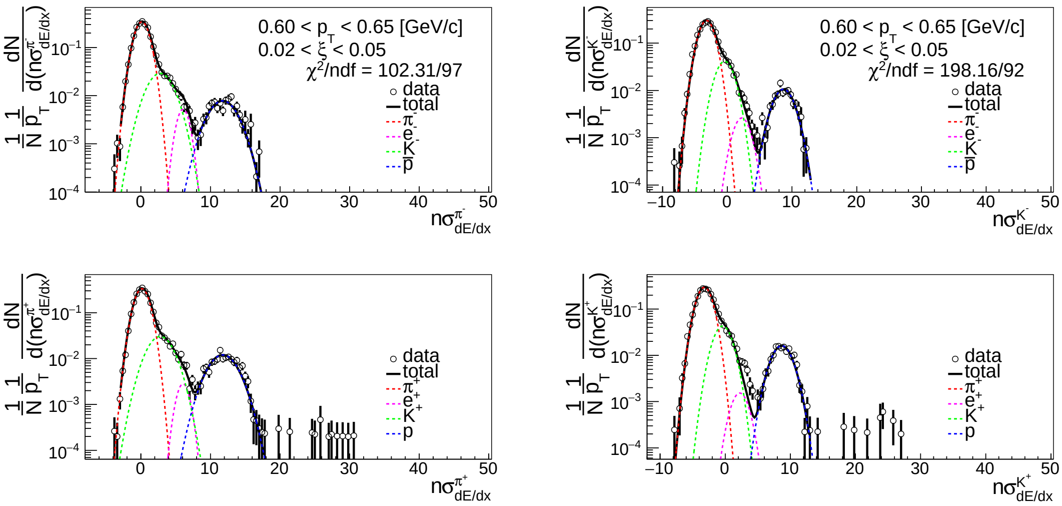

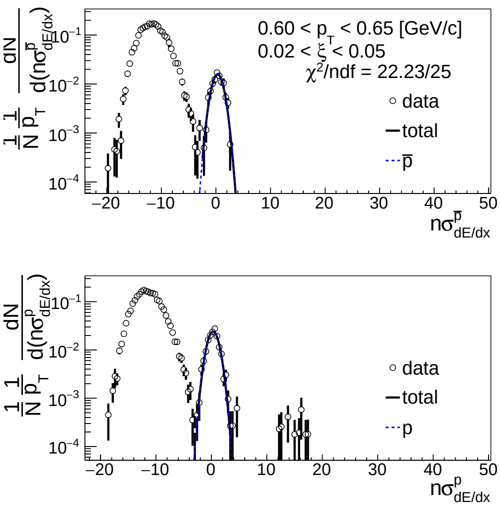

Figure 7.9: Distributions of (top left) $n\sigma^{\pi^\pm}_{dE/dx}$ for $\pi^\pm$, (top right) $n\sigma^{K^\pm}_{dE/dx}$ for $K^\pm$ and (bottom left) $n\sigma^{\bar{p}/p}_{dE/dx}$ for $\bar{p}/p$ in sample p_{T} bin and sample ξ range shown for each particle species. Particles are corrected for energy loss [1] and vertexing. The curves represent the Gaussian fits to the $n\sigma^{i}_{dE/dx}$ distributions.

  - Fit σ_{e^-/e^+} as a function of p_{T}, for $0.45 < p_{\mathrm{T}} < 0.65$ GeV/c, with constant p_0
- Step 3:
  - σ_{e^-/e^+} fixed to the values calculated from functions obtained in Steps 1 and 2 for $0.3 < p_{\mathrm{T}} < 0.45$ and $0.45 < p_{\mathrm{T}} < 0.65$, respectively.
  - The rest parameters from Step 1 are fixed to the values calculated from functions obtained in Step 1: μ_{π^-/π^+}, σ_{π^-/π^+}, μ_{e^-/e^+} , μ_{K^-/K^+},σ_{K^-/K^+}

3. $\bar{p}, p$:

- Step 1 (Fig. 7.12):
  - Analyze data with $0.4 < p_{\mathrm{T}} < 0.9$ GeV/c
  - Fit μ_{π^-/π^+}, μ_{K^-/K^+} as a function of p_{T} with a polynomial $p_0 p_{\mathrm{T}} + p_1$
  - Fit σ_{π^-/π^+} as a function of p_{T} with a polynomial $p_0 p_{\mathrm{T}}^2 + p_1 p_{\mathrm{T}} + p_2$
  - Fit σ_{K^-/K^+} as a function of p_{T} with $\exp\left(p_0 + p_1 p_{\mathrm{T}}\right)$
- Step 2:
  - μ_{K^-/K^+} fixed to the values calculated from a function obtained in Step 1

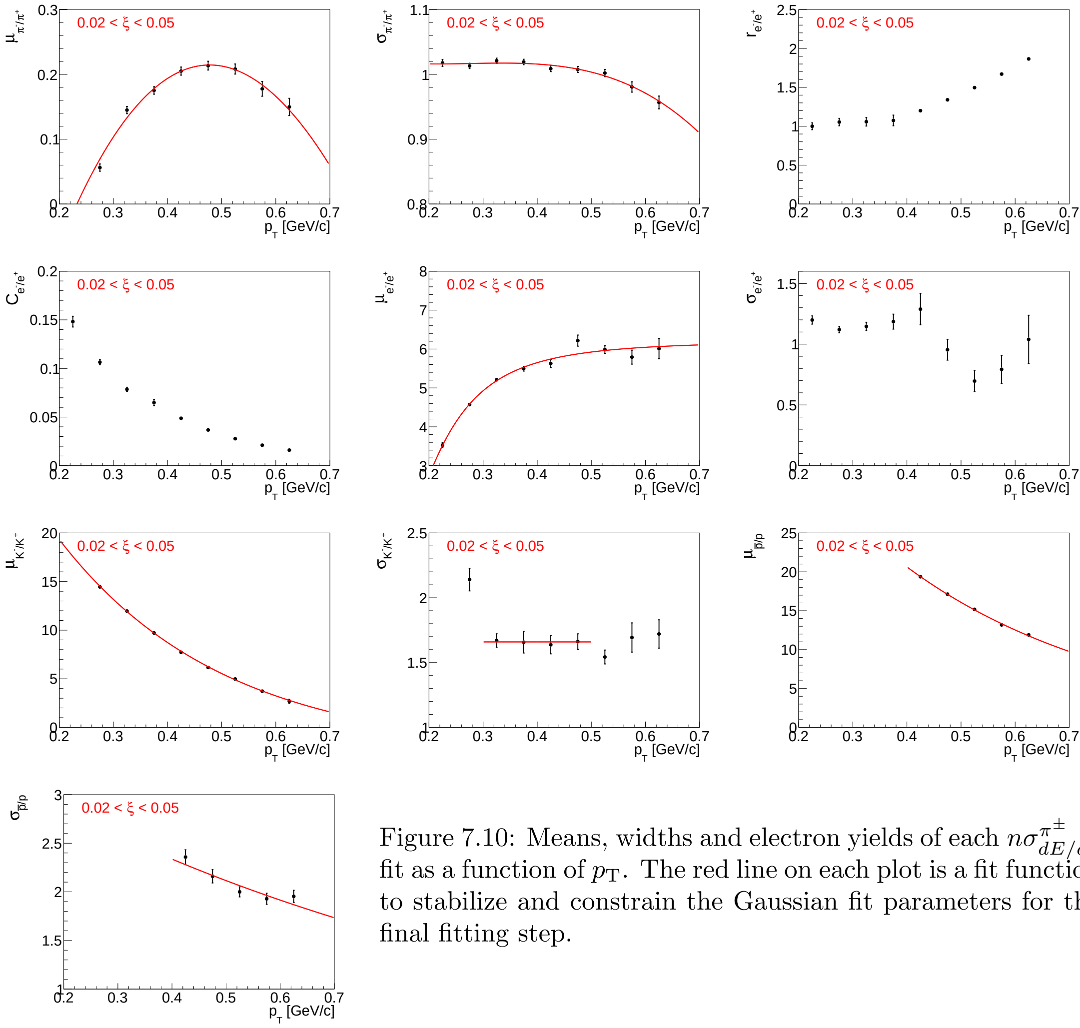

Figure 7.10: Means, widths and electron yields of each $n\sigma^{\pi^{\pm}}_{dE/dx}$ fit as a function of p_{T}. The red line on each plot is a fit function to stabilize and constrain the Gaussian fit parameters for the final fitting step.

  – All the rest parameters from Step 1 are limited to the values calculated from functions obtained in Step 1
  – Fit μ_{π^-/π^+}, σ_{π^-/π^+}, σ_{K^-/K^+} as a function of p_{T} with a polynomial $p_0 p_{\mathrm{T}}^2 + p_1 p_{\mathrm{T}} + p_2$
  – Fit $\mu_{\bar{p}/p}$ as a function of p_{T}, for $0.7 < p_{\mathrm{T}} < 1.0$ GeV/c, with constant p_0

- Step 3:
  – μ_{K^-/K^+} fixed to the values calculated from a function obtained in Step 1
  – $\mu_{\bar{p}/p}$ fixed to the values calculated from a function obtained in Step 2 for $0.7 < p_{\mathrm{T}} < 1.0$
  – The rest parameters from Step 2 are fixed to the values calculated from functions obtained in Step 2: μ_{π^-/π^+}, σ_{π^-/π^+}, σ_{K^-/K^+}

The particle yield is extracted from the fit to the corresponding $n\sigma^{i}_{dE/dx}$ distribution (corrected only for the energy loss and vertexing). As shown in Fig. 7.8, the dE/dx of each particle type merge at large p_{T}. Hence, the particle identification is limited. Pions can be identified in the momentum range of $0.2 - 0.7$ GeV/c, kaons in $0.3 - 0.65$ GeV/c and (anti)protons in $0.4 - 1.0$ GeV/c.

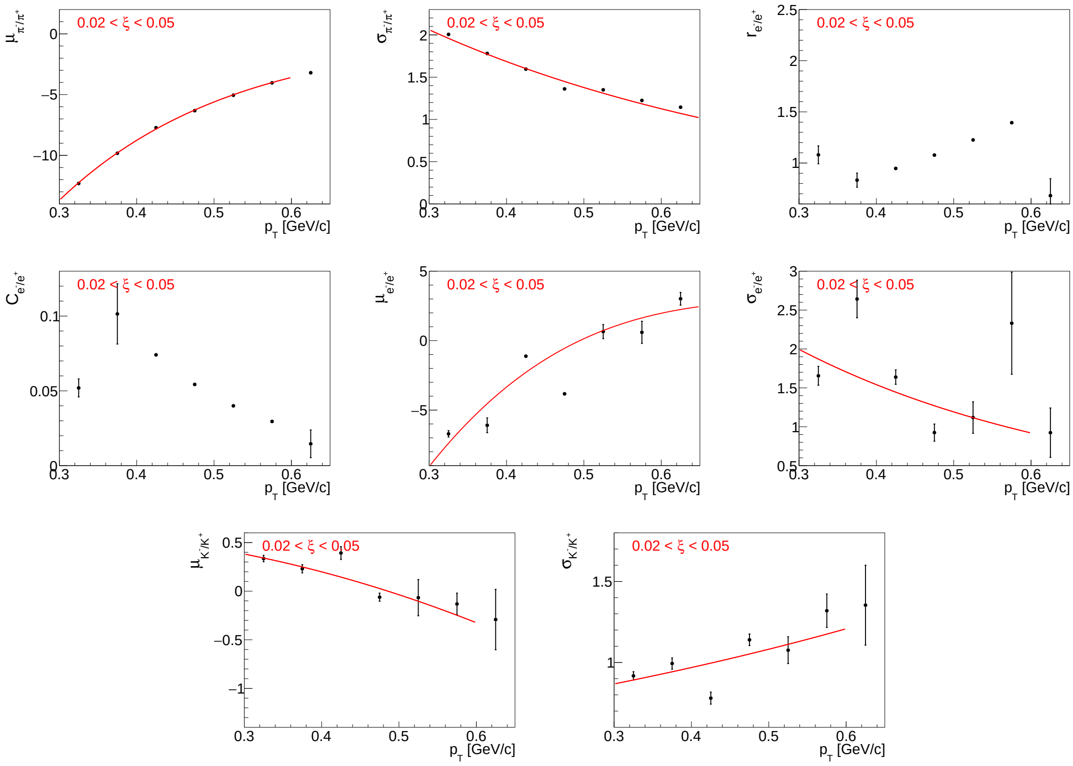

Figure 7.11: Means, widths and electron yields of each $n\sigma^{K^{\pm}}_{dE/dx}$ fit as a function of p_{T}. The red line on each plot is a fit function to stabilize and constrain the Gaussian fit parameters for the final fitting step.

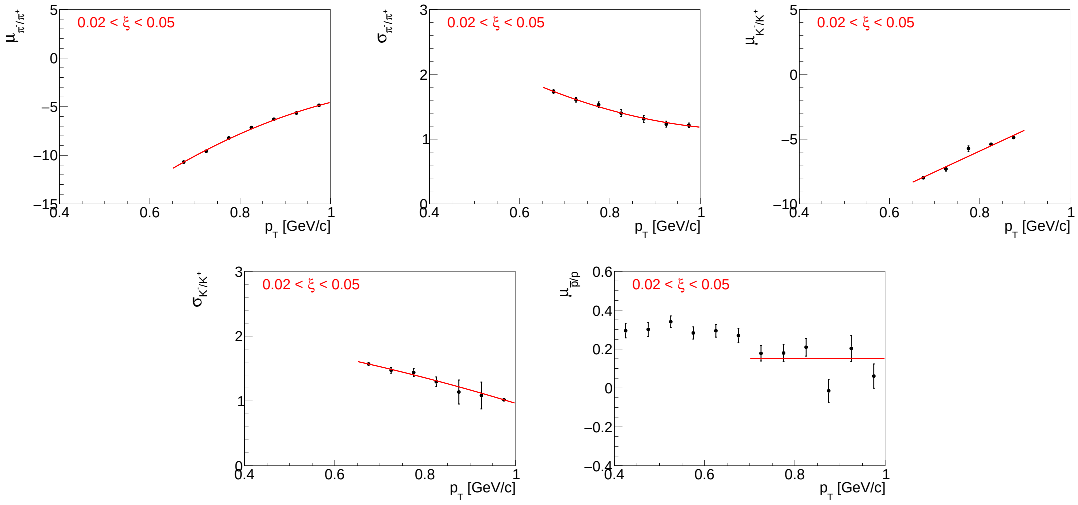

Figure 7.12: Means and widths of each $n\sigma^{\bar{p}/p}_{dE/dx}$ fit as a function of p_{T}. The red line on each plot is a fit function to stabilize and constrain the Gaussian fit parameters for the final fitting step.

7.6 Antiparticle-to-Particle Ratios

The following steps were taken to correct the identified antiparticle to particle (pion, kaon, proton and their antiparticle) multiplicity ratios as a function of p_T in three ranges of ξ:

- The raw identified particle yields were obtained through multi-Gaussian fits to the $n\sigma^{i}_{dE/dx}$ distributions (Sec. 7.5), where the vertex reconstruction and energy loss corrections [1] were applied. The latter depends on the particle type.
- The non-SD background (Sec. 4.2) is the same for particles and antiparticles, thus, it was not subtracted. The accidental background contribution (Sec. 4) is very small, hence, any particle-antiparticle differences have a negligible effect on the result. Therefore, it was assumed that the accidental background does not depend on the particle type and for this reason it was not subtracted.
- The particle yields were corrected for track reconstruction efficiencies [1], which depend on the particle type and charge. These corrections are averaged over η and V_z. The ratio of particle to antiparticle TPC-TOF efficiencies is shown in Fig. 7.13. It weakly depends on ξ range, therefore, only sample results for single range of $0.02 < \xi < 0.05$ are presented.
- The background from non-primary tracks was subtracted (Sec. 4.1):
  - $\pi^{\pm}$: weak decays pions, muon contribution and background from detector dead-material interactions,
  - p: background from detector dead-material interactions,
  - $p, \bar{p}$: reconstructed tracks which have the appropriate number of common hit points with true-level particle, but the distance between them is too large (this background is negligibly small for other particle types),
  - fake track contribution was assumed to be the same for each particle type, hence, it was not subtracted.
- Since track and ξ migrations, and BBC-small efficiency, do not depend on the particle type and charge, these corrections are not applied.
- Finally, each antiparticle p_T distribution was divided by the corresponding particle p_T distribution to obtain fully corrected identified antiparticle to particle multiplicity ratios.
- Additionally, the average antiparticle to particle ratios over fiducial region of p_T in each ξ region were calculated.

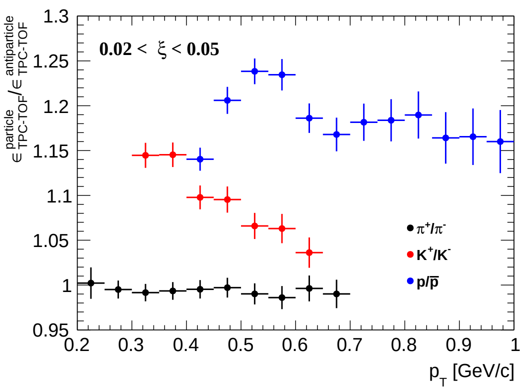

Figure 7.13: Ratio of particle to antiparticle TPC-TOF efficiencies for $0.02 < \xi < 0.05$.

8. Systematic Uncertainties

Apart from the statistical uncertainties there are also systematic uncertainties originating from inefficiencies and limitations of the measurement devices and techniques. The following sources of systematic uncertainties were considered:

- the effect of off-time pile-up on TPC track reconstruction efficiency [1],
- the uncertainty of TPC track reconstruction efficiency related to the description of dead-material in simulation [1],
- representation of data sample in embedding MC [1],
- variation in the track quality cuts [1],
- non-primary track background contribution (Sec. 4.1),
- fake track background contribution (Sec. 4.1),
- TOF system simulation accuracy [1],
- accidental background contribution (Sec. 4),
- the effect of alternative model of hadronization on BBC-small efficiency (Sec. 5.2),
- non-SD background contribution (Sec. 4.2),
- the effect of alternative model on ϵ_m correction (Sec. 7.1),
- non-closure (Sec 7.3),
- non-closure of N_{ev}, applied only to p_{T} and $\bar{\eta}$ distributions,
- difference in the distributions calculated separately for events in which forward proton is on one and the other side of the IP (east-west, Sec 7.4).

Some of the systematic uncertainties on $1/N\ dN/dn_{\text{ch}}$ (related to TPC and TOF reconstruction efficiencies, fake track background contribution) are propagated by randomly removing and adding tracks in the n_{sel} distribution before unfolding procedure. For each track, a random number is generated. If this number is smaller than the absolute value of systematic uncertainty, then n_{sel} is increased or decreased, depending on the sign of systematic uncertainty.

Figures 8.1 to 8.3 show the components contributing to the total systematic uncertainty for charged particle distributions without the identification. The dominant systematic uncertainty for p_{T} and n_{ch} distributions is related to TOF system simulation accuracy. It affects mainly low-p_{T} particles, where it is about $2-3\%$, and large charged particle multiplicities, where it varies up to 20% for $n_{\text{ch}} = 8$ and $0.02 < \xi < 0.05$. In case of $\bar{\eta}$ distribution, the systematic uncertainty on TOF mainly refers to charged particles produced at the edge of the fiducial region, for which it is about 2%. The largest (up to 30%) systematic uncertainty for $\langle\bar{\eta}\rangle$, is related to the observed difference in the distributions calculated separately with respect to the forward-scattered proton direction. The rest of the components have smaller contributions to the total systematic uncertainty. The systematic uncertainty on non-closure is on average at the level of 2% which proves the accuracy of the correction procedure.

Figures 8.4 to 8.7 show breakdown of all different systematics for the antiparticle-to-particle multiplicity ratio distributions. An additional systematic contribution for $\bar{p}/p$ multiplicity ratio due to proton background estimation was introduced. Since most of the corrections are the same for particle and its antiparticle, nearly all systematic uncertainties cancel out in the antiparticle-to-particle ratios. The largest sources of systematics, which do not, are related to proton background estimation and dead-material effect on TPC track reconstruction efficiency. The former was found to be up to 6%, whereas the latter varies up to 2% for low-p_{T} $\bar{p}/p$ multiplicity ratio.

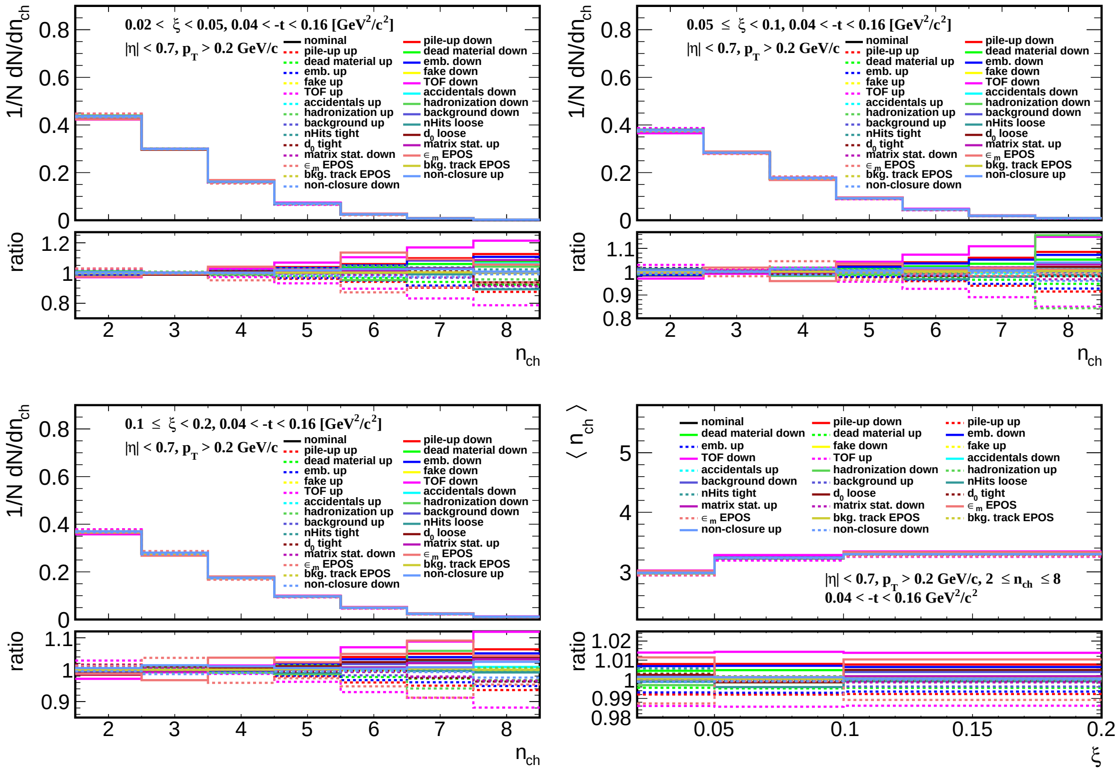

Figure 8.1: Components of the systematic uncertainties for the charged particle multiplicity in three ξ regions and for the average charged particle multiplicity.

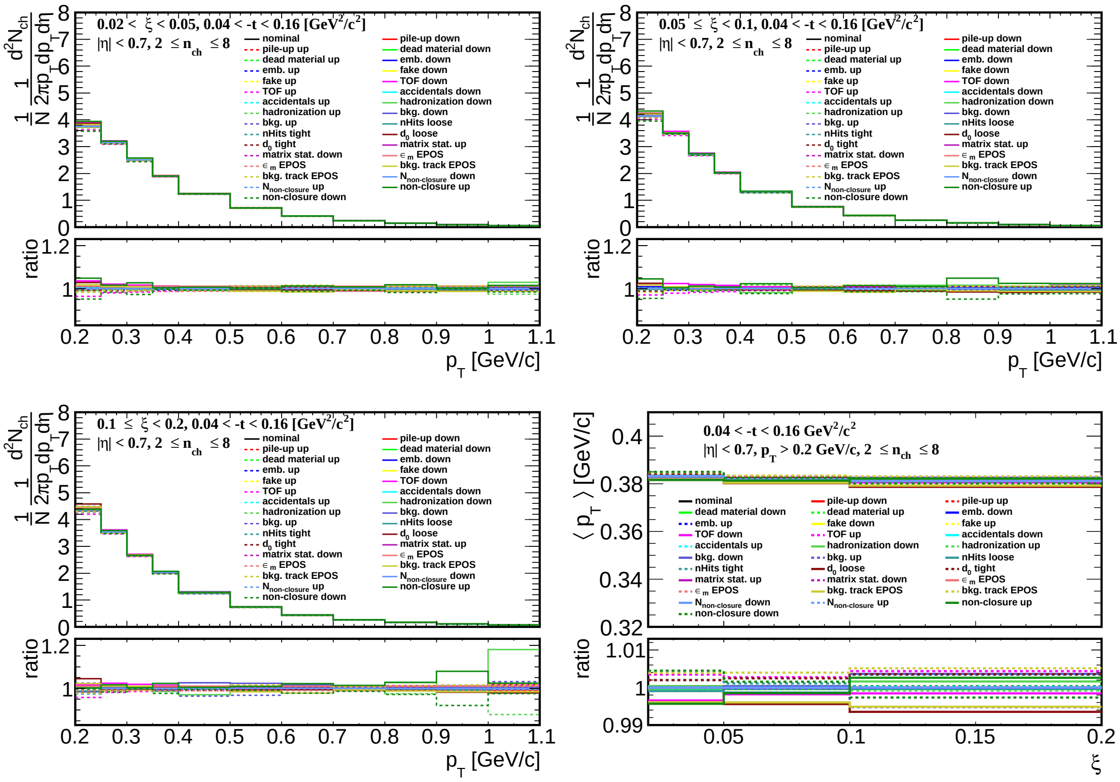

Figure 8.2: Components of the systematic uncertainties for p_T distributions in three ξ regions and for an average p_T distribution.

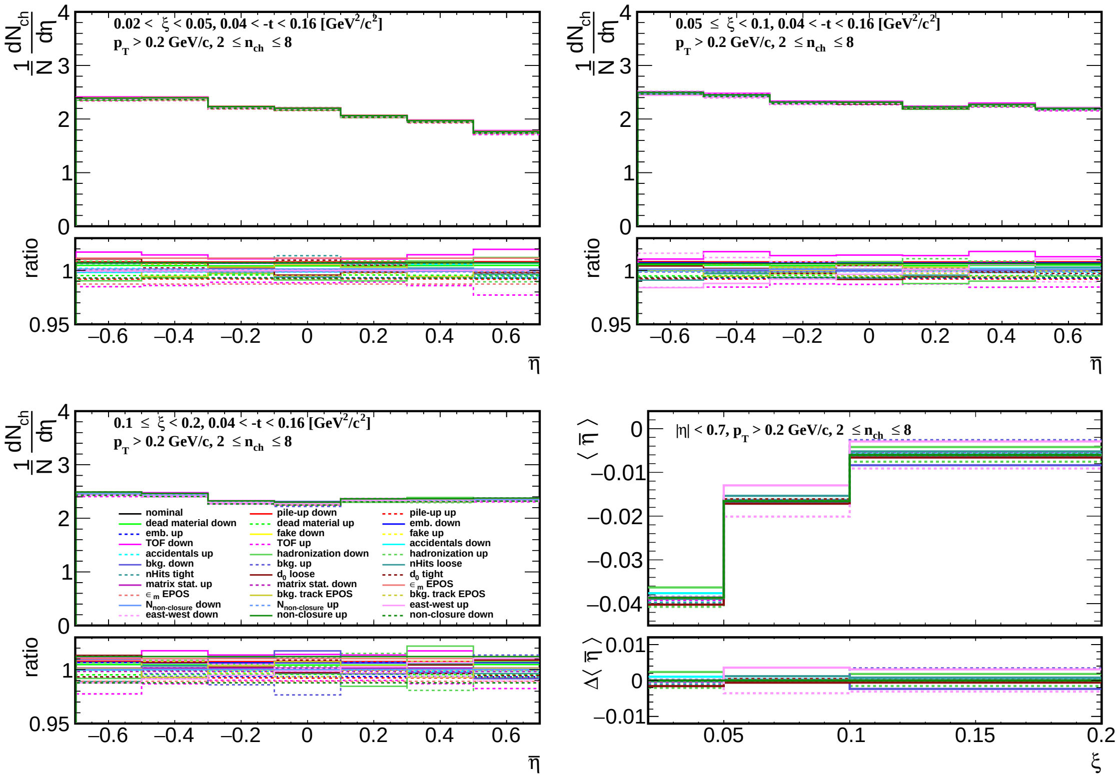

Figure 8.3: Components of the systematic uncertainties for $\bar{\eta}$ distributions in three ξ regions and for an average $\bar{\eta}$ distribution.

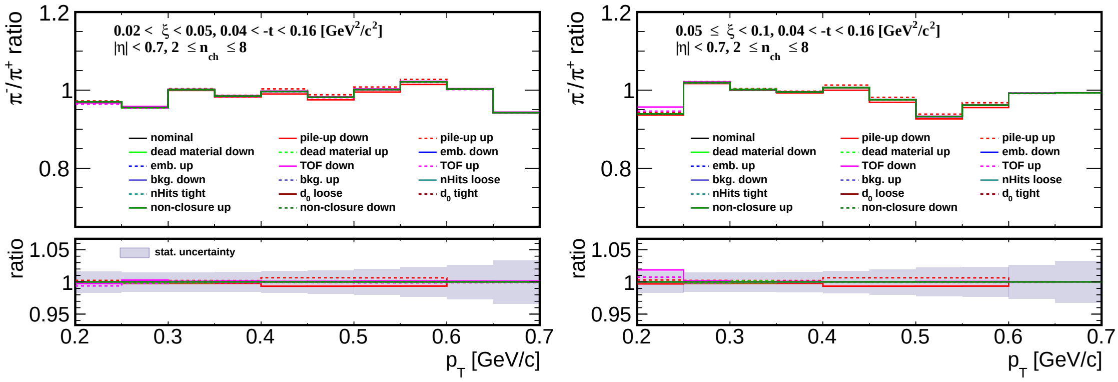

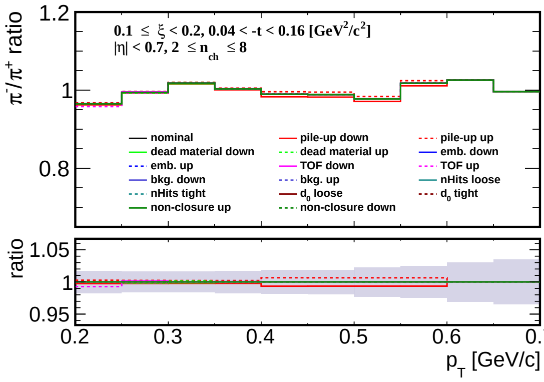

Figure 8.4: Components of the systematic uncertainties of π^-/π^+ multiplicity ratios in three ξ regions. The gray band in the bottom pad represents statistical uncertainties.

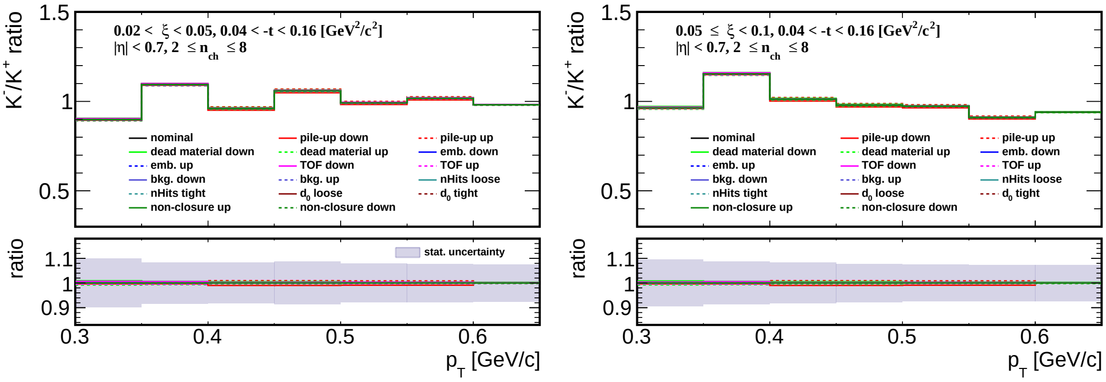

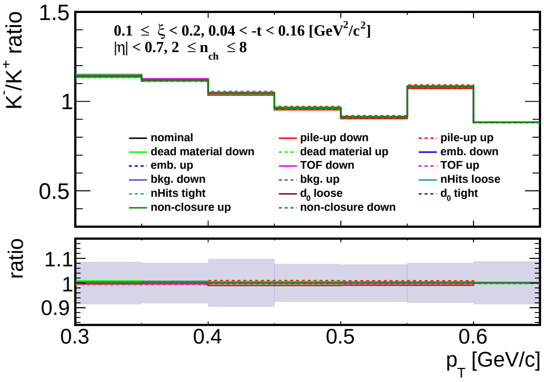

Figure 8.5: Components of the systematic uncertainties of K^-/K^+ multiplicity ratios in three ξ regions. The gray band in the bottom pad represents statistical uncertainties.

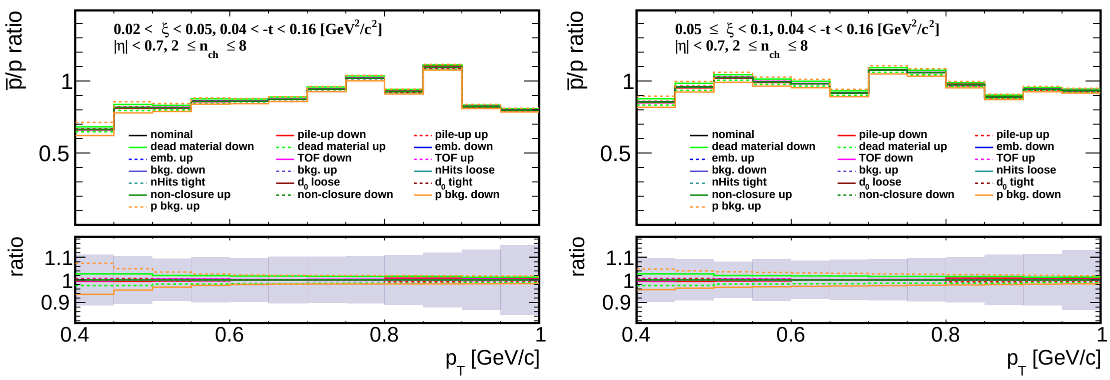

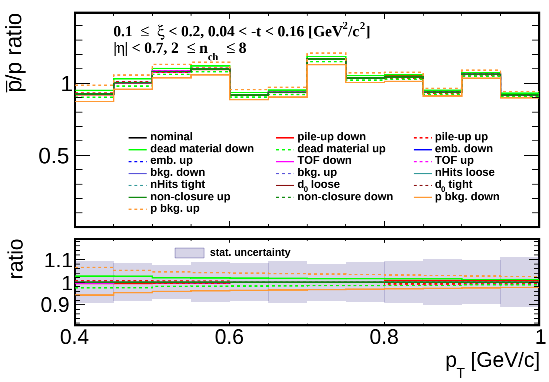

Figure 8.6: Components of the systematic uncertainties of $\bar{p}/p$ multiplicity ratios in three ξ regions. The gray band in the bottom pad represents statistical uncertainties.

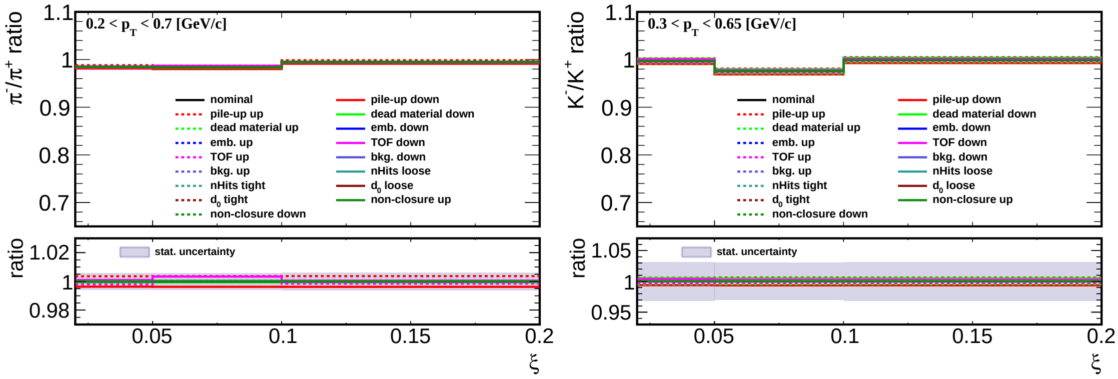

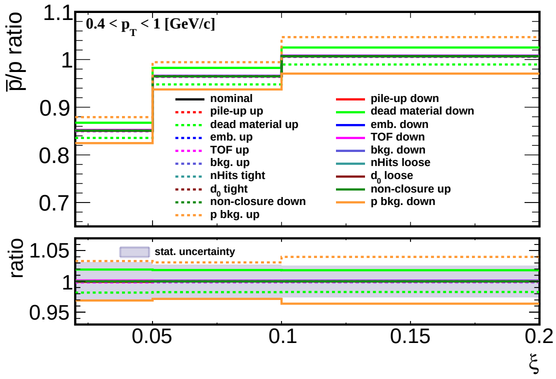

Figure 8.7: Components of the systematic uncertainties of average antiparticle-to-particle multiplicity ratios in three ξ regions. The gray band in the bottom pad represents statistical uncertainties

Figures 8.8 and 8.9 show breakdown of all different systematics for the $(K^- + K^+) / (\pi^- + \pi^+)$ multiplicity ratio distributions. The largest sources of systematics are related to TOF reconstruction efficiencies and dead-material effect on TPC track reconstruction efficiency. The former was found to be up to 4%, whereas the latter varies up to 5% for low-p_T multiplicity ratio.

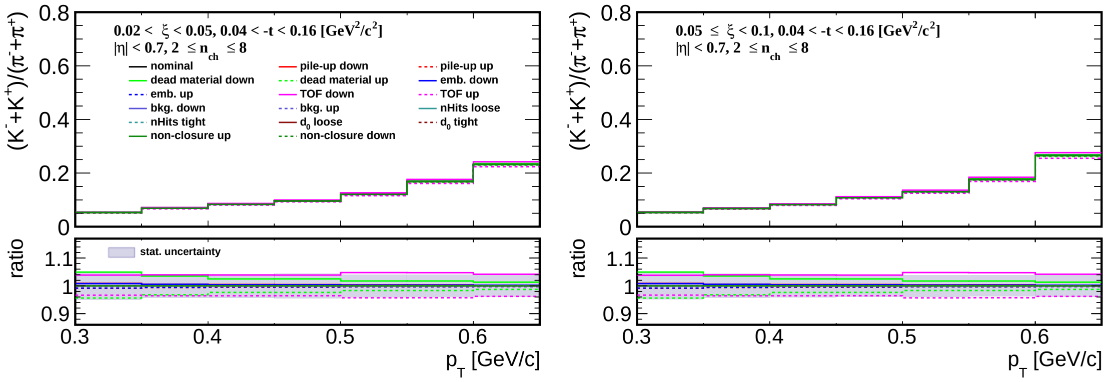

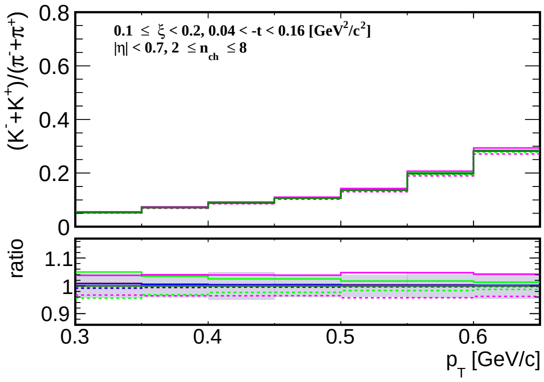

Figure 8.8: Components of the systematic uncertainties of $(K^- + K^+) / (\pi^- + \pi^+)$ multiplicity ratios in three ξ regions. The gray band in the bottom pad represents statistical uncertainties.

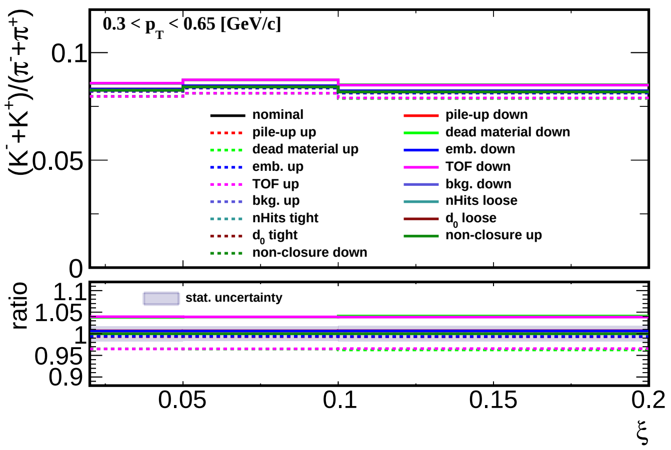

Figure 8.9: Components of the systematic uncertainties of average $(K^- + K^+) / (\pi^- + \pi^+)$ multiplicity ratios in three ξ regions. The gray band in the bottom pad represents statistical uncertainties

9. Results

In the following section, the final-state charged particle distributions are compared with various SD MC predictions, i.e.

- PYTHIA 8 4C (SaS),
- PYTHIA 8 A2 (MBR),
- PYTHIA 8 A2 (MBR-tuned),
- HERWIG 7,
- EPOS LHC with combined two classes of processes: diffractive (EPOS SD) and non-diffractive (EPOS SD′),
- EPOS LHC SD′.

In all figures, data are shown as solid points with error bars representing the statistical uncertainties. Gray boxes represent statistical and systematic uncertainties added in quadrature. Predictions from MC models are shown as colour histograms and markers. The lower panel in each figure shows the ratio of data to the models' predictions. All results are presented separately for three ranges of ξ: $0.02 < \xi < 0.05$, $0.05 < \xi < 0.1$, $0.1 < \xi < 0.2$.

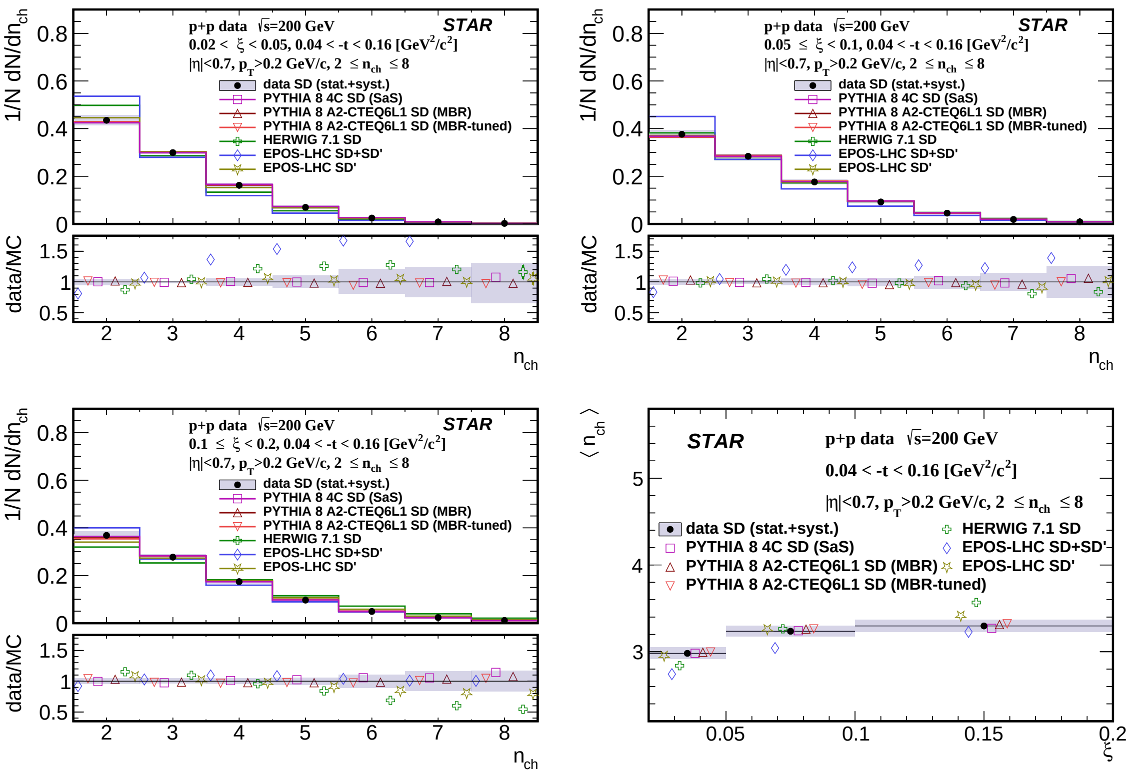

Figure 9.1: Primary charged-particle multiplicity shown separately for the three ranges of ξ: (top left) $0.02 < \xi < 0.05$, (top right) $0.05 < \xi < 0.1$, (bottom left) $0.1 < \xi < 0.2$ and (bottom right) the mean multiplicity $\langle n_{\rm ch} \rangle$ as a function of ξ.

Figure 9.1 shows primary charged-particle multiplicity separately for the three ranges of ξ and the mean multiplicity $\langle n_{\mathrm{ch}}\rangle$ as a function of ξ. Data follow the expected increase of $\langle n_{\mathrm{ch}}\rangle$ with ξ due to the larger diffractive masses probed by increasing ξ in SD process. The shapes of the measured distributions are reproduced reasonably well by all models except EPOS SD+SD′ and HERWIG SD which predicts smaller $\langle n_{\mathrm{ch}}\rangle$ for $0.02 < \xi < 0.1$ and $0.02 < \xi < 0.05$, respectively. HERWIG SD predicts too large $\langle n_{\mathrm{ch}}\rangle$ for $0.1 < \xi < 0.2$.

Figure 9.2 shows primary charged-particle multiplicities as a function of p_{T} separately for the three ranges of ξ and the mean transverse momentum $\langle p_{\mathrm{T}}\rangle$ as a function of ξ. Data show that $\langle p_{\mathrm{T}}\rangle$ depends very weakly on ξ. Models describe data fairly well except HERWIG SD which predicts much steeper dependence of particle density with p_{T} in all three ξ ranges.

Figure 9.3 shows primary charged-particle multiplicity as a function of $\bar{\eta}$ separately for the three ranges of ξ and the mean pseudorapidity $\langle\bar{\eta}\rangle$ as a function of ξ. Data show expected flattening of the $\bar{\eta}$ distribution with increasing ξ which reflects SD event-asymmetry and fact that the gap-edge at large ξ is outside $|\bar{\eta}| < 0.7$ region leading to more flat distribution of particle density as a function of $\bar{\eta}$. PYTHIA 8 models describe data fairly well only at $0.02 < \xi < 0.05$ and predicts flatter distributions for $0.05 < \xi < 0.2$. EPOS SD+SD′ and HERWIG SD predict less and more steep dependence of particle density with $\bar{\eta}$ for all three ξ ranges, respectively.

Figure 9.4 shows the ratio of production yields of π^-/π^+ as a function of p_{T} separately for the three ranges of ξ. Data in all three ξ ranges are consistent with equal amounts of π^+ and π^- with no significant p_{T} dependence. Models agree with data (except HERWIG) predicting on average small deviation from unity by $\sim 2\%$ what is smaller than data uncertainties. HERWIG in first two ξ ranges predicts too large asymmetry between π^+ and π^-.

Figure 9.5 shows the ratio of production yields of K^-/K^+ as a function of p_{T} separately for

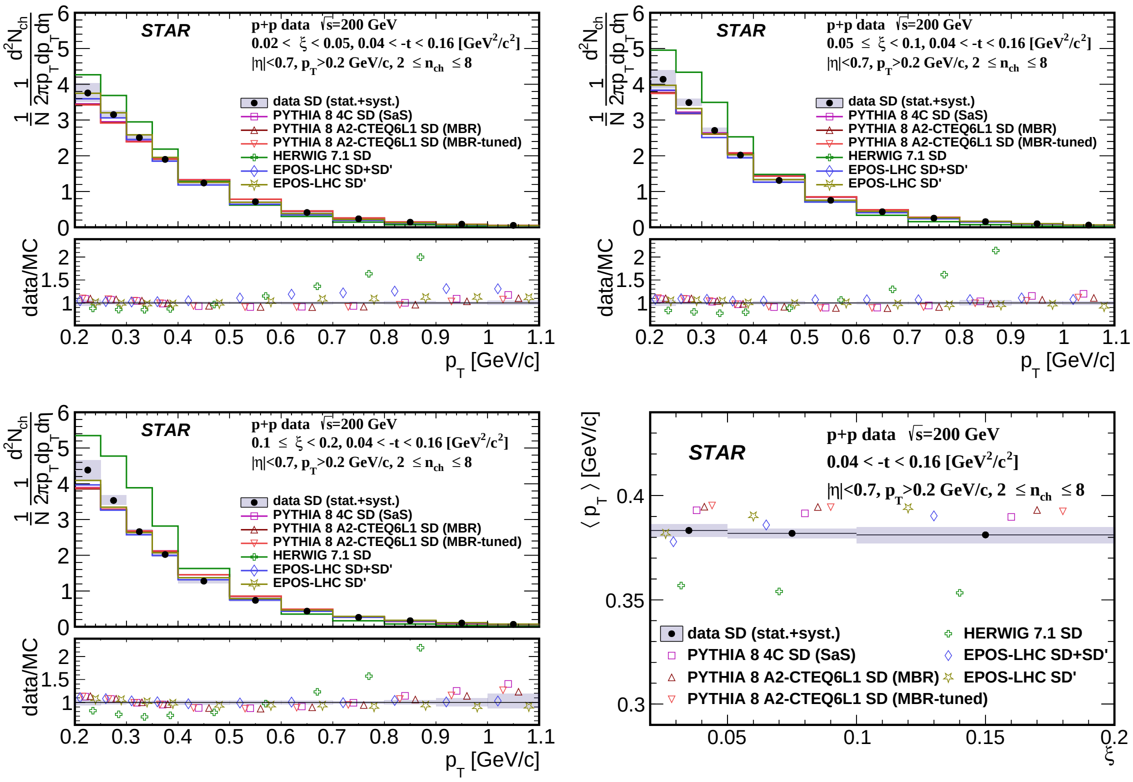

Figure 9.2: Primary charged-particle multiplicities as a function of p_{T} shown separately for the three ranges of ξ: (top left) $0.02 < \xi < 0.05$, (top right) $0.05 < \xi < 0.1$, (bottom left) $0.1 < \xi < 0.2$ and (bottom right) the mean transverse momentum $\langle p_{\mathrm{T}}\rangle$ as a function of ξ.

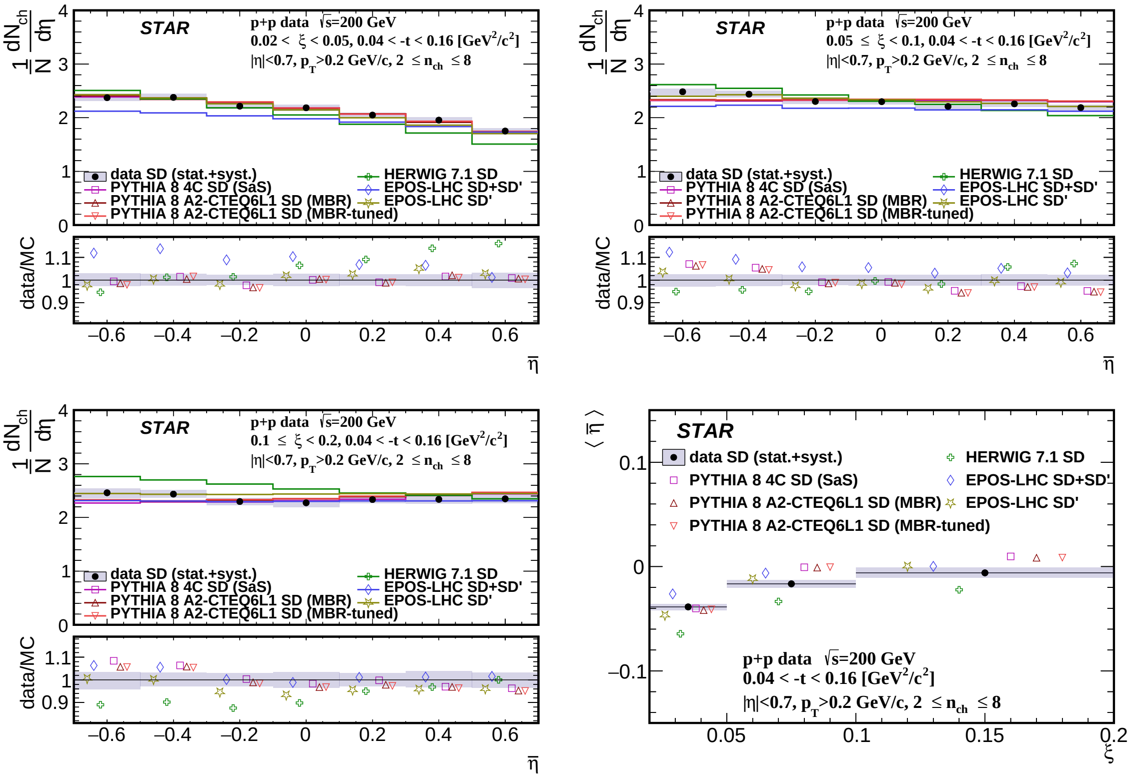

Figure 9.3: Primary charged-particle multiplicity as a function of $\bar{\eta}$ shown separately for the three ranges of ξ: (top left) $0.02 < \xi < 0.05$, (top right) $0.05 < \xi < 0.1$, (bottom left) $0.1 < \xi < 0.2$ and (bottom right) the mean pseudorapidity $\langle\bar{\eta}\rangle$ as a function of ξ.

the three ranges of ξ. Data in all three ξ ranges are consistent with equal amounts of K^+ and K^- with no p_{T} dependence. Models agree with data except HERWIG in the first ξ range predicting too large ratio of K^- to K^+.

Figure 9.6 shows the ratio of production yields of $\bar{p}/p$ as a function of p_{T} separately for the three ranges of ξ. Data in the last two ξ ranges are consistent with equal amounts of p and $\bar{p}$ with no p_{T} dependence. However, in the first ξ range at $p_{\mathrm{T}} < 0.7$ GeV/c data shows significant deviation from unity indicating a significant transfer of the baryon number from the forward to the central region. PYTHIA8, EPOS SD$'$ and EPOS SD+SD$'$ agree with data in the last two ξ ranges. In first ξ range PYTHIA8 and EPOS SD$'$ predict small deviation from unity by $\approx 7\%$ which is smaller than observed in data ($\bar{p}/p = 0.85 \pm 0.04$), whereas EPOS SD+SD$'$ predicts an asymmetry between $\bar{p}$ and p of $\sim 30\%$ which is larger than observed in data except $p_{\mathrm{T}} < 0.5$ GeV/c. HERWIG predicts much larger baryon number transfer compared to data in first two ξ ranges and shows consistency with data in last ξ range.

Figure 9.7 shows mean ratio of production yields of π^-/π^+, K^-/K^+ and $\bar{p}/p$ as a function of ξ.

Figures 9.8 shows the ratio of production yields of $(K^- + K^+) / (\pi^- + \pi^+)$ as a function of p_{T} separately for the three ranges of ξ.

Figure 9.9 shows mean ratio of production yields of $(K^- + K^+) / (\pi^- + \pi^+)$ as a function of ξ.

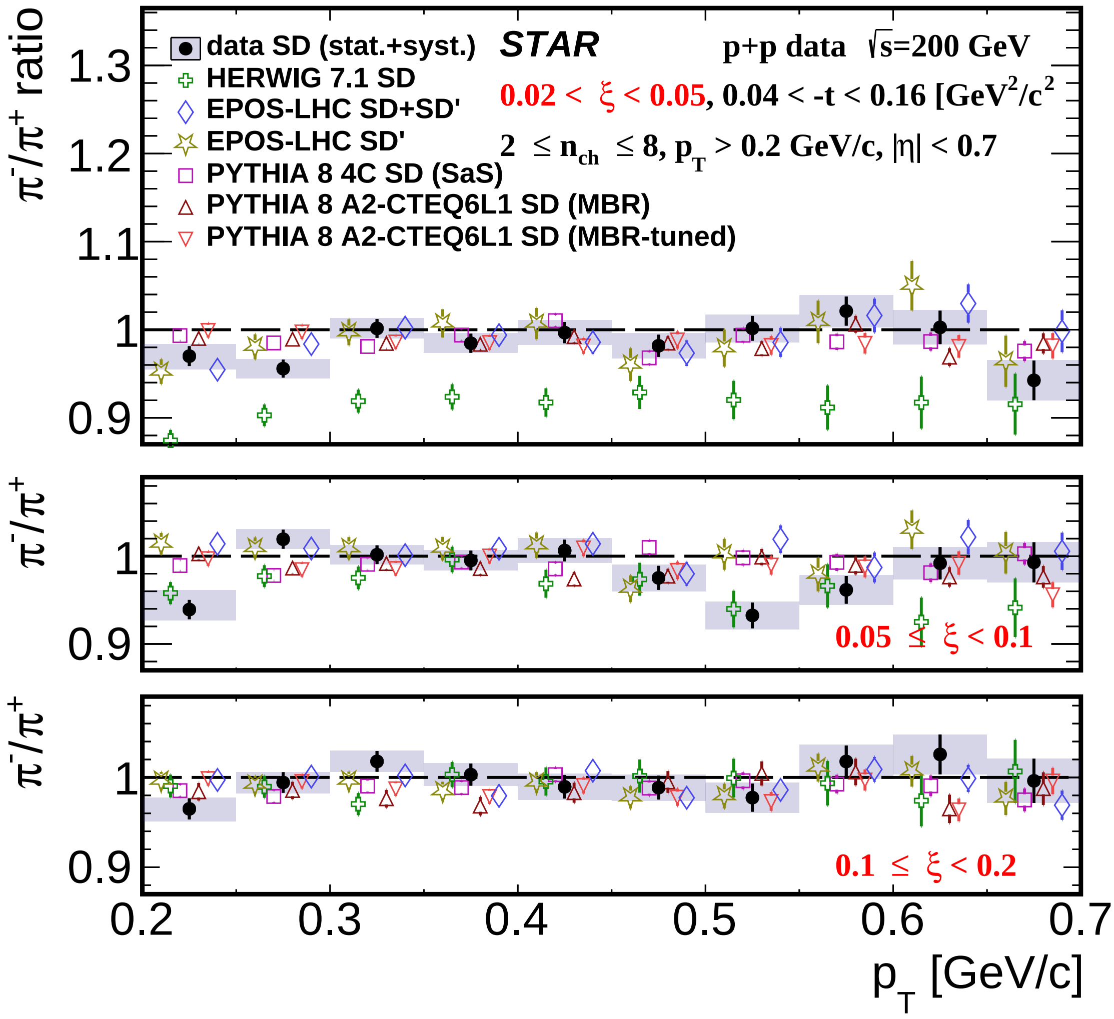

Figure 9.4: Ratio of production yields of π^-/π^+ as a function of p_T shown separately for the three ranges of ξ: (top) $0.02 < \xi < 0.05$, (middle) $0.05 < \xi < 0.1$, (bottom) $0.1 < \xi < 0.2$.

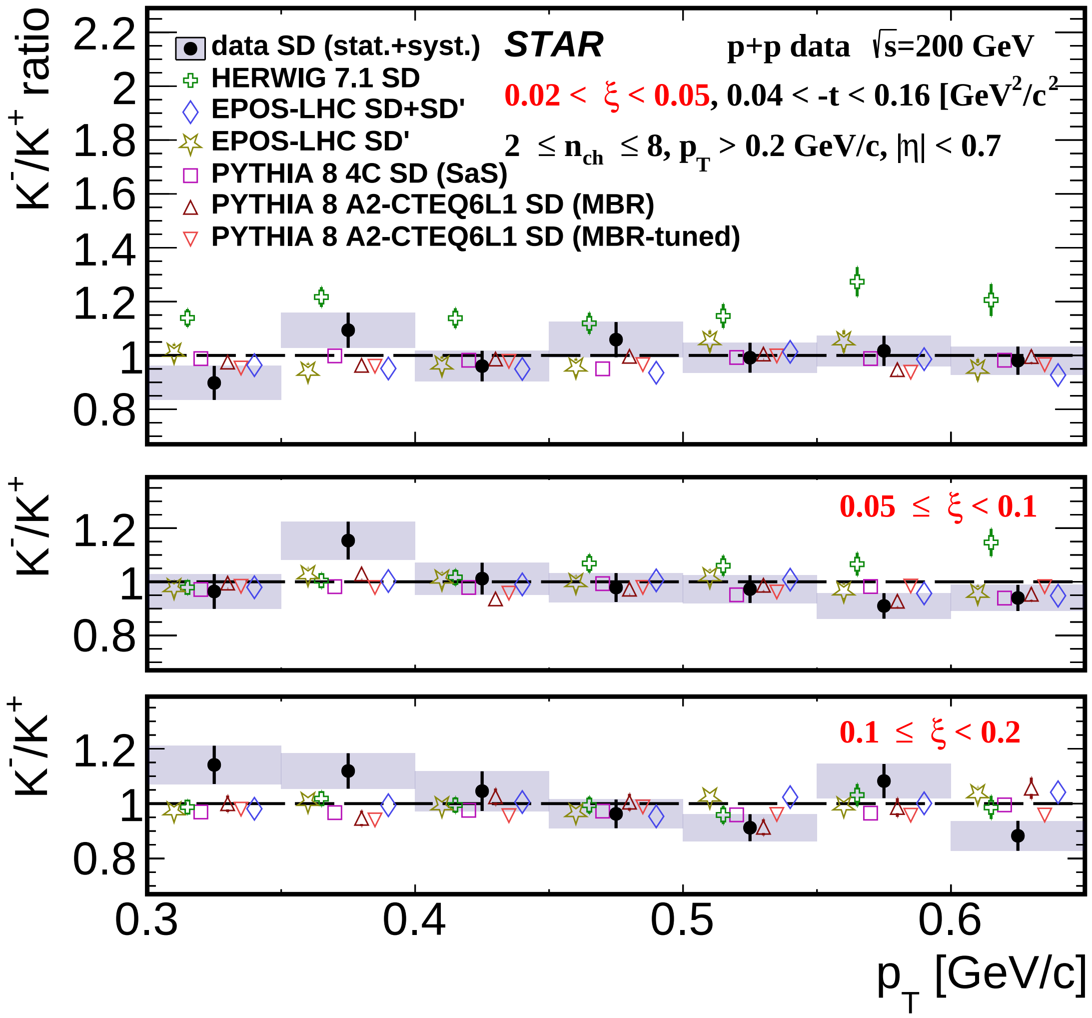

Figure 9.5: Ratio of production yields of K^-/K^+ as a function of p_T shown separately for the three ranges of ξ: (top) $0.02 < \xi < 0.05$, (middle) $0.05 < \xi < 0.1$, (bottom) $0.1 < \xi < 0.2$.

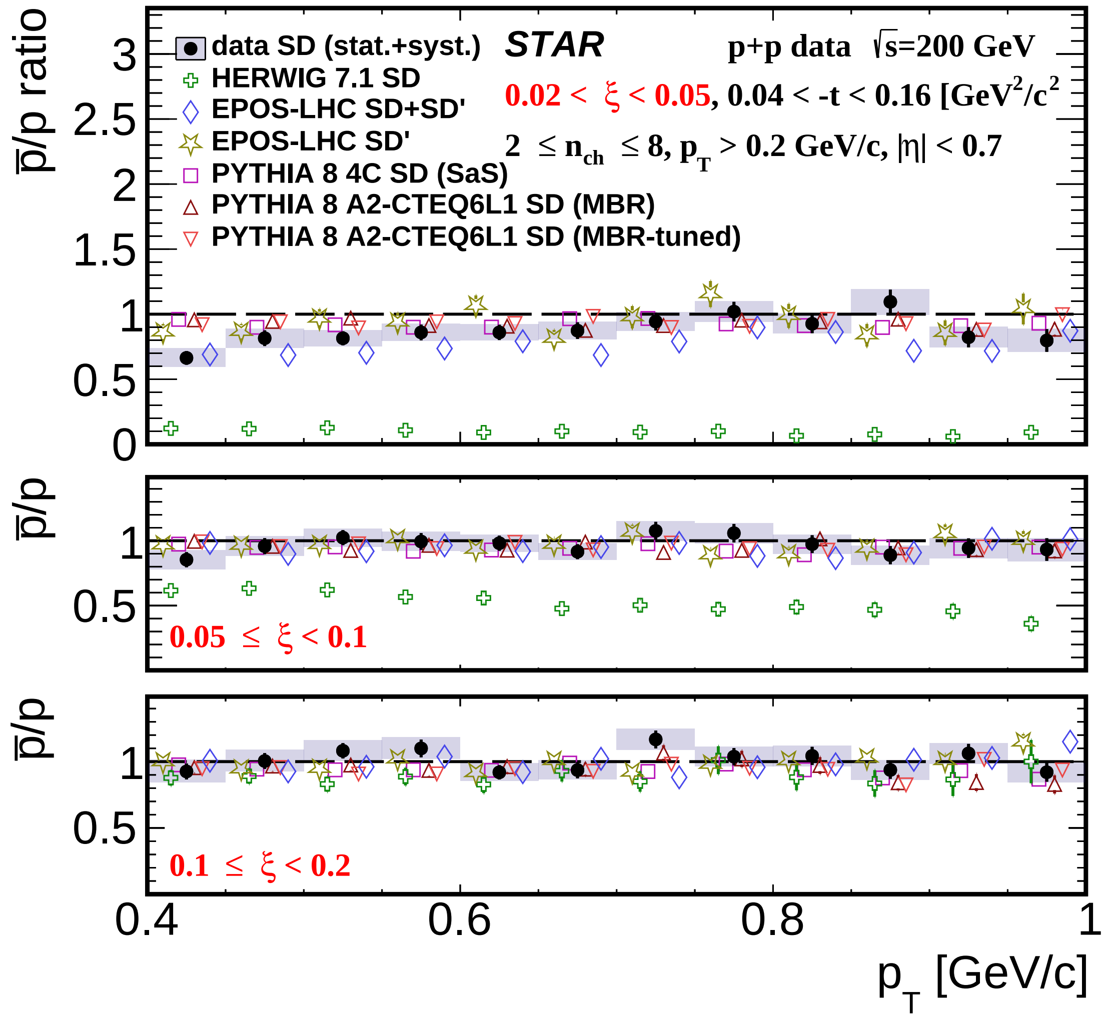

Figure 9.6: Ratio of production yields of $\bar{p}/p$ as a function of p_{T} shown separately for the three ranges of ξ: (top) $0.02 < \xi < 0.05$, (middle) $0.05 < \xi < 0.1$, (bottom) $0.1 < \xi < 0.2$.

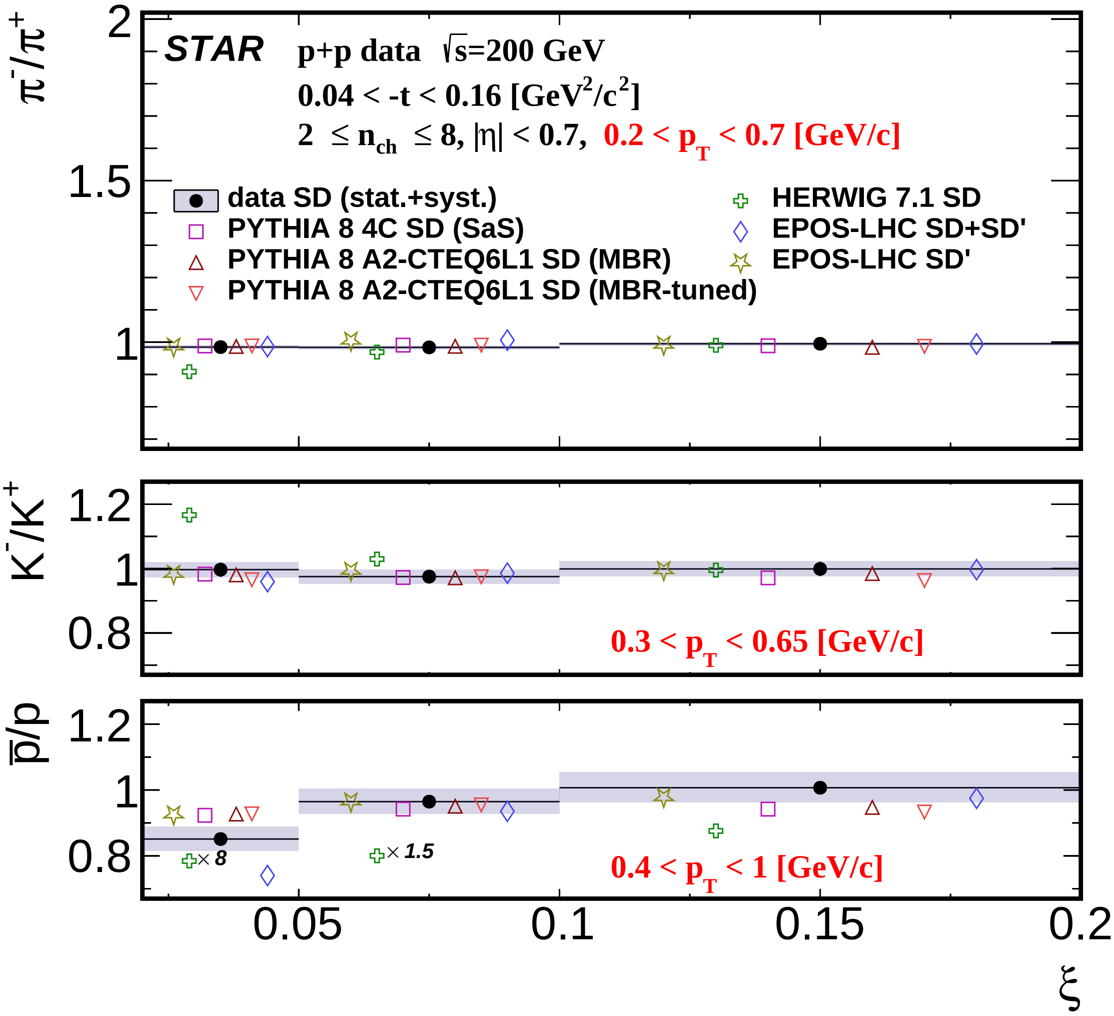

Figure 9.7: Ratio of production yields of π^-/π^+, K^-/K^+ and $\bar{p}/p$ as a function of ξ.

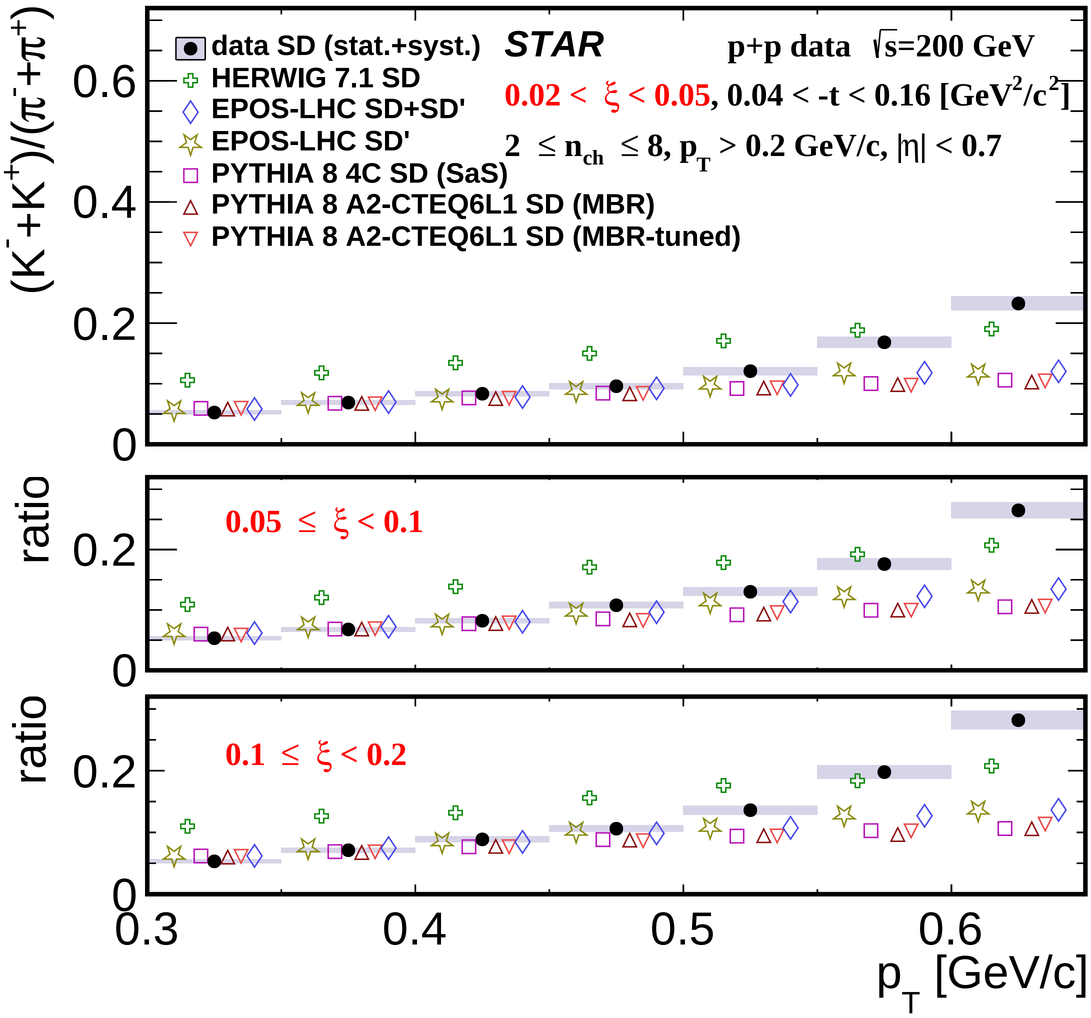

Figure 9.8: Ratio of production yields of $(K^- + K^+)\,/\,(\pi^- + \pi^+)$ as a function of p_T shown separately for the three ranges of ξ: (top) $0.02 < \xi < 0.05$, (middle) $0.05 < \xi < 0.1$, (bottom) $0.1 < \xi < 0.2$.

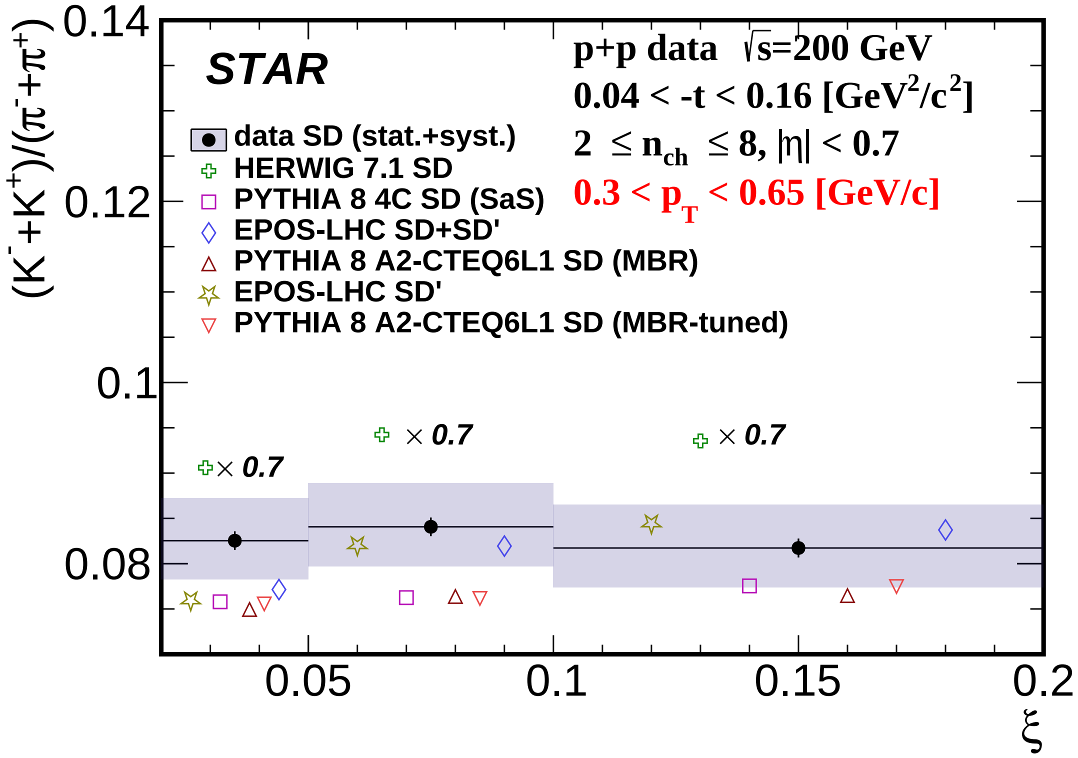

Figure 9.9: Ratio of production yields of $(K^- + K^+) / (\pi^- + \pi^+)$ as a function of ξ.

9.1 Comparison of Charged-Particle Densities at Central Rapidities

The measured charged-particle densities in pseudorapidity near $\eta \approx 0$ are compared to other experimental results from pp and $p\bar{p}$ collisions (shown in Fig. 9.10). Various event selections, based on the topology of the final state, allow to split the data samples into enhanced in non-SD (NSD) and SD events, whose sum forms the inelastic sample. For SD events, the midrapidity region is located at $\bar{\eta} = \eta_m = -\ln(\sqrt{s}/M_X)$, instead of $\eta \approx 0$, and the proper energy scale is given by M_X instead of $\sqrt{s}$. The values of η_m and $\langle M_X \rangle$, calculated for STAR data, are presented in Tab. 9.1. For all three ranges of ξ, the value of η_m is outside the fiducial region of the measurement. In the case of other experiments the pseudorapidity densities were obtained in the region of the total number of primary charged particles $n_{\mathrm{ch}} \geq 1$ (instead of $n_{\mathrm{ch}} \geq 2$ as in this analysis). Therefore, the results from STAR analysis were extrapolated to the above fiducial region using PYTHIA 8 A2 (MBR) SD predictions. The uncertainties due to the corrections are not estimated.

ξ range	$\langle M_X \rangle$	η_m	η_{edge}
$0.02 < \xi < 0.05$	37.53 GeV	−1.67	2.02
$0.05 < \xi < 0.1$	53.52 GeV	−1.31	2.73
$0.1 < \xi < 0.2$	72.71 GeV	−1.01	3.34

Table 9.1: Values of $\langle M_X \rangle$ and $\eta_m = \ln(\sqrt{s}/M_X)$ for three ranges of ξ and position of gap edge η_{edge}.

The extrapolation procedure was as follows:

1. the ratio of particle density at $\bar{\eta} = \eta_m$ and $n_{\mathrm{ch}} \geq 1$ to that at $\bar{\eta} = 0$ and $n_{\mathrm{ch}} \geq 2$ was calculated using PYTHIA 8 predictions,
2. differences in the slope of the pseudorapidity distribution in the region of $n_{\mathrm{ch}} \geq 2$ were observed between data and MC. Therefore, data and MC distributions were normalized to have the same particle density at $\bar{\eta} \approx 0$ and their ratio was fitted with a linear function,
3. the correction from step #1, multiplied by the value of the above function at $\bar{\eta} = \eta_m$, was used to scale the measured particle density at $\bar{\eta} \approx 0$.

Figure 9.10 presents the charged-particle densities near $\eta \approx 0$ as a function of $\sqrt{s}$ in inelastic pp and $p\bar{p}$ collisions. The SD results, calculated near $\bar{\eta} = \eta_m$ at $\sqrt{s}$ (M_X), are also shown.

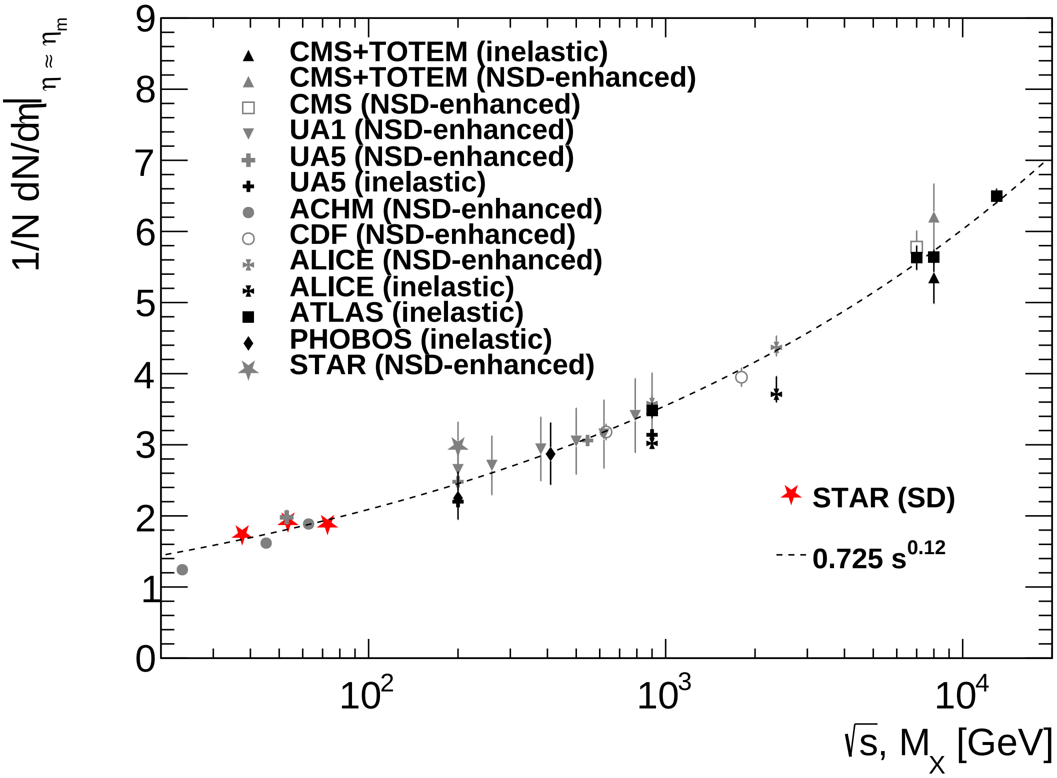

Figure 9.10: The evolution of $1/N_{\mathrm{ev}}\ dN/d\eta$ at $\eta \approx 0$ as a function of $\sqrt{s}$ in inelastic pp and $p\bar{p}$ collisions [12, 17, 18, 19, 20, 21, 22, 23, 24, 25, 26, 27]. The SD results were calculated near $\bar{\eta} \approx \eta_m$ at $\sqrt{s}$ (M_X). The dashed lines represent power-law fits to the NSD-enhanced [17] data. The results from this analysis are shown in red.

10. Summary and Conclusions

Inclusive and identified (pion, kaon, proton and their antiparticles) charged particle production in Single Diffractive Dissociation process has been measured in proton-proton collisions at $\sqrt{s} = 200$ GeV with the STAR detector at RHIC using data corresponding to an integrated luminosity of 15 nb^{-1}.

Significant differences are observed between the measured distributions of ξ and MC model predictions. Amongst the models considered, EPOS and PYTHIA 8 (MBR) without artificial suppression of diffractive cross sections at large ξ provide the best description of the data.

Charged-particle multiplicity and its dependence on the pseudorapidity and the transverse momentum are well described by PYTHIA8 and EPOS SD′ models. EPOS SD+SD′ and HERWIG do not describe the data.

π^-/π^+ and K^-/K^+ production ratios are close to unity and consistent with most of model predictions except for HERWIG.

$\bar{p}/p$ production ratio shows a significant deviation from unity in the $0.02 < \xi < 0.05$ range indicating a non-negligible transfer of the baryon number from the forward to the central region. Equal amount of protons and antiprotons are observed in the $\xi > 0.05$ range. PYTHIA8, EPOS SD+SD′ and EPOS SD′ agree with data for $\xi > 0.05$. For $0.02 < \xi < 0.05$ PYTHIA 8 and EPOS SD′ predict small deviations from unity (0.93) which is however higher than observed in data (0.85 ± 0.04). EPOS SD+SD′ predicts an asymmetry between $\bar{p}$ and p of $\sim 30\%$ at $0.02 < \xi < 0.05$. HERWIG predicts much larger baryon number transfers compared to data for $\xi < 0.1$ and shows consistency with data for $\xi > 0.1$.

Bibliography

[1] L. Adamczyk, L. Fulek, and R. Sikora, *Supplementary note on diffractive analyses of 2015 proton-proton data*, `https://drupal.star.bnl.gov/STAR/starnotes/private/psn0732`, July, 2019.

[2] B. Z. Kopeliovich and B. G. Zakharov, *Novel Mechanisms of Baryon Number Flow Over Large Rapidity Gap*, Z. Phys. **C43** (1989) 241.

[3] F. W. Bopp, *Baryon transport in dual models and the possibility of a backward peak in diffraction*, in *New trends in high-energy physics: Experiment, phenomenology, theory. Proceedings, International School-Conference, Crimea 2000, Yalta, Ukraine, May 27-June 4, 2000.* `arXiv:hep-ph/0007229 [hep-ph]`.

[4] M. Anderson et al., *The STAR Time Projection Chamber: A Unique tool for studying high multiplicity events at RHIC*, Nucl. Instrum. Meth. **A499** (2003) 659–678, `arXiv:nucl-ex/0301015 [nucl-ex]`.

[5] T. Sjöstrand, S. Mrenna, and P. Z. Skands, *PYTHIA 6.4 Physics and Manual*, JHEP **05** (2006) 026.

[6] R. Ciesielski and K. Goulianos, *MBR Monte Carlo Simulation in PYTHIA8*, PoS **ICHEP2012** (2013) 301, `arXiv:1205.1446 [hep-ph]`.

[7] *Roman Pot Phase II* - online DAQ monitoring*, `https://online.star.bnl.gov/rp/pp200/`.

[8] *STAR RunLog Browser*, `https://online.star.bnl.gov/RunLogRun15/`.

[9] W. Fischer, *Run Overview of the Relativistic Heavy Ion Collider*, `http://www.agsrhichome.bnl.gov/RHIC/Runs/`.

[10] *STAR Luminosity Tracker*, `https://www.star.bnl.gov/protected/common/common2015/trigger2015/runningStatepp200GeV/plots.html`.

[11] STAR Collaboration, J. Adam et al., *Results on Total and Elastic Cross Sections in Proton-Proton Collisions at $\sqrt{s} = 200$ GeV*, `arXiv:2003.12136 [hep-ex]`.

[12] STAR Collaboration, B. I. Abelev et al., *Systematic Measurements of Identified Particle Spectra in pp, d^{+} Au and Au+Au Collisions from STAR*, Phys. Rev. **C79** (2009) 034909, `arXiv:0808.2041 [nucl-ex]`.

[13] CDF Collaboration, D. Acosta et al., *Inclusive double pomeron exchange at the Fermilab Tevatron $\bar{p}p$ collider*, Phys. Rev. Lett. **93** (2004) 141601, `arXiv:hep-ex/0311023 [hep-ex]`.

[14] ATLAS Collaboration, G. Aad et al., *Charged-particle distributions in $\sqrt{s}$ = 13 TeV pp interactions measured with the ATLAS detector at the LHC*, Phys. Lett. **B758** (2016) 67–88, `arXiv:1602.01633 [hep-ex]`.

[15] G. D'Agostini, *A Multidimensional unfolding method based on Bayes' theorem*, Nucl. Instrum. Meth. **A362** (1995) 487–498.

[16] H. Bichsel, *A method to improve tracking and particle identification in TPCs and silicon detectors*, Nucl. Instrum. Meth. **A562** (2006) 154–197.

[17] CMS, TOTEM Collaboration, S. Chatrchyan et al., *Measurement of pseudorapidity distributions of charged particles in proton-proton collisions at $\sqrt{s} = 8$ TeV by the CMS and TOTEM experiments*, Eur. Phys. J. **C74** (2014) 3053.

[18] UA1 Collaboration, C. Albajar et al., *A Study of the General Characteristics of $p\bar{p}$ Collisions at $\sqrt{s} = 0.2$-TeV to 0.9-TeV*, Nucl. Phys. **B335** (1990) 261–287.

[19] UA5 Collaboration, G. J. Alner et al., *Scaling of Pseudorapidity Distributions at c.m. Energies Up to 0.9-TeV*, Z. Phys. **C33** (1986) 1–6.

[20] ACHM Collaboration, W. Thome et al., *Charged Particle Multiplicity Distributions in p p Collisions at ISR Energies*, Nucl. Phys. **B129** (1977) 365.

[21] CDF Collaboration, F. Abe et al., *Pseudorapidity distributions of charged particles produced in $\bar{p}p$ interactions at $\sqrt{s} = 630$ GeV and 1800 GeV*, Phys. Rev. **D41** (1990) 2330.

[22] ALICE Collaboration, K. Aamodt et al., *Charged-particle multiplicity measurement in proton-proton collisions at $\sqrt{s} = 0.9$ and 2.36 TeV with ALICE at LHC*, Eur. Phys. J. **C68** (2010) 89–108.

[23] ATLAS Collaboration, M. Aaboud et al., *Charged-particle distributions at low transverse momentum in $\sqrt{s} = 13$ TeV pp interactions measured with the ATLAS detector at the LHC*, Eur. Phys. J. **C76** (2016) 502, `arXiv:1606.01133 [hep-ex]`.

[24] ATLAS Collaboration, G. Aad et al., *Charged-particle distributions in pp interactions at $\sqrt{s} = 8$ TeV measured with the ATLAS detector*, Eur. Phys. J. **C76** (2016) 403.

[25] ATLAS Collaboration, G. Aad et al., *Charged-particle multiplicities in pp interactions measured with the ATLAS detector at the LHC*, New J. Phys. **13** (2011) 053033.

[26] PHOBOS Collaboration, B. Alver et al., *Phobos results on charged particle multiplicity and pseudorapidity distributions in Au+Au, Cu+Cu, d+Au, and p+p collisions at ultra-relativistic energies*, Phys. Rev. **C83** (2011) 024913.

[27] CMS Collaboration, V. Khachatryan et al., *Transverse-momentum and pseudorapidity distributions of charged hadrons in pp collisions at $\sqrt{s} = 7$ TeV*, Phys. Rev. Lett. **105** (2010) 022002, `arXiv:1005.3299 [hep-ex]`.

Appendices

A. Proton and Antiproton DCA Distributions

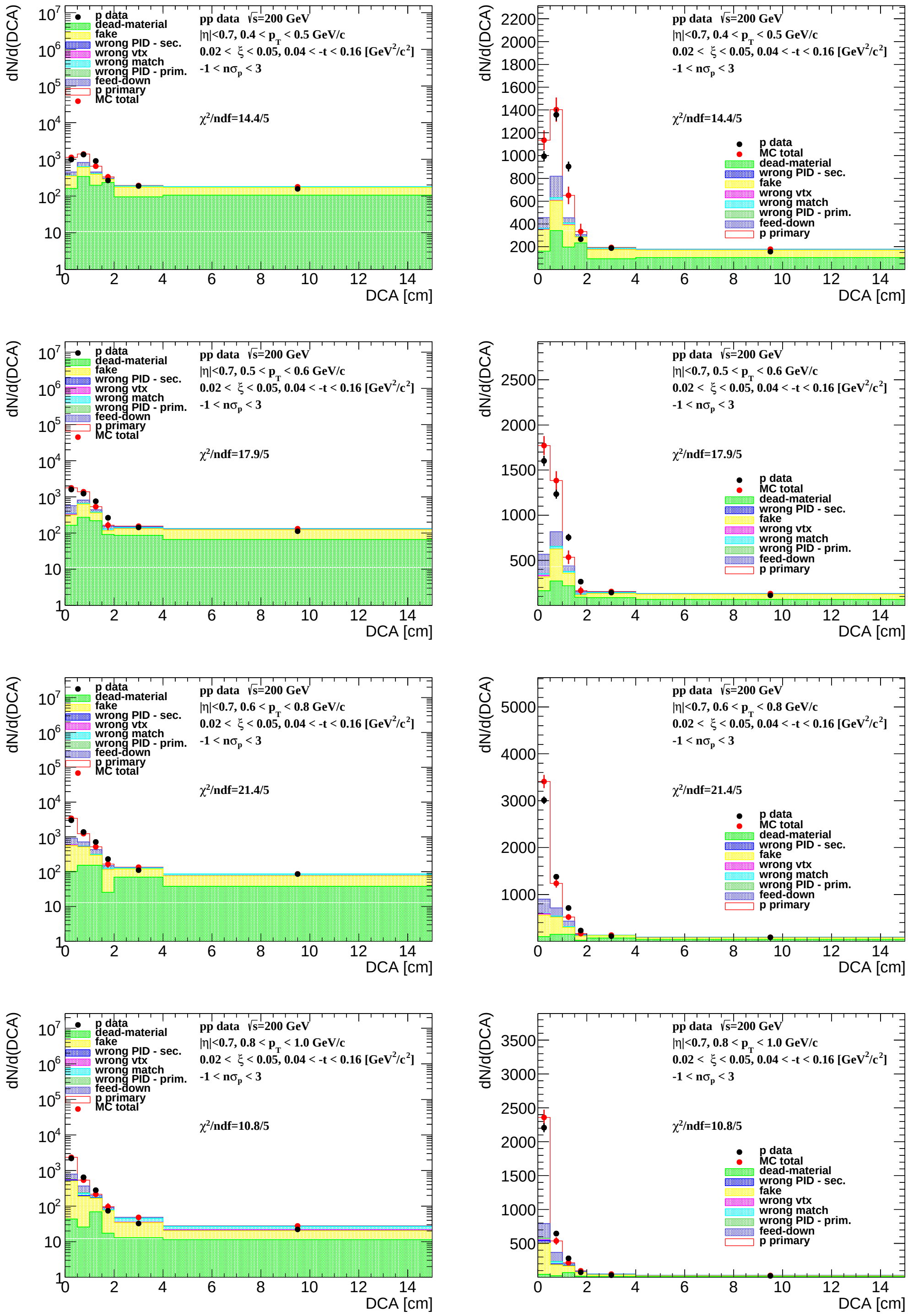

Figure A.1: Distributions of DCA for protons in SD interactions with $0.02 < \xi < 0.05$ and loose selection.

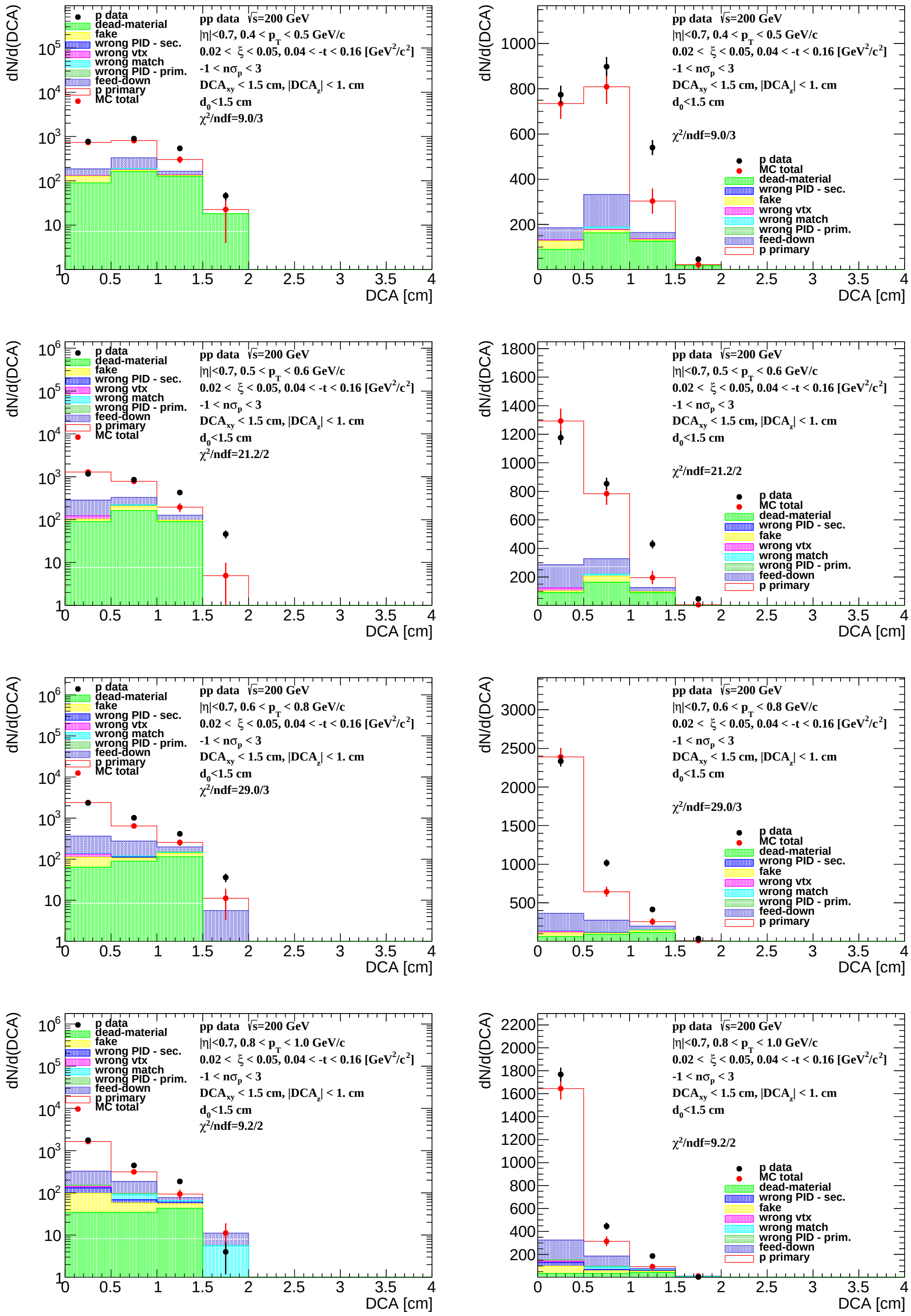

Figure A.2: Distributions of DCA for protons in SD interactions with $0.02 < \xi < 0.05$ and normal selection.

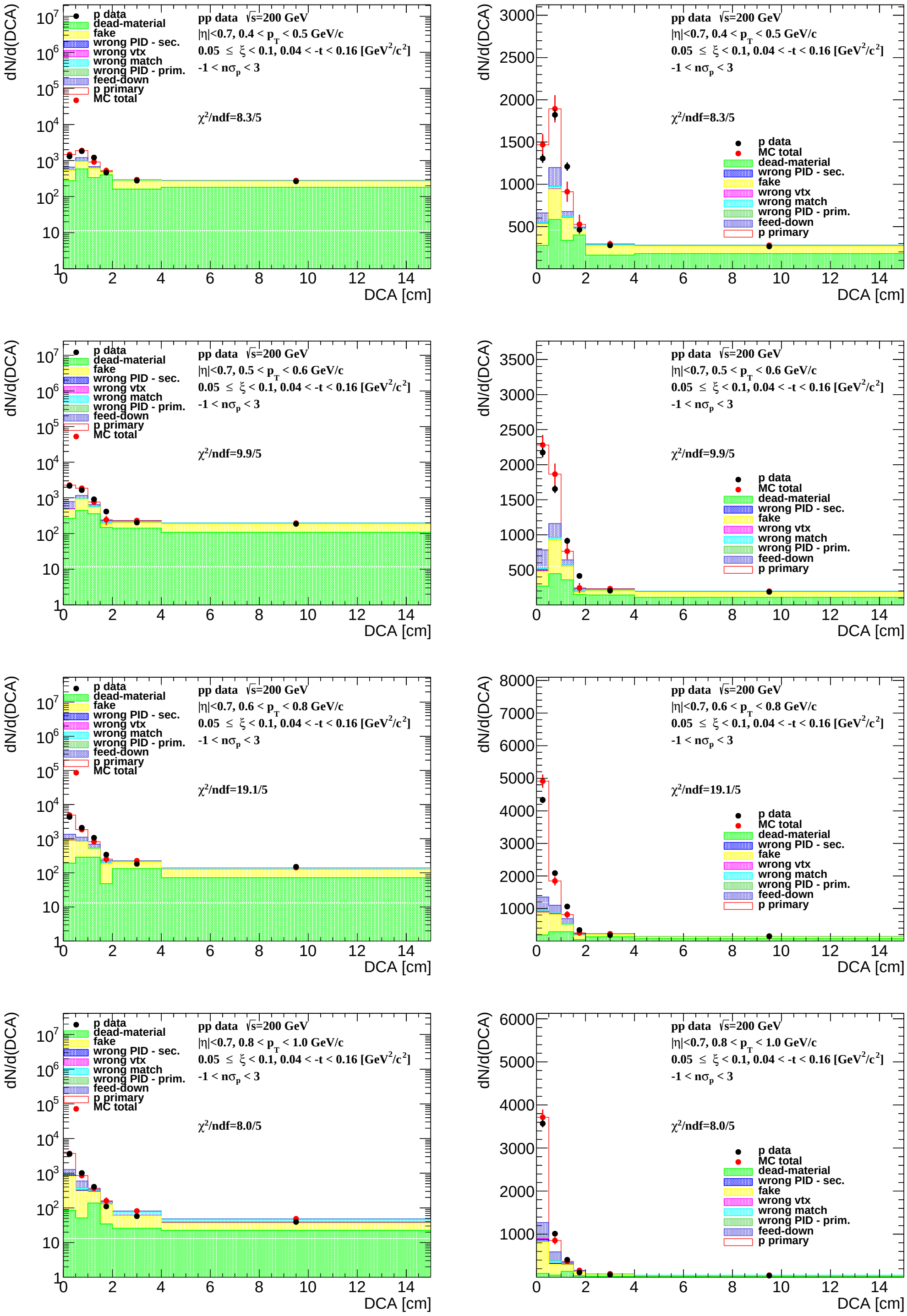

Figure A.3: Distributions of DCA for protons in SD interactions with $0.05 < \xi < 0.1$ and loose selection.

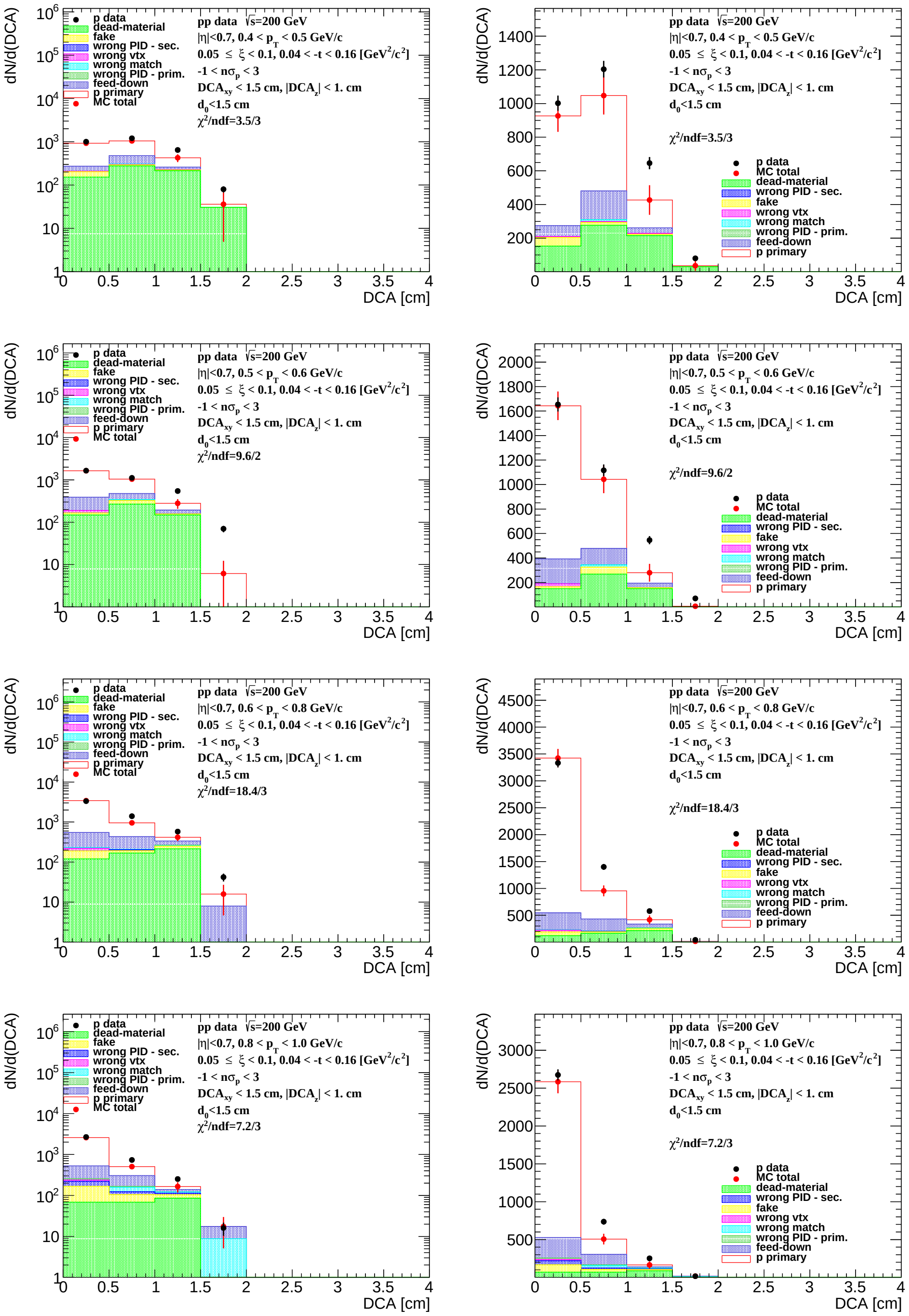

Figure A.4: Distributions of DCA for protons in SD interactions with $0.05 < \xi < 0.1$ and normal selection.

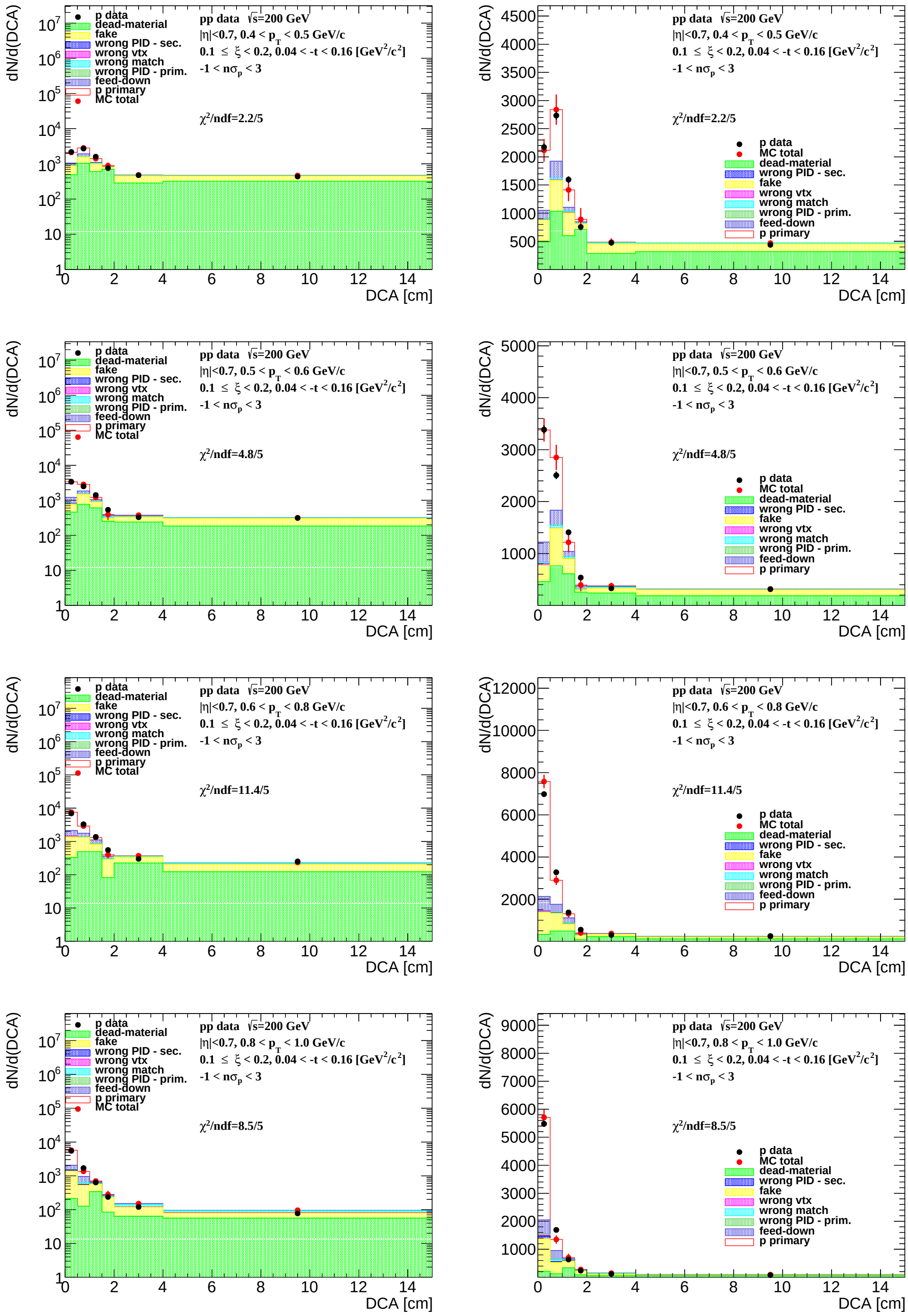

Figure A.5: Distributions of DCA for protons in SD interactions with $0.1 < \xi < 0.2$ and loose selection.

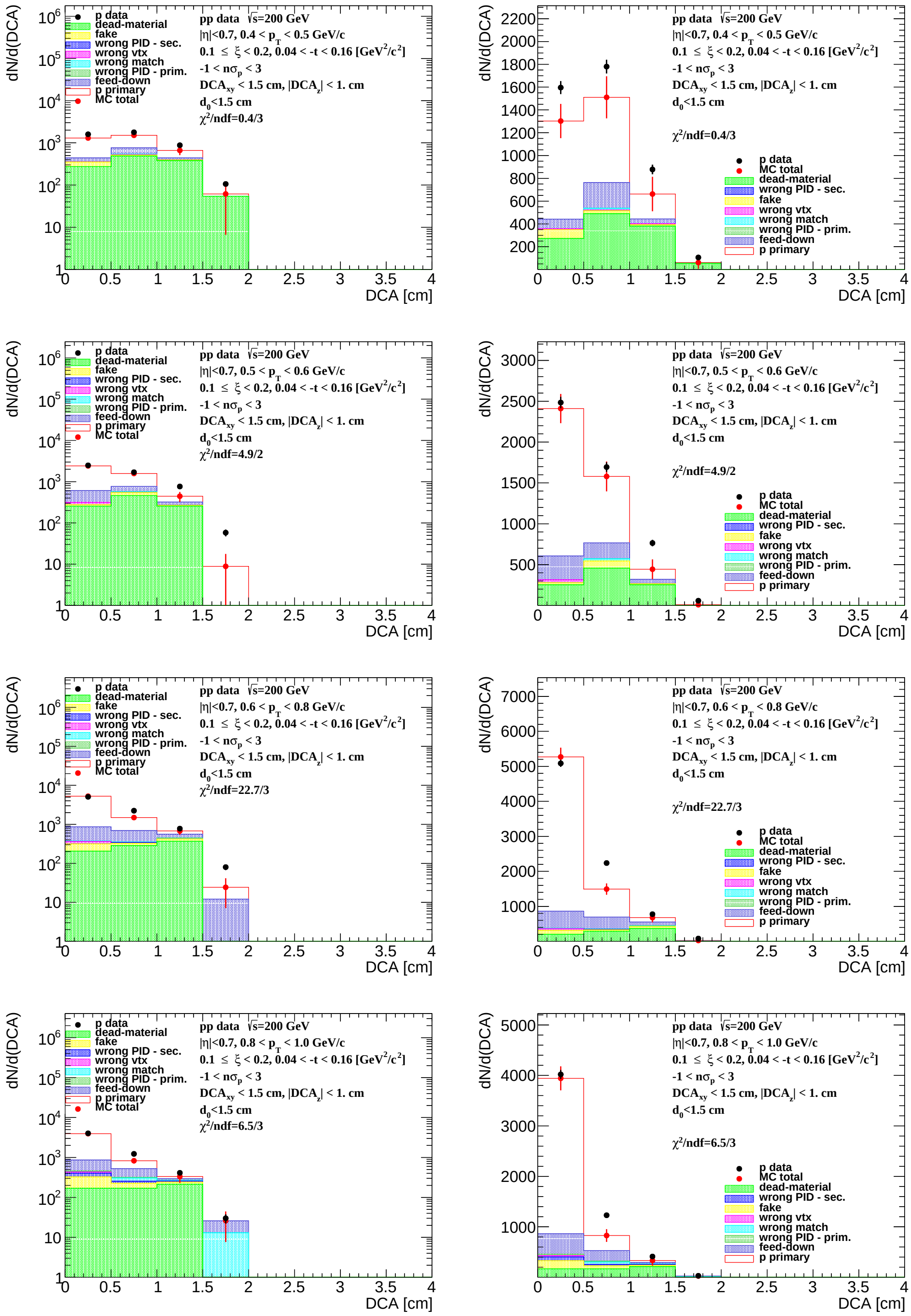

Figure A.6: Distributions of DCA for protons in SD interactions with $0.1 < \xi < 0.2$ and normal selection.

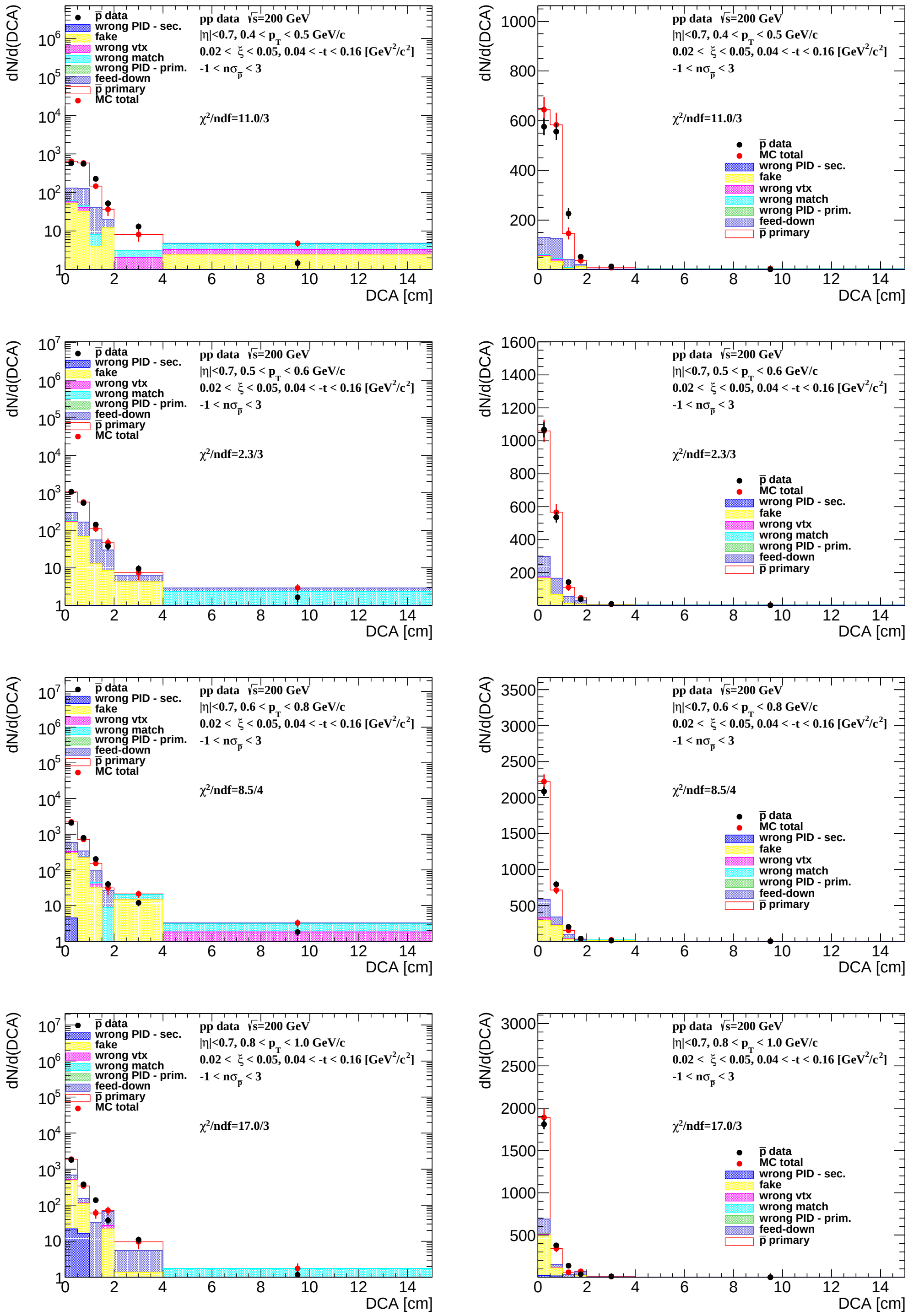

Figure A.7: Distributions of DCA for antiprotons in SD interactions with $0.02 < \xi < 0.05$ and loose selection.

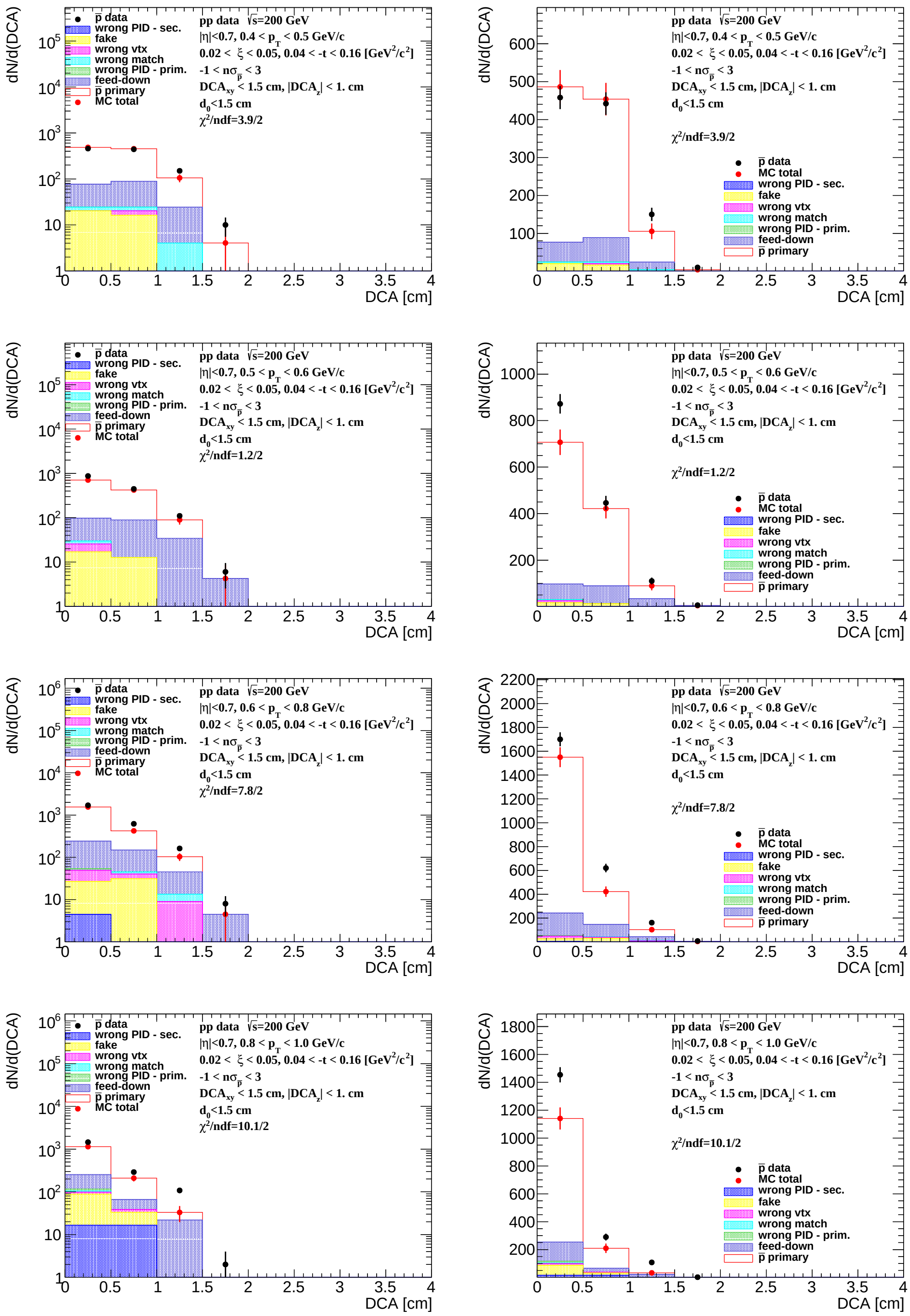

Figure A.8: Distributions of DCA for antiprotons in SD interactions with $0.02 < \xi < 0.05$ and normal selection.

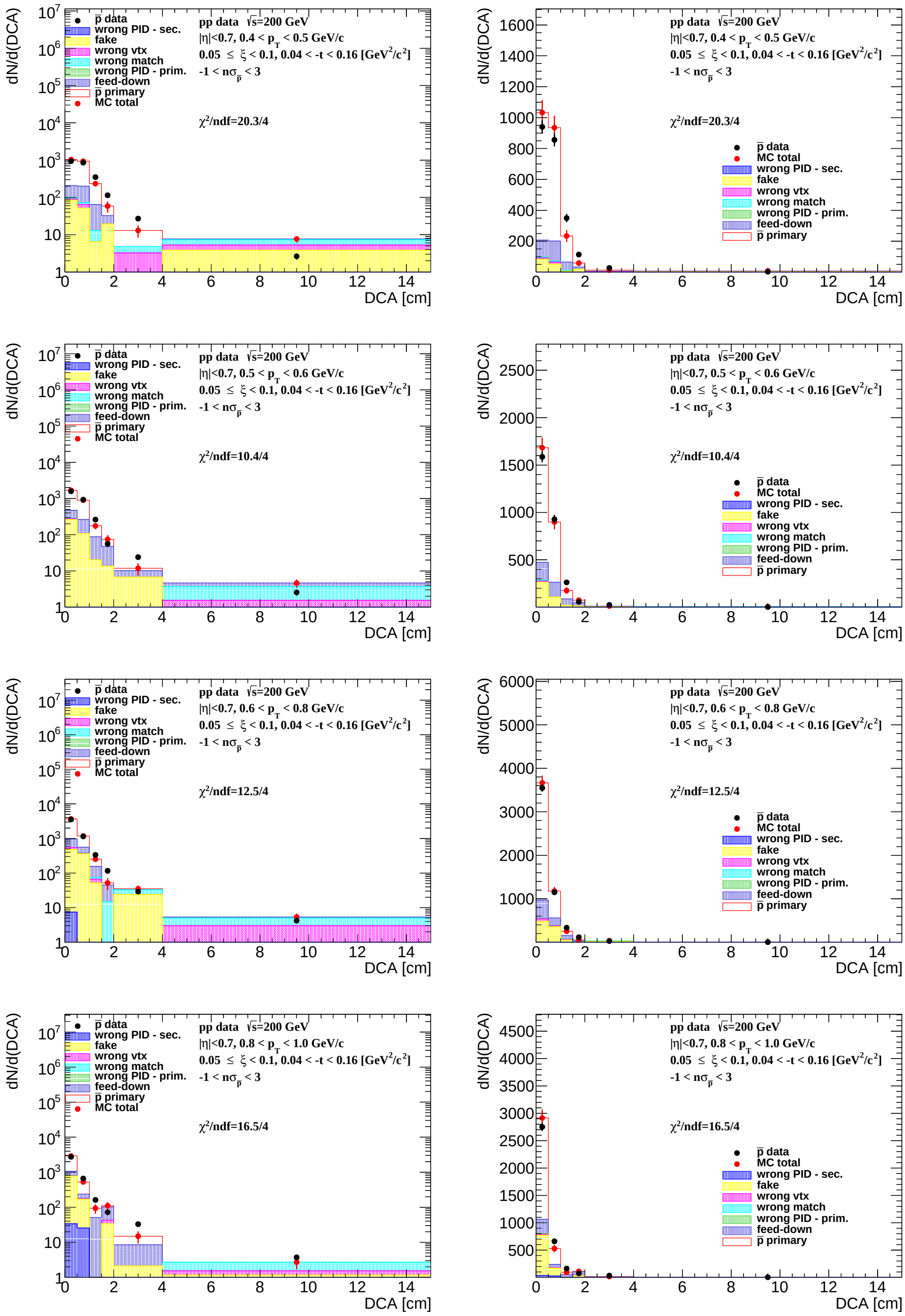

Figure A.9: Distributions of DCA for antiprotons in SD interactions with $0.05 < \xi < 0.1$ and loose selection.

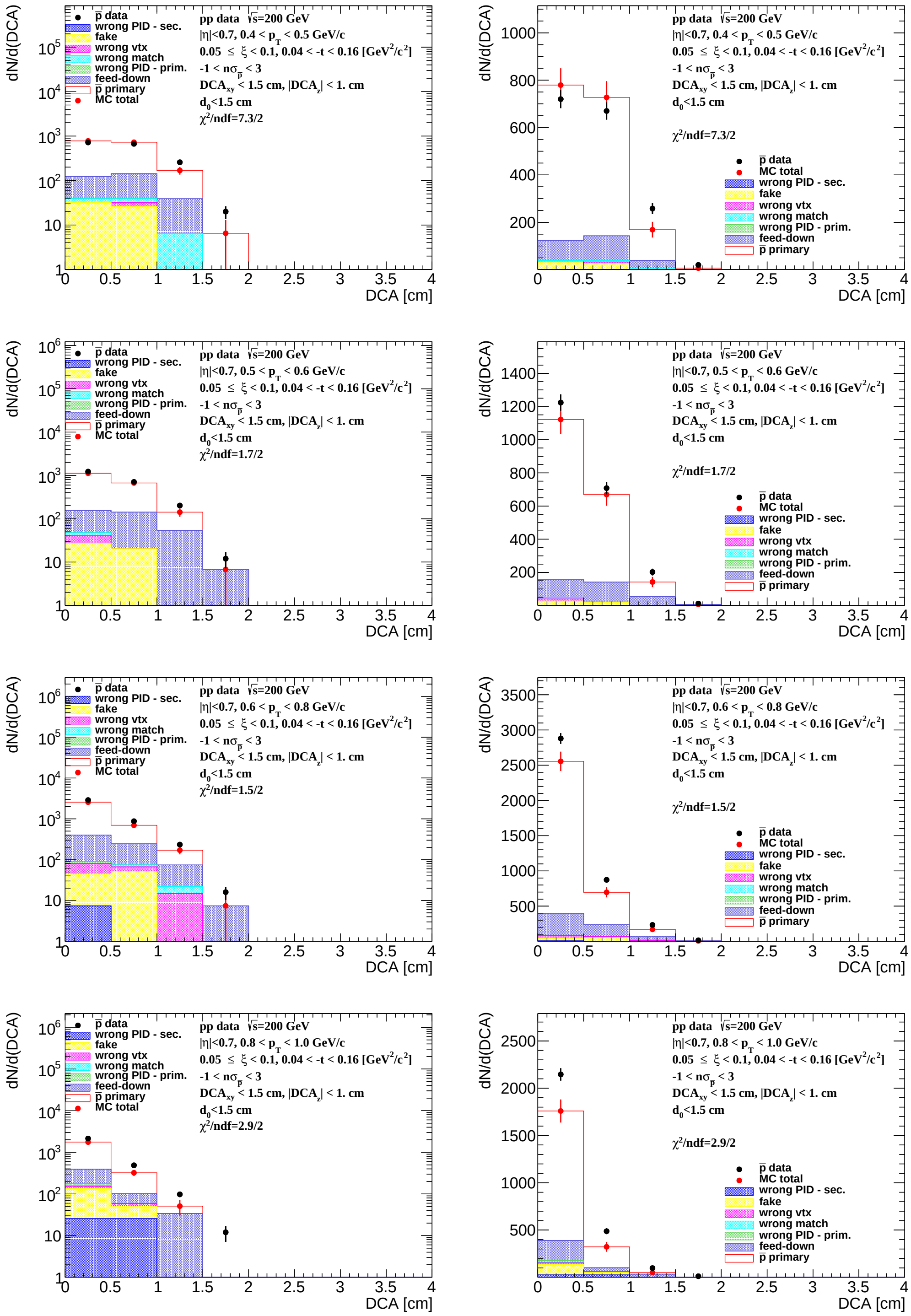

Figure A.10: Distributions of DCA for antiprotons in SD interactions with $0.05 < \xi < 0.1$ and normal selection.

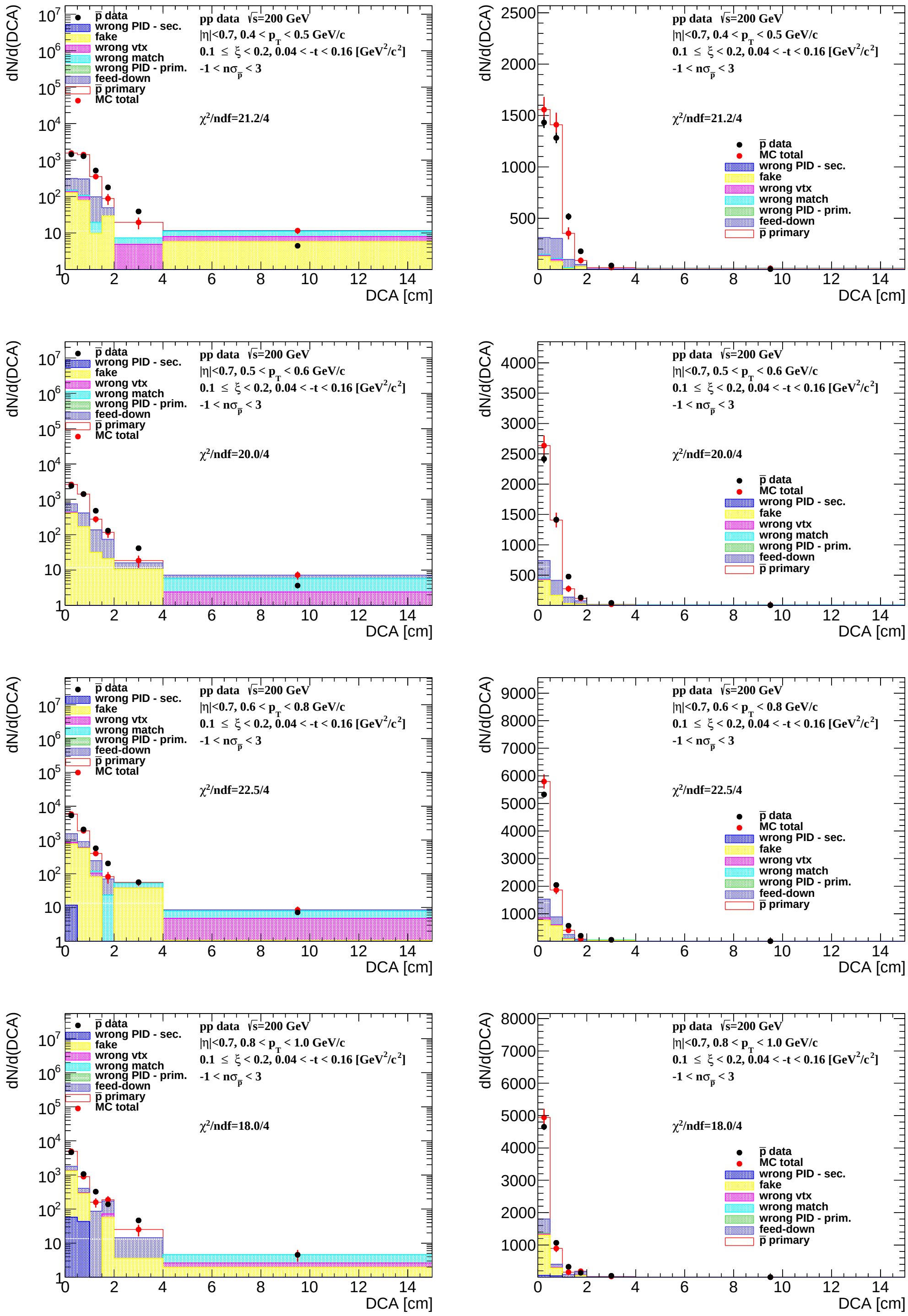

Figure A.11: Distributions of DCA for antiprotons in SD interactions with $0.1 < \xi < 0.2$ and loose selection.

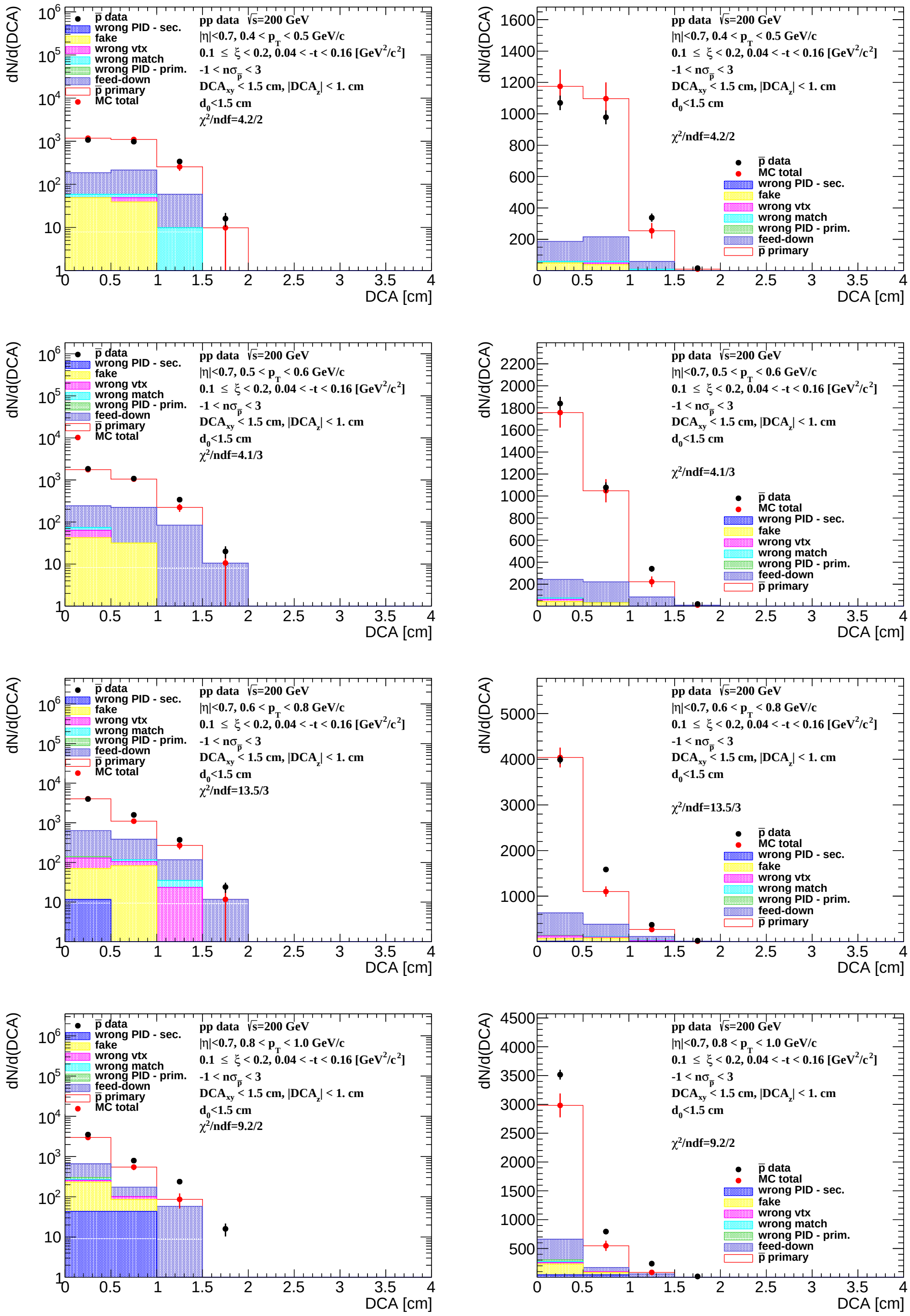

Figure A.12: Distributions of DCA for antiprotons in SD interactions with $0.1 < \xi < 0.2$ and normal selection.

B. Distributions of $n\sigma^{i}_{dE/dx}$ in SD

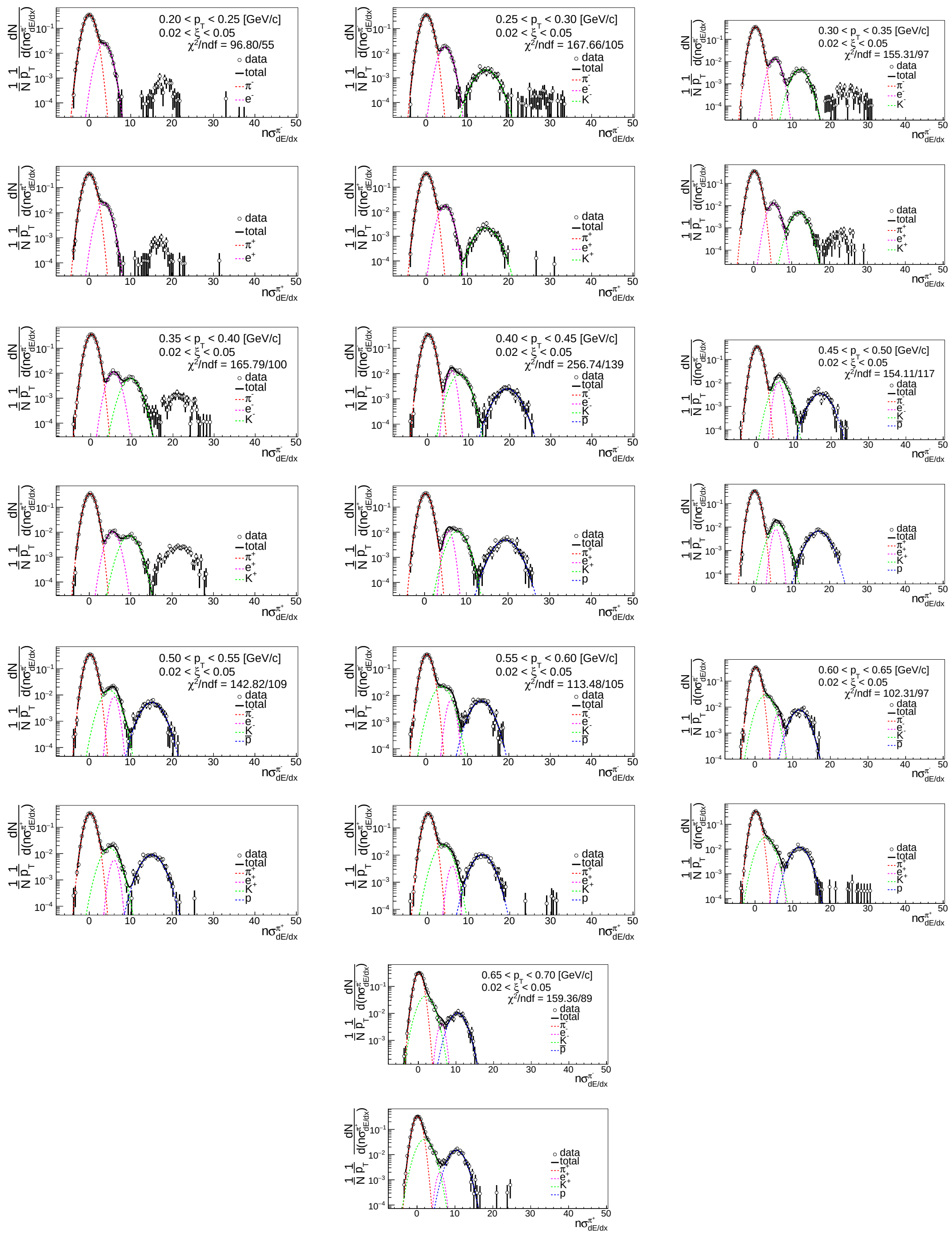

Figure B.1: Distributions of $n\sigma^{\pi^{\pm}}_{dE/dx}$ for $\pi^{\pm}$ in SD interactions with $0.02 < \xi < 0.05$.

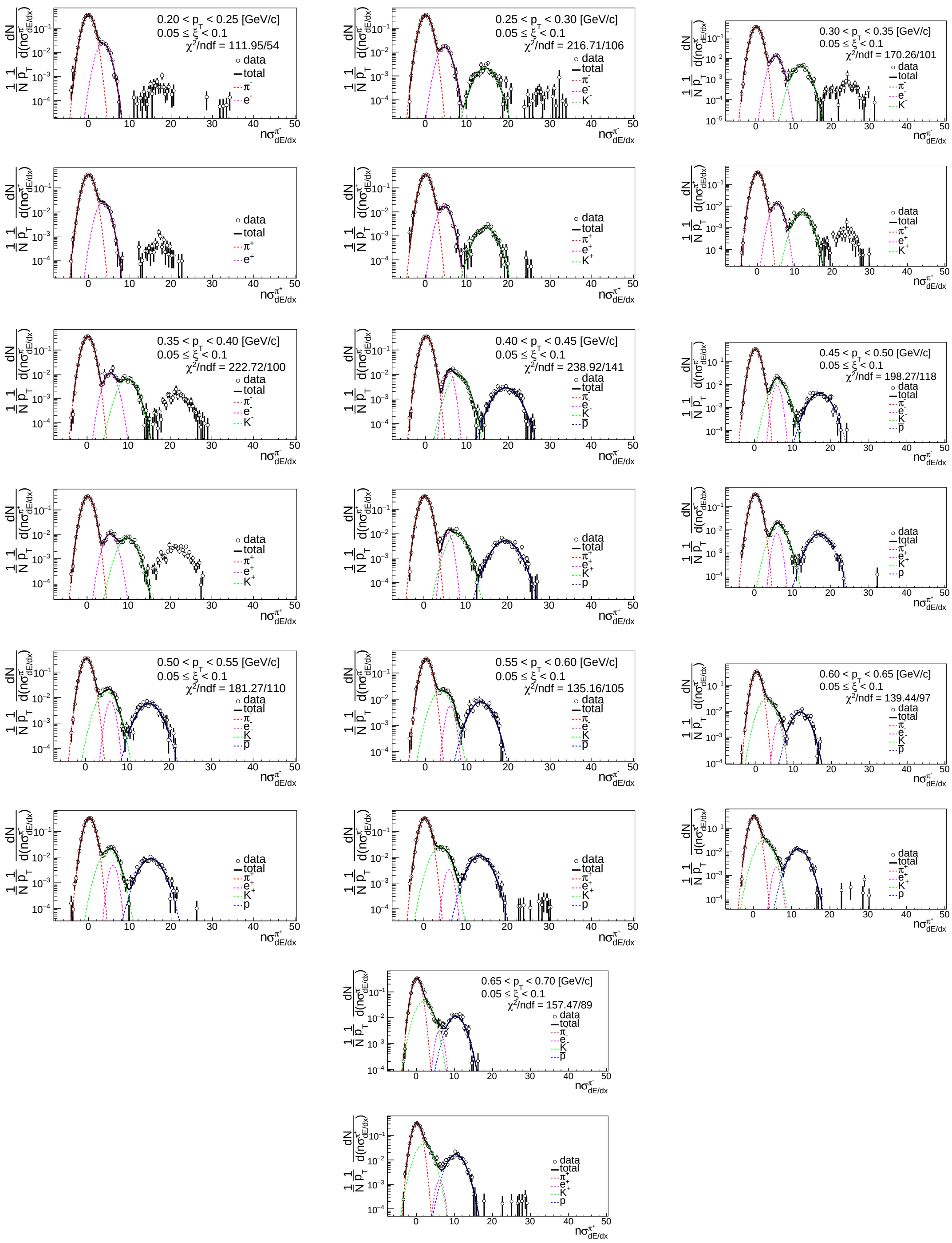

Figure B.2: Distributions of $n\sigma^{\pi^{\pm}}_{dE/dx}$ for $\pi^{\pm}$ in SD interactions with $0.05 < \xi < 0.1$.

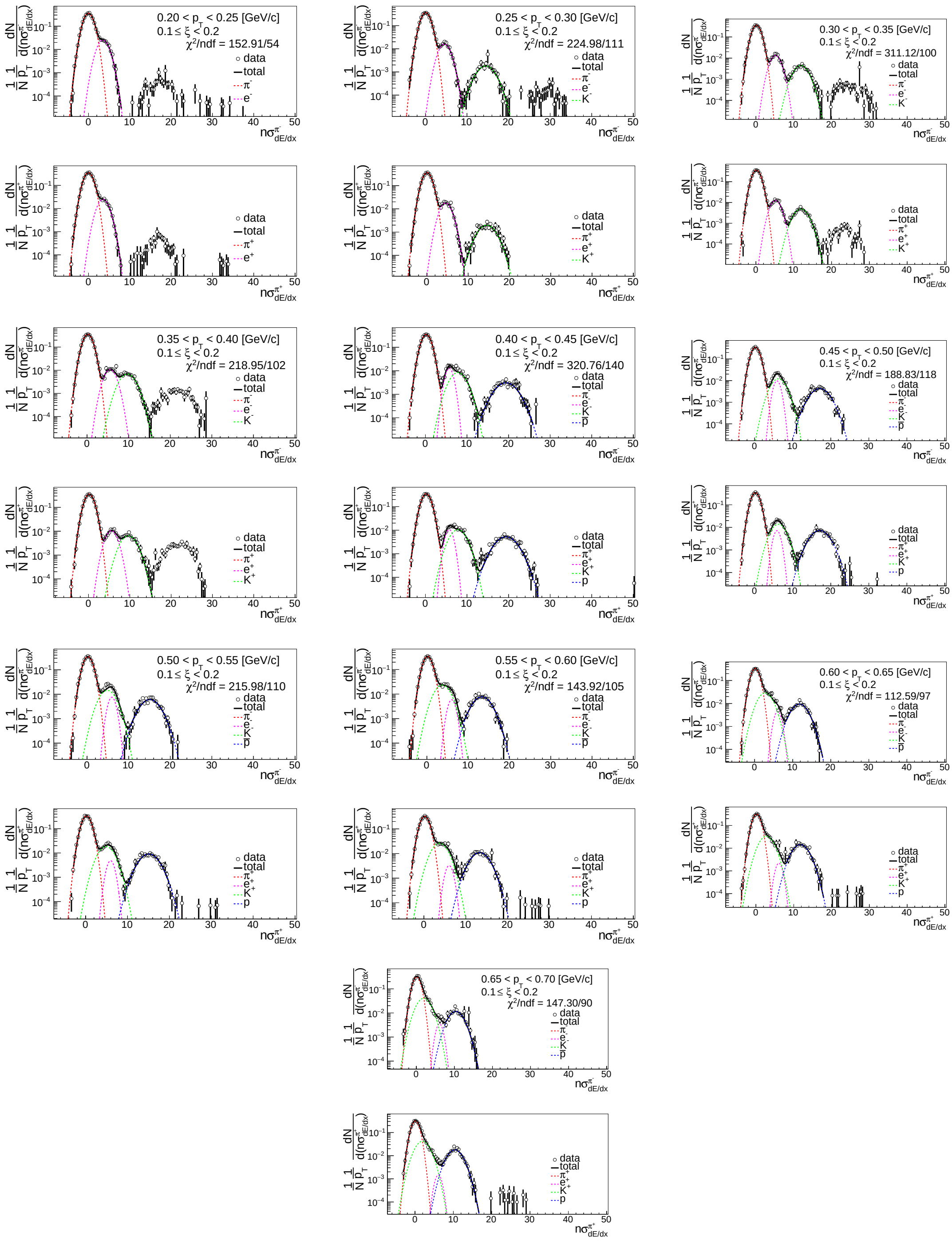

Figure B.3: Distributions of $n\sigma^{\pi^{\pm}}_{dE/dx}$ for $\pi^{\pm}$ in SD interactions with $0.1 < \xi < 0.2$.

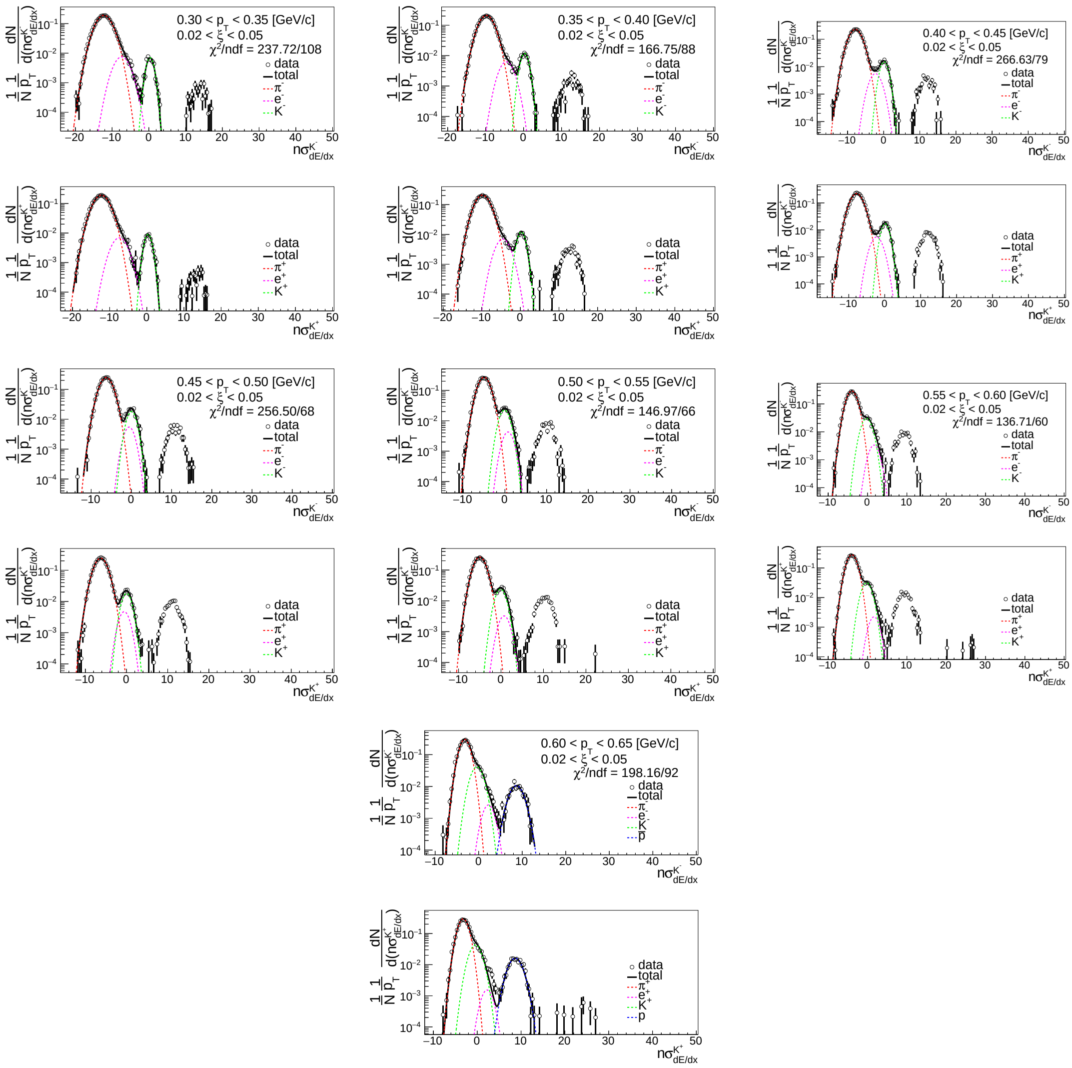

Figure B.4: Distributions of $n\sigma^{K^{\pm}}_{dE/dx}$ for $K^{\pm}$ in SD interactions with $0.02 < \xi < 0.05$.

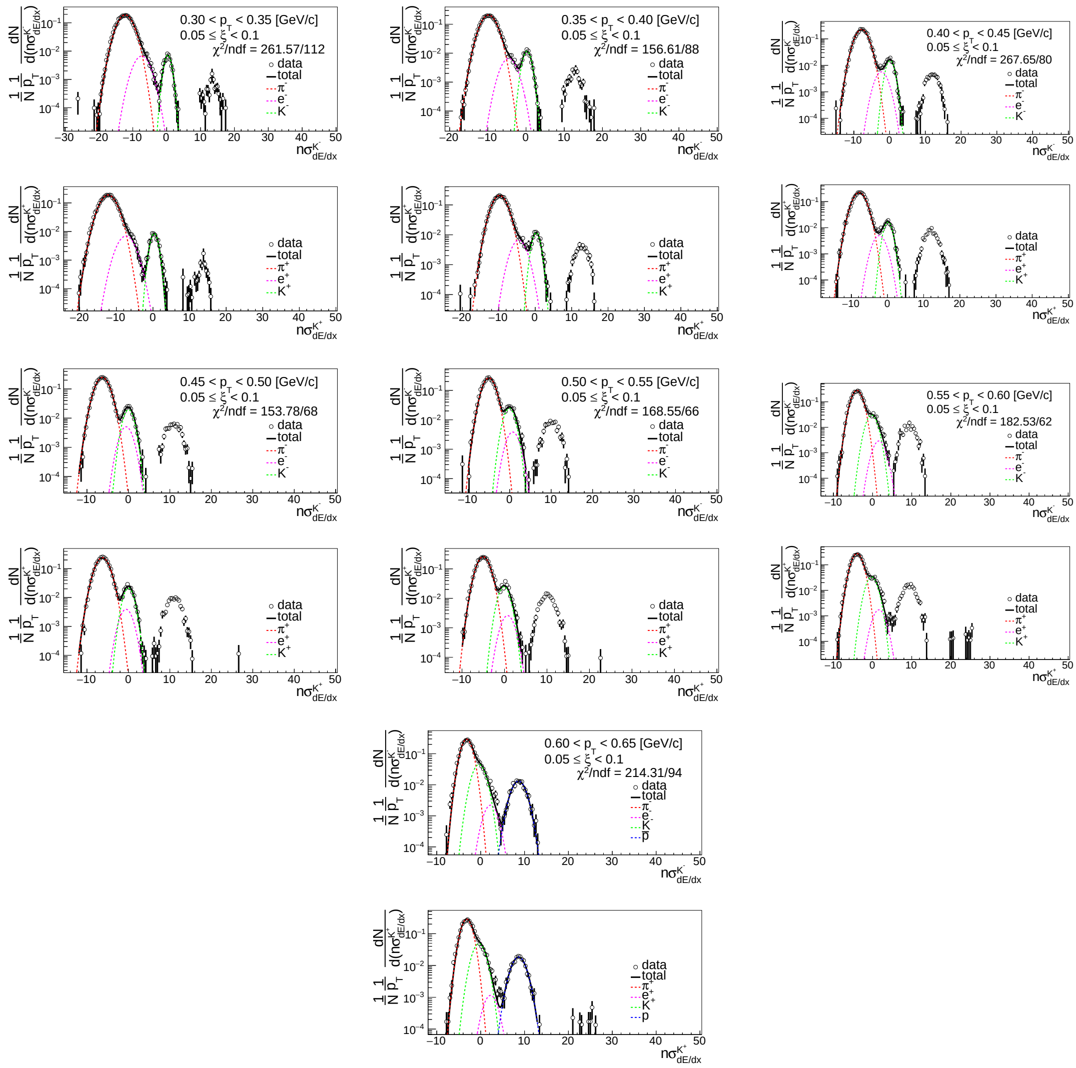

Figure B.5: Distributions of $n\sigma^{K^\pm}_{dE/dx}$ for $K^\pm$ in SD interactions with $0.05 < \xi < 0.1$.

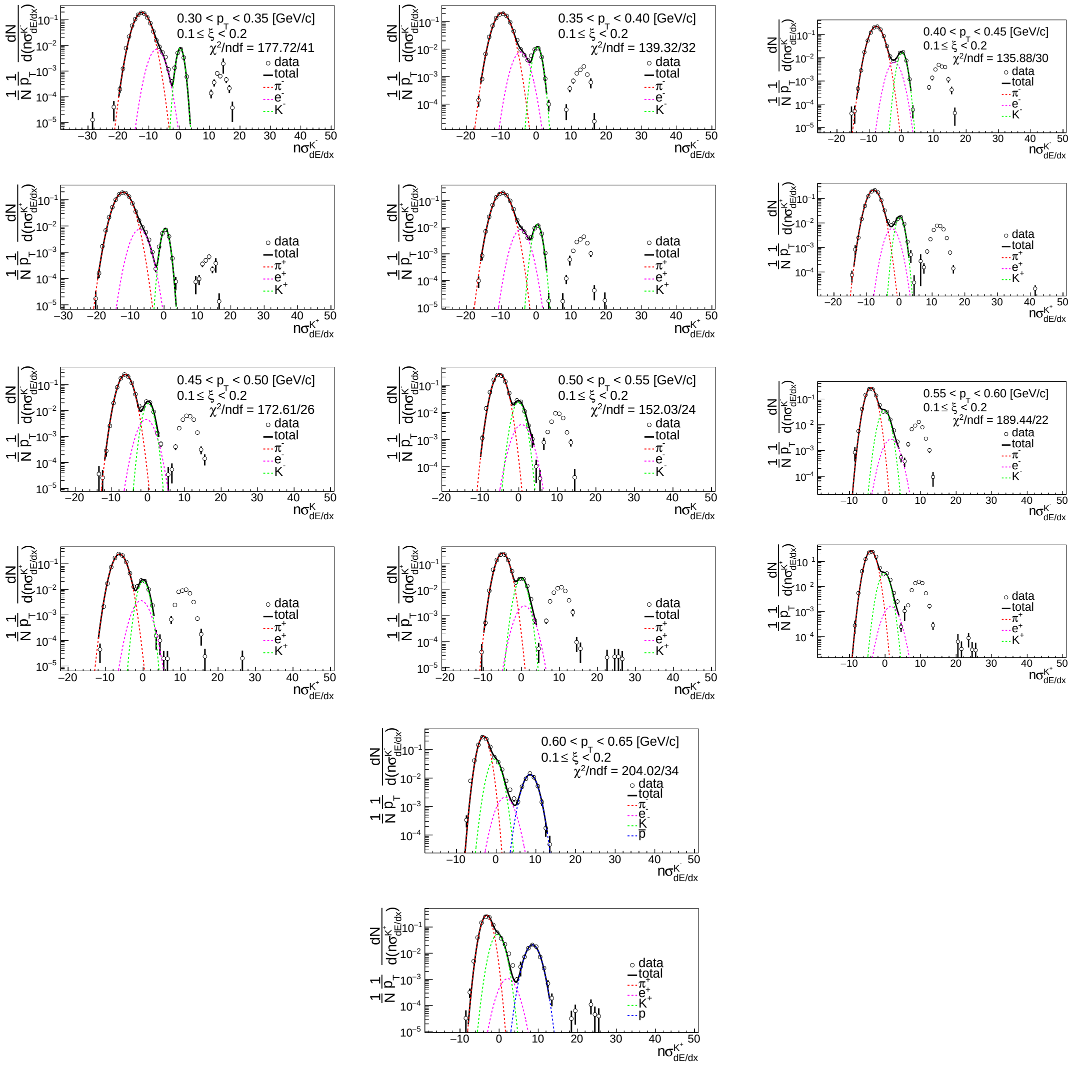

Figure B.6: Distributions of $n\sigma^{K^{\pm}}_{dE/dx}$ for $K^{\pm}$ in SD interactions with $0.1 < \xi < 0.2$.

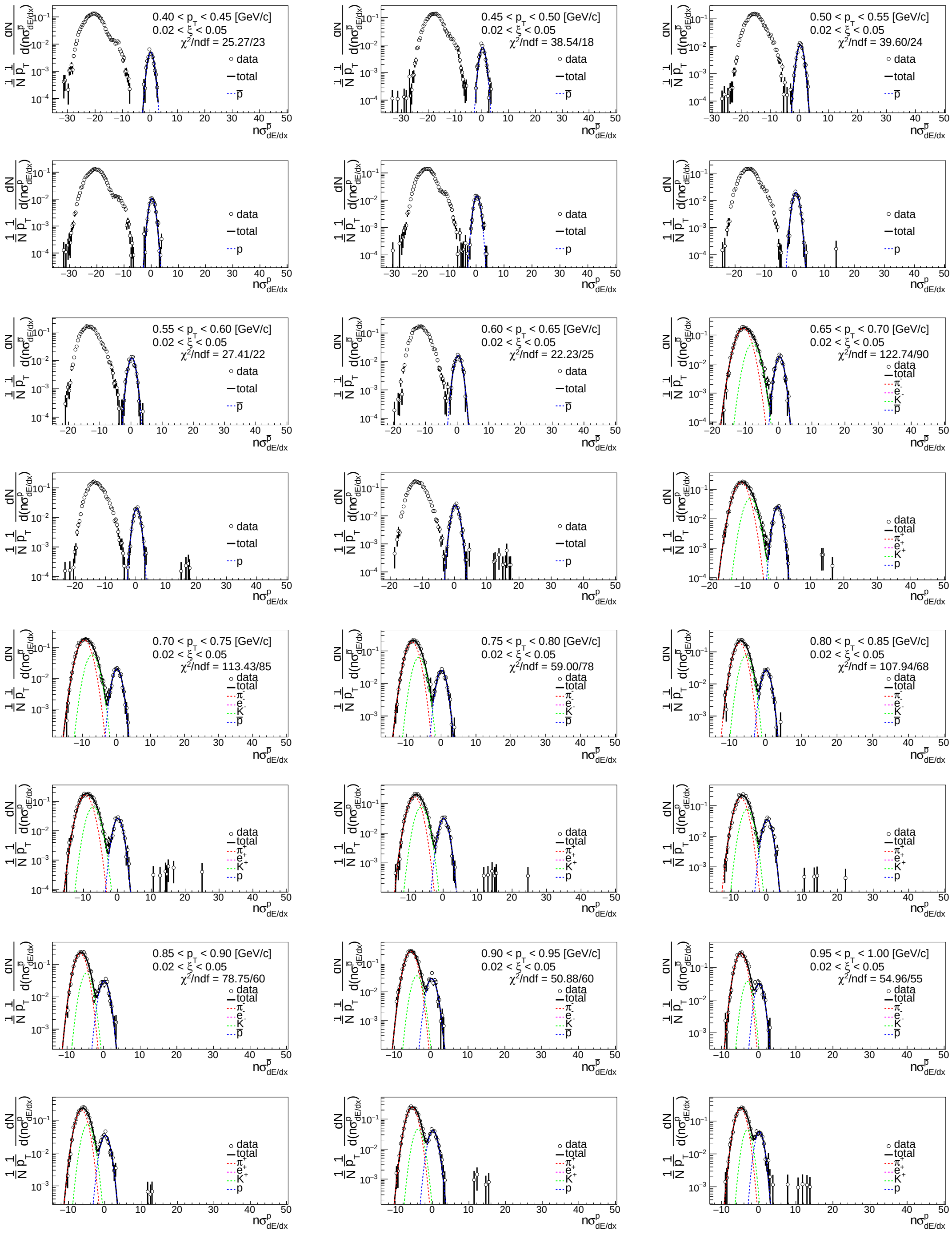

Figure B.7: Distributions of $n\sigma^{\bar{p},p}_{dE/dx}$ for $\bar{p}, p$ in SD interactions with $0.02 < \xi < 0.05$.

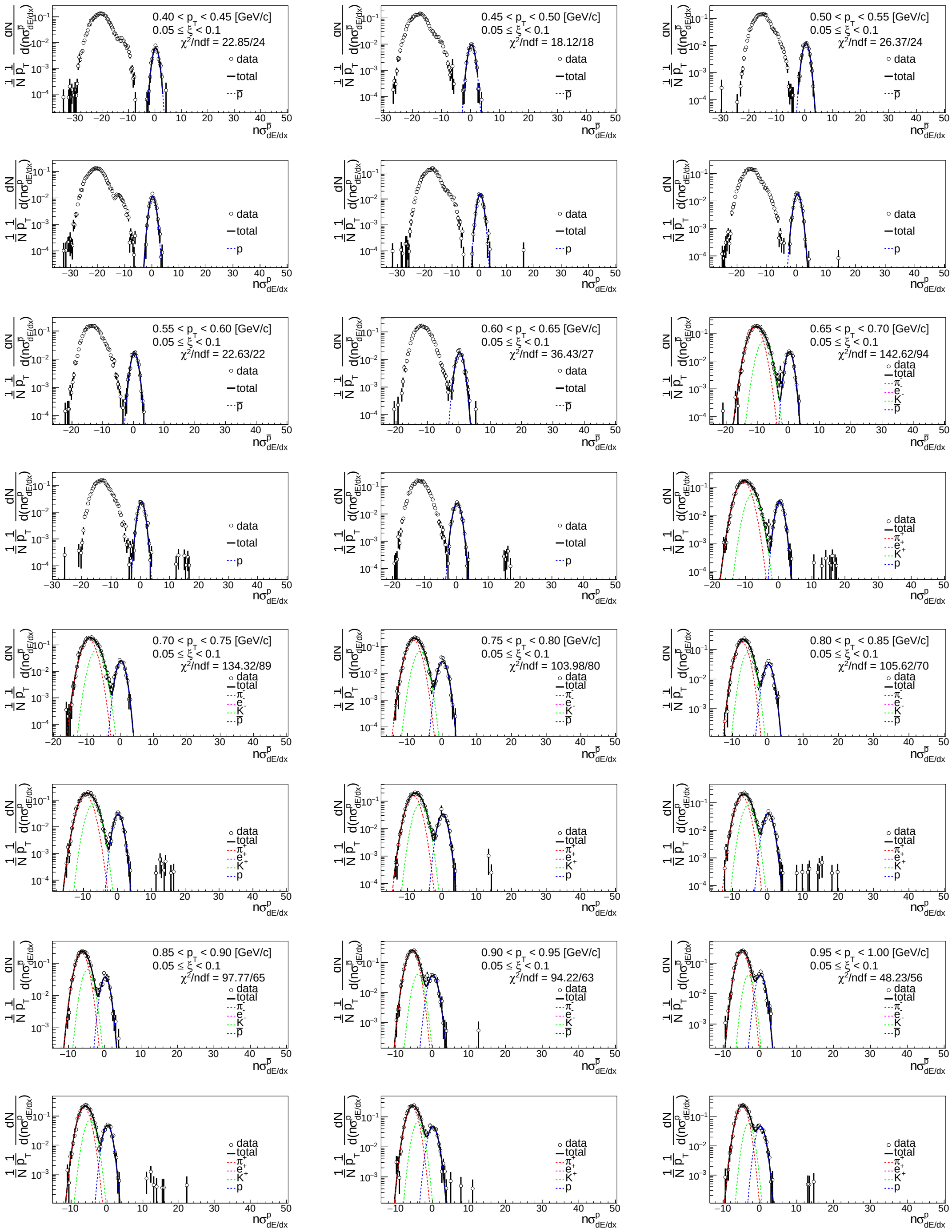

Figure B.8: Distributions of $n\sigma_{dE/dx}^{\bar{p},p}$ for $\bar{p}, p$ in SD interactions with $0.05 < \xi < 0.1$.

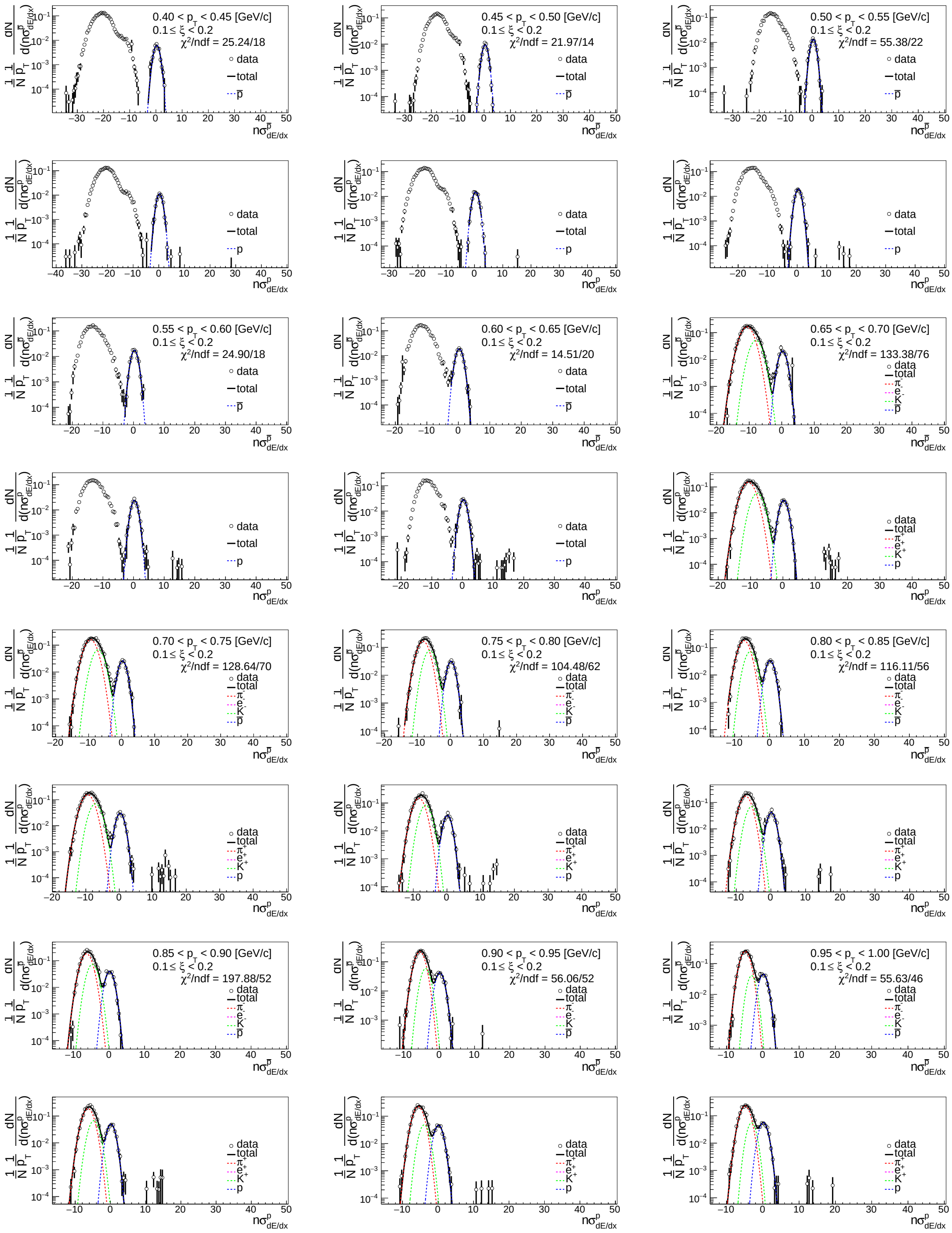

Figure B.9: Distributions of $n\sigma^{\bar{p},p}_{dE/dx}$ for $\bar{p}, p$ in SD interactions with $0.1 < \xi < 0.2$.